Faculty of Sciences

Department of Earth and Environmental Sciences

chawada.nkanokang@studentmail.biust.ac.bw

THE GEOPHYSICAL SIGNATURES OF THE KGAGODI BASIN, CENTRAL BOTSWANA

by

CHAWADA NKANOKANG

Student ID number: 13000458

BSc (Geology) (BIUST)

A Thesis Submitted to the Faculty of Sciences in Partial Fulfilment of the Requirements for the Award of the Degree of Master of Science in Geological Sciences of BIUST

Supervisor: Dr. Ame Thato Selepeng

Department of Earth and Environmental Sciences

Faculty of Science, BIUST

E-mail Address: selepengat@biust.ac.bw

August, 2022

TABLE OF CONTENTS

BOTSWANA INTERNATIONAL UNIVERSITY OF SCIENCE & TECHNOLOGY

POSTGRADUATE SCHOOL

Declaration Regarding the Work and Copyright

DECLARATION REGARDING THE WORK AND COPYRIGHT

Candidate CHAWADA NKANOKANG

Student ID: 13000458

Thesis Titled: The geophysical signatures of the Kgagodi basin, central Botswana

I, the **Candidate**, certify that the Thesis is all my own original work and that I have not obtained a degree in this University or elsewhere on the basis of any of this work.

Signed: ---------- Date: 12th August 2022

Primary Supervisor Dr Ame Thato Selepeng

I, the Candidate's **Primary Supervisor**, hereby confirm that I have inspected the above titled thesis and, to the best of my knowledge, it is based on the original work of the candidate.

Signed: ---------- Date: 12th August 2022

Abstract

The Kgagodi basin is located at 22°28'26.67"S and 27°34'54.10"E, about 7 km South of the Kgagodi village, Central Botswana. This structure is buried by sediments thus it has no pronounced surficial expression. The Kgagodi basin has been suggested to represent an intersection of two fault lines thereby making it a prospective hydrological target. Investigating the Kgagodi basin allows understanding of the impact process and its effects on geological formations. The current study aimed at delineating the geologic structures within the basin and determining the 3-D geometry of the Kgagodi basin using high resolution aeromagnetic data, ground gravity data, and Vertical electrical sounding (VES) data. Results of the study will aid future scientific investigations and guide drilling initiatives in the basin.

Aeromagnetic data analysis showed a smooth textured magnetic signature over the basin corresponding to younger sediment fill as compared to the noisy signature of the surrounding metamorphic terrain. Two major cross cutting lineaments were identified. The first lineament has a NW-SE trend and is characterised by a magnetic high and was presumed to be a dyke. The second lineament observed is a low magnetic signature anomaly trending NE-SW which can be attributed to possible faulting. Results of the gravity survey showed two main signatures on the Bouguer Anomaly (BA) map: (1) a pronounced density low (-127.8 to – 119.4 mGal) over the basin which is associated with the basin fill and (2), high density anomalies (-119.5 to -112.2 mGal) associated with the metamorphic basement terrain. The 3-D density distribution model of the BA data showed a bowl-shaped structure with a diameter of ~3.5 km. The density model revealed predominant gravity low anomaly features (1 to 2.75 g/cm^3) at the centre, which is the suspected

impact crater region. From the surface until approximately 970m deep, the model showed medium density contrasts (2.0-2.75 g/cm^3) and were interpreted to be the later crater fill possibly made up of allochthonous material. A parabolic lens of low densities ranging between 1 to 1.9 g/cm^3 was observed at depth of 700-900m and was proposed to be the breccia lens made up of both allochthonous material and highly shocked and melted target material. Beneath this layer high densities of (2-3 g/cm^3), suggested to represent the parautochthonous material were also observed.

Results from 1-D modelling of the VES data showed that the predominant field curve in the area is the H-type combination curve with mostly three and four geoelectrical layers identified. The centre of the basin is characterised by a low resistivity zone (6-193 ohm.m), corresponding to conductive basin fill and saturated sediments. The constructed geoelectrical cross sections along East-West profiles indicated that the shallow basin fill (about 100m depth) is made up of alternating layers of different sediments. From this investigation, it was concluded that the magnetic signature over the Kgagodi basin is smooth textured. The two cross cutting lineaments in the Kgagodi basin could be an intersection of two fault lines. The dolerite dyke in the area could be older or relatively the same age as the Kgagodi basin. This structure has a diameter of approximately 3. 5 km and its depth to the basement is 900m. The shallow basin fill is made up of possibly faulted low resistive materials, with signatures corresponding to those of saturated sediments. The inside of the basin is considered to have good groundwater potential.

Key words; Kgagodi basin, impact crater, aeromagnetic method, gravity method, 3-D density model, vertical electrical sounding method.

Acknowledgements

Foremost, I would like to extend my sincere appreciation to my supervisor Dr. Ame Thato Selepeng. Completion of this study would have not been possible without his expertise, patience, motivation, and guidance.

I would also like to extend my thanks to the rest of the geophysics team in the Department of Earth and Environmental Sciences, BIUST who played a key role in data collection for this study; Mr. Boniface Kgosidintsi (geophysics technician), Mr. Calistus Ramotoroko (PhD student), Mr. Valiant Mosokomani (MSc student), Mr. Desmond Botsisang (MSc student), Ms. Sara Babi (MSc student) and Mr. Kopo Gareosenye (MSc student). I thank the two anonymous external reviewers of this thesis whose constructive comments significantly improved the thesis.

I am extremely grateful to my parents for their moral support, prayers, and sacrifices throughout my studies. Above all, I thank God for giving me the strength and protection to complete my studies.

List of tables

List of figures

Chapter 1

Introduction

1.1 Background information

The Earth's continual rotation around the sun causes it to pass close to orbiting asteroids and comets on occasion, resulting in near-earth-object situations (Abraham, 2004; Grieve, 2005). On impact with the earth at a very high speed, these objects leave behind marks or geologic structures called impact craters (Abraham, 2004). The process by which these unique geologic structures form is referred to as impact cratering (Senft & Stewart, 2007; Raiskila, 2013; Zylberman, 2017). During this process, when small particles, typically from asteroid collisions, burn up in the atmosphere, the larger ones usually survive and land as meteorites on the ground, forming craters. According to Robbins et al. (2013) impact craters are scars of the primary exogenic modification process on earth. The impact cratering process is complex and it mostly depends on the following factors which result in craters having different shapes: (1) the target material (water, ice, sediments, or crystalline), (2) the meteorite's velocity, size, and composition, as well as the target rock's strength, and (3) the impact angle (Henkel, 1992; Raiskila, 2013). Extreme pressures that generate shockwaves that penetrate a target material are the major triggers of crater formation mechanisms. The whole impact cratering process is rapid and takes a few minutes (Raiskila, 2013). There are generally three physical stages that are involved in the formation of impact craters:

(i) *The contact and compression stage*- This starts as soon as the moving projectile contacts the earth's ground surface. On a solid target, the penetration depth of the

projectile is 1-2 times its diameter, and the shock waves are spread radially in the target (French, 1999; Raiskila, 2013). This stage results in the displacement and ejection of both the impactor and the target material, henceforth producing a crater on the target surface (Collins et al., 2012).

(ii) *The excavation stage*- Interactions between shock waves as they move outward, and the original ground surface cause the target material to move outward and upward, excavating a crater. This crater known as the transient crater is usually 10-20 times the original impactor's diameter (French & Koeberl, 2010).

(iii) *The modification stage*- This stage begins when the transient crater has grown to its maximum size (French, 1999). Gravity and tock mechanics alter the generated crater. Most impact-induced changes such as core uplifting and crater collapse occur and the crater is filled with allochthonous rocks, breccias, and melts (Raiskila, 2013). Nevertheless, this stage eventually blends into typical geologic processes that include but are not limited to mass movement, erosion, isostatic uplift, and sedimentation; it has no obvious end (French, 1999).

Based on their morphology, impact craters have been divided into simple craters and complex craters (Pilkington & Grieve, 1992; Melosh, 2011). Simple craters (Figure 1.1), have a circular bowl-shaped depression with a diameter of about 2 – 4 km (Abraham, 2004; O'Neill & Heine, 2005; Raiskila et al., 2013; Zylberman, 2017). In most cases, they have depth-to-diameter ratios of 1:5 to 1:7 (Zylberman, 2017). The central portion of simple craters is gouged out and they may have inverted edges with material such as debris-strewn a long way from the crater rims (Beard, 2012). These structures are filled with impact-generated deposits such as impact breccias and

melt rocks, as well as post-impact sediments (Melosh, 2011; Zylberman, 2017). The apparent depth for simple craters is marked by a lens of breccia (Pilkington & Grieve, 1992; Therriault et al., 2002; Melosh, 2011). This breccia includes representatives from all the formations intersected by the crater. The thickness of the lens of breccia is usually 1/2 to 1/3 of the rim-to-floor depth (Grieve, 2005; Melosh, 2011). The true crater floor contains shocked and fractured rocks (Therriault et al., 2002; Zylberman, 2017). As the diameter of terrestrial craters increases, relatively shallow structures are formed (Henkel, 1992). At an average crater diameter of 2 km and 4 km depending on whether the target rock is sedimentary or crystalline respectively, simple craters transition to complex craters (Melosh, 2011; O'Neill & Heine, 2005; Osinski, 2006; Zylberman, 2017).

Complex craters (Figure 1.2), have diameters that are greater than 4 km with a structurally complicated rim and have depth-to-diameter ratios of 1:10 to 1:20, making them shallower than simple craters (Raiskila et al., 2013; Zylberman, 2017). Complex craters, just like simple craters, have a circular shape and are filled with both impact-induced and post-impact products, and when undeformed their rims are covered by ejecta (Zylberman, 2017). These types of craters are characterized by a central uplift and a down-faulted annular trough (Osinski, 2006; Zylberman, 2017). The resistance to weathering of the central uplift is generally higher than that of the nearby crater fill. The material that makes up this part of the crater (central uplift) is derived from material that is pushed upward from the deepest levels of the crater (Melosh, 2011; Reimold & Koeberl, 2014).

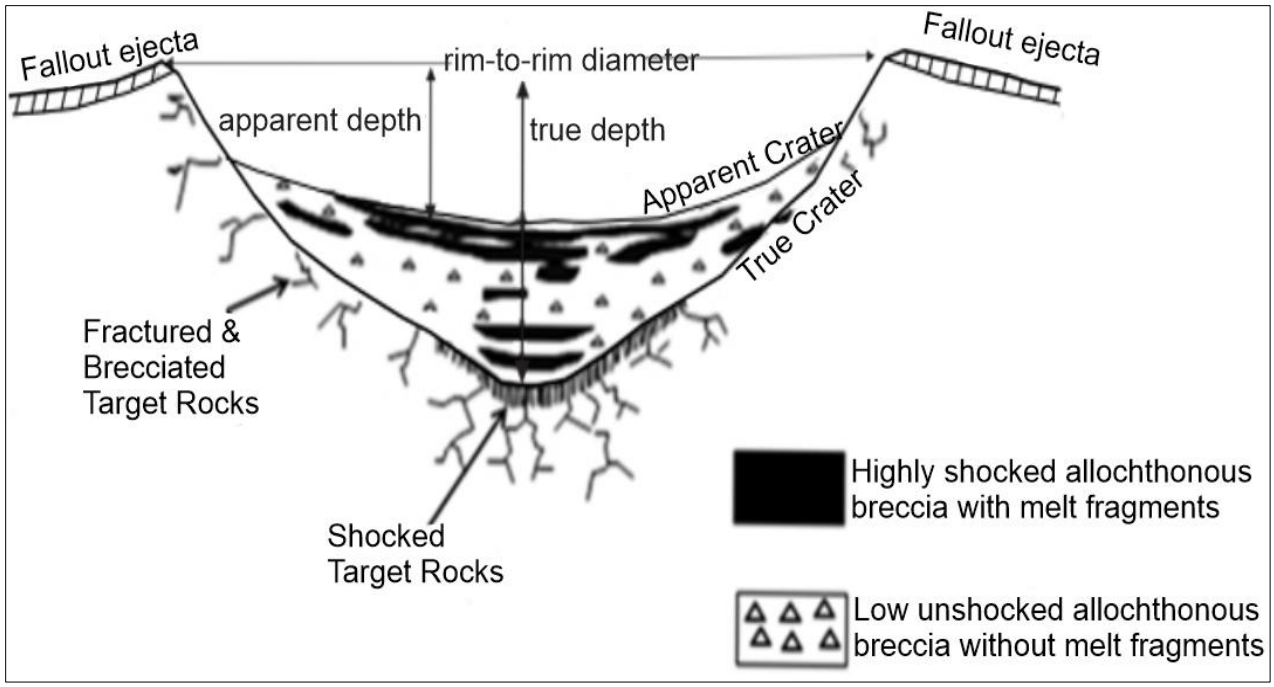

Figure 1.1. A cross-section of a simple impact crater formed in crystalline target material (Zylberman, 2017).

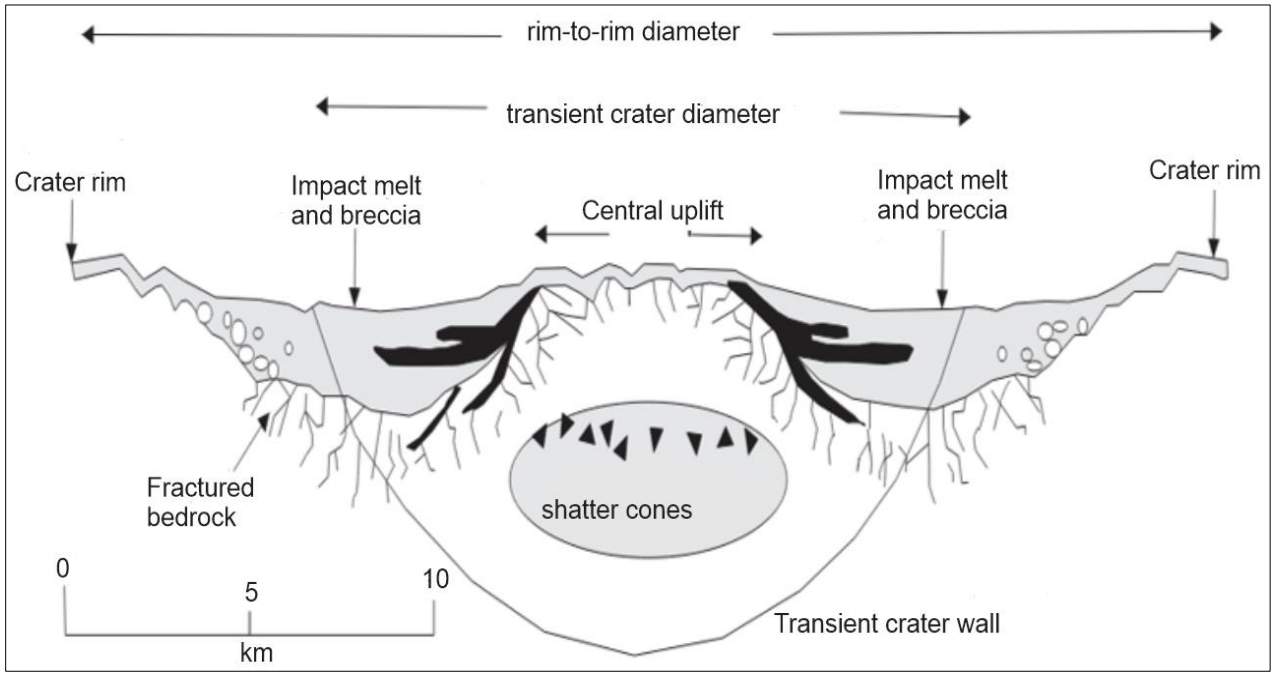

Figure 1.2. Schematic cross-section of a typical complex impact crater with central uplift (Raiskila, 2013).

As a result of increased pressure and temperature in and around craters during the impact event, unusual rocks form (Grieve, 2005; Stöffler & Grieve, 2007; Raiskila, 2013). Non-brecciated rocks, impact melt rocks, and impact breccias are the three main types of rocks that form because of the impact cratering process. Unless buried under sediments, breccias and melts are sensitive to modification and erosion. Furthermore, impacts into crystalline environments often generate more melt than impacts in sedimentary settings (Raiskila, 2013; Reimold & Koeberl, 2014). Some geological activities such as erosion, volcanic resurfacing, magnetic and other tectonic processes result in modifications of the primary morphology of these terrestrial impact structures; making it hard to recognize them from the surface (Pilkington & Grieve, 1992; Therriault et al., 2002; Henkel et al., 2010; Rebolledo-Vieyra et al., 2010). Impact structures that have been subjected to erosion may be covered by water or post-impact sediments. Furthermore, older sedimentary rocks that escaped erosion as a result of their placement in the crater depression may be missing from the crater surroundings (Henkel et al., 2010; Reimold & Koeberl, 2014).

1.2 Literature review

1.2.1 The geophysical signatures of impact structures

Terrestrial impact craters can be manifested by subsurface changes that can be identified by geophysical methods (Abraham, 2004; Raiskila, 2013). Underneath post-impact strata, some known terrestrial craters are buried, hence geophysics has played a major role in identifying many of these structures leading to their subsequent drilling and detailed geological studies (Pilkington & Grieve, 1992; Reimold & Koeberl, 2014). Nevertheless, the prominent indicative features of an impact crater are the occurrence of shock metamorphic effects (Henkel et al.,

2002; Therriault et al., 2002). Shock metamorphism is the constant breakdown in the structural order of minerals and rocks induced by the passage of high-pressure shockwaves (Therriault et al., 2002). This process necessitates pressures and temperatures exceeding those of the endogenic terrestrial metamorphic pressure-temperature field (Glikson & Uysal, 2013). These effects include the presence of impact melt, shock micro deformations like planar deformations, diaplectic glass of minerals, and high-pressure polymorphs of minerals (Henkel et al., 2002; Therriault et al., 2002; French & Koeberl, 2010). Meteorite impacts cause subsurface structural deformations which cause changes to the geophysical properties of the rocks found in and around the impact structures (Abraham, 2004). Variations in subsurface electrical conductivity, magnetic field, and mineralogical phase changes are some of these properties. These changes cause geophysical anomalies that can be used as indicators of the existence of buried structures.

Geophysical methods have an advantage over other methods because they can cover a large area of a given structure in a short time thereby overcoming problems of limited exposures. However, because the geophysical signatures of impact structures are complicated, it is vital to consider that geophysics alone does not give conclusive proof for their impact origin (Henkel, 1992; Grieve, 2005). The combined analysis and interpretation of different geophysical methods can be used to constrain and reduce the ambiguity of results obtained (Henkel, 1992). Due to the vast availability and continuous coverage of potential field data over large areas, gravity and magnetic studies have been the principal geophysical tools used for evaluation of the occurrence of probable impact structures on Earth (Therriault et al., 2002). Generally, the density distribution and magnetization of shock rocks and the immediate environment change during the impact

process, making it possible to use gravity and magnetic methods for identifying and exploring impact structures (Ferreira et al., 2015).

Uneroded impact structures are generally associated with circular negative Bouguer anomalies that can extend to, or slightly beyond the crater rim (Reimold & Koeberl, 2014; Therriault et al., 2002; Zylberman, 2017). Impact-induced fragmentation and brecciation of the target material as well as the high porosity of the crater fills, result in these gravity low anomalies (Reimold & Koeberl, 2014). For complex structures and those that have been highly eroded, the gravity anomaly patterns may become complex as the anomalies will be determined by sub-crater basement geology (Reimold & Koeberl, 2014). Large complex structures, on the other hand, are more likely to have a central gravity high that extends to around half the structure's circumference (Osinski, 2012).

Compared to gravity signatures, magnetic anomalies of impact craters are more complex. These anomalies are determined by the magnetic properties of the crater fill and sub-crater lithologies (Abraham, 2004). In addition, impact-induced heat and chemical remanence are important in determining the crater magnetic anomalies (Reimold & Koeberl, 2014). All known terrestrial impact structures normally do not show any distinctive magnetic signature patterns; the signature can be low or high. Nevertheless, magnetic low is the dominant magnetic signature over simple and some small complex craters (Pilkington & Grieve, 1992; Pilkington & Hildebrand, 2003). The presence of localized anomalies with shorter wavelengths and large amplitude, which usually occur at or near the centre of the crater, can modify the magnetic low signatures over

large impact structures (Pilkington & Hildebrand, 2003; Therriault et al., 2002). Additionally, there may be uplifted magnetic lithologies within the central uplift, which are usually crystalline basement rocks (Pilkington & Hildebrand, 2003). In impact structure studies, gravity and magnetic methods have been widely used to determine the geometry of the structures, the density and magnetization variations of the rocks in and around the craters, to estimate the uplift in sedimentary targets, and to calculate the depth to the basement (Ernstson, 1984; Talwani et al., 2003; Vasconcelos et al., 2012; Ferreira et al., 2015; El Hidayah et al., 2018).

The electrical properties of rocks in impact craters are greatly influenced by their degree of brecciation, fracturing, and fragmentation (Pilkington & Grieve, 1992). An increase in the aforementioned factors, results in the increase of water content in the pore spaces, ultimately increasing the conductivity of the rocks within and around the crater as compared to that of the unaffected surrounding rocks. Increased conductivity makes it possible for geo-electrical methods to be employed in mapping and investigating impact craters (Pilkington & Grieve, 1992). Craters are generally associated with high conductive anomalies (Bodoky et al., 2006). Electrical methods are not popular in impact cratering studies. However, the successful application of these methods has been in mapping the thickness of the post-impact sediments and breccia, both of which are identified by a high conductivity response due to their high porosity and permeability (Hawke, 2004). The few investigations that have been done using these methods involve Direct Current (DC) electrical methods like Vertical Electrical Sounding (VES) technique (Pilkington & Grieve, 1992). This method can be used to map the true crater floor, show how electrical properties change as a function of fracturing level, determine the boundary between sediments

and impact breccias and detect the base of allochthonous material (Pilkington & Grieve, 1992). Therefore, the current study was focused on employing magnetics, gravity, and electrical method to understand the geometry of the Kgagodi basin, in Central district Botswana from an impact crater point of view.

1.2.2 Previous work in the Kgagodi basin

Initial investigations on this structure by Paya et al. (1999) reported a central negative Bouguer anomaly of 10 mGal, a basin depth of ~900m and basin diameter of 3-4 km. This study also indicated presence of breccia which led to the suggestion that Kgagodi basin might be of impact origin. Nonetheless, at the time no concrete proof for impact had been found; for instance, shock metamorphic deformation effects (Reimold et al., 2000; Brandt et al., 2002; Reimold & Koeberl, 2014). Initial evidence of shock metamorphic evidence was provided by Reimold et al. (2000).

This structure's impact origin was described in detail by Brandt et al. (2002). They carried out the petrographical and geochemical analysis of samples from a drill core (240m long), obtained less than 400m inside of the crater rim. This study reported shock metamorphic effects in granitoid clasts in the brecciated zone. The breccia was classified as suevitic impact breccia due to the presence of melt and glass fragments in it. In addition, various sets of planar deformation characteristics in feldspar and quartz; diaplectic quartz, isotropized felsic minerals, and rare melt fragments were reported. Furthermore, the breccia samples were reported to contain higher quantities of siderophile elements, as well as iridium, than the target rocks, which was interpreted as indicating the presence of a minor meteoritic component (Brandt et al., 2002;

Reimold & Koeberl, 2014). Brandt et al. (2002) further reported gravity and magnetic results of six profiles which revealed: a diameter of ~3.5 km and a depth to the basement of ~900m. Furthermore, a central gravity low of up to 10 mGal, and a noisy high frequency magnetic signature around the structure was noted, confirming results by Paya et al. (1999) and Reimold et al. (2000). Reimold et al. (2000) suggested that the Kgagodi basin is similar to Brent Crater in Canada. Brent crater has a 3.6 km simple, bowl-shaped geometry and is formed in a crystalline basement environment (Reimold & Koeberl, 2014).

1.3 Problem statement

The Kgagodi basin is buried by sediments with limited outcrops in its surroundings (Brandt et al., 2002). Previous geophysical studies in the area by Reimold et al. (2000) and Brandt et al. (2002) confirmed the basin to be of impact origin. These studies classified it as a simple impact crater with a diameter of 3 to 4 km and a depth to the basement of about 900m. Currently, no study has presented a detailed and precise geometric and structural model of the basin. A review of the impact craters in Africa by Reimold and Koeberl (2014) suggested that further geophysical investigations in the basin should be carried out to determine and understand the geometry of this buried structure before any further drilling can be done.

1.4 Significance of the study

Generally, investigations of impact structures are important because: (1) they can host economic mineralization, (2) can be of significant groundwater recharge zones, and, (3) can provide a long-term record of paleo-environmental conditions (Grieve, 2005; Pati & Reimold,

2007; Reimold & Koeberl, 2014). The impact event causes fracturing and brecciation of rocks below and around impact structures, therefore providing sufficient water flow in these structures (Henkel et al., 2010; Zylberman, 2017). The Kgagodi basin has been suggested to represent an intersection of two fault lines thereby making it a prospective hydrological target (Brandt et al., 2002; Reimold & Koeberl, 2014).

According to Earth Impact Database (2018), the Kgagodi basin is by far the oldest confirmed simple crater in Southern Africa and the first confirmed impact crater in Botswana. Investigating the Kgagodi basin allows understanding of the impact process and its effects on geological formations. In addition, the results of the study will aid future scientific investigations and guide drilling initiatives in the basin.

1.5 Aims and objectives

Aim: To delineate the geologic structures within the Kgagodi basin and determine the 3-D geometry of the Kgagodi basin.

Objectives:

- To Investigate the structural characteristics and evolution of the basin, from analysis of existing high-resolution aeromagnetic data,
- To evaluate the basin fill thickness and morphology of the basin by interpretation of ground gravity data,
- To investigate the shallow geoelectrical units within the basin using the Vertical Electrical Sounding (VES) technique.

Chapter 2

The study area

2.1 Location and general description

The Kgagodi basin structure is located at 22°28'26.67"S and 27°34'54.10"E, about 7 km South of the Kgagodi village, Central Botswana (Figure 2.1). This structure is along the old Maunatlala-Kgagodi road and on the North-eastern side of the Tswapong hills (Brandt et al., 2002). Aerial photography and satellite imagery of the area provided the first indications of the basin (Brandt et al., 2002). The area around the Kgagodi basin is flat. Except for the calcrete deposits, no outcrops can be observed from the satellite image (Figure 2.1). The rims of the Kgagodi basin are marked by sporadic calcrete exposures (Brandt et al., 2002).

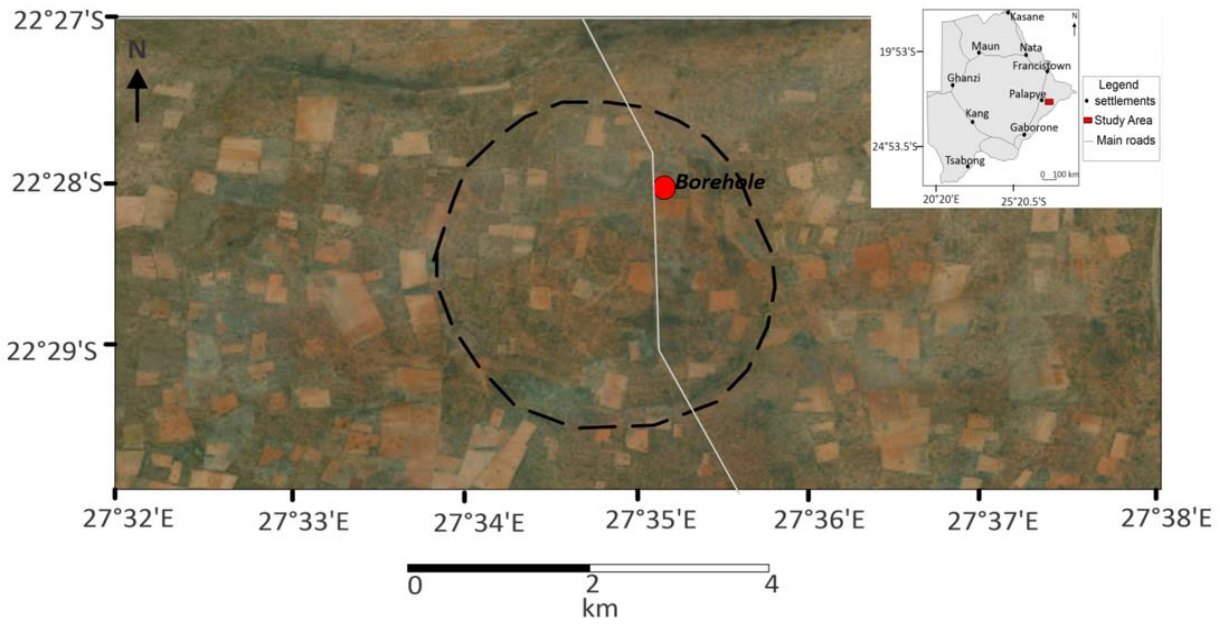

Figure 2.1. Google image showing the topographic expression of the Kgagodi basin. In the top, right Insert is a map of Botswana showing the approximate location of the Kgagodi basin. The black dashed line in the google image represents the estimated boundary derived from google earth and the grey line is the old Kgagodi-Maunatlala road. The red dot is the location of the borehole used by Brandt et al. (2002).

2.2 Geologic and tectonic setting

The Kgagodi basin is located in the Central Zone of the Limpopo Mobile Belt (McCourt & Vearncombe, 1992; Key & Ayres, 2000; Brandt et al., 2002). The Limpopo Mobile Belt is a high-grade metamorphic terrain characterized by major structures trending North-South and it is made up of Archean to Paleoproterozoic rocks (McCourt & van Reenen, 1992; Key & Ayres, 2000; Brandt et al., 2002; Zeh et al., 2007). The central zone of the Limpopo Mobile Belt in Botswana is further divided into two; the Phikwe complex and the Mahalapye complex. Within the central zone, the Kgagodi structure is situated in the Phikwe Complex (Figure 2.2), which composes of Archean hornblende-bearing, trondjemitic, tonalitic gneisses, igneous rocks, and metasedimentary rocks (Key & Ayres, 2000; Zeh et al., 2007). Local occurrences of quartzites, Banded Iron Formation (BIFS), biotite shists, and metamorphosed basic/ultrabasic intrusions are also present in the Phikwe complex (Aldiss, 1991).

Limited exposures of Archean high-grade gneisses, amphibolites, ultramafics, migmatites, and granitic gneisses are found in the region around the Kgagodi basin (Brandt et al., 2002). Overlaying the Archean lithologies are metasedimentary rocks belonging to the Palapye Group (Figure 2.3). In addition, younger formations in the area include Karoo sediments and some Karoo dolerite intrusions (Brandt et al., 2002). There are some occurrences of Karoo dolerite in several hills which are less than 1 km from the structure and scattered exposures of amphibolite and loose boulders occur on the southern part of the structure (Brandt et al., 2002). No shock metamorphic markers e.g., macro deformation can be noticed in and around the basin (Brandt et al., 2002).

According to Brandt et al. (2002) the stratigraphy of the Kgagodi basin can be derived from the drill core obtained less than 400 m from the edge of the structure (Figure 2.4). Brandt et al. (2002) summarized this drill core as follows: the upper 60 m is made up of unconsolidated sands with different amounts of carbonate material as calcrete and marl layers. From 60m to 158m marl or limestone is intersected. At 158, about 5m of poorly consolidated, coarse, breccia is found, overlain by the sediments. Thereafter, a fractured granitoid basement made up of varying lithologies that include leucogranite, granodiorite, diorite, and minor amphibolite is encountered at ~164m. This fractured layer eventually grades into a less fractured and finally fresh basement with increasing depth. In between the fractured basement, at ~240m, a 1 cm thick band of breccia made of granitoid-derived clasts in a weathered matrix is encountered. It is suggested that this band could signify a possible injection into or a local formation of a melt in the crater floor (Brandt et al., 2002). Finally, the undeformed basement was intersected at ~254m.

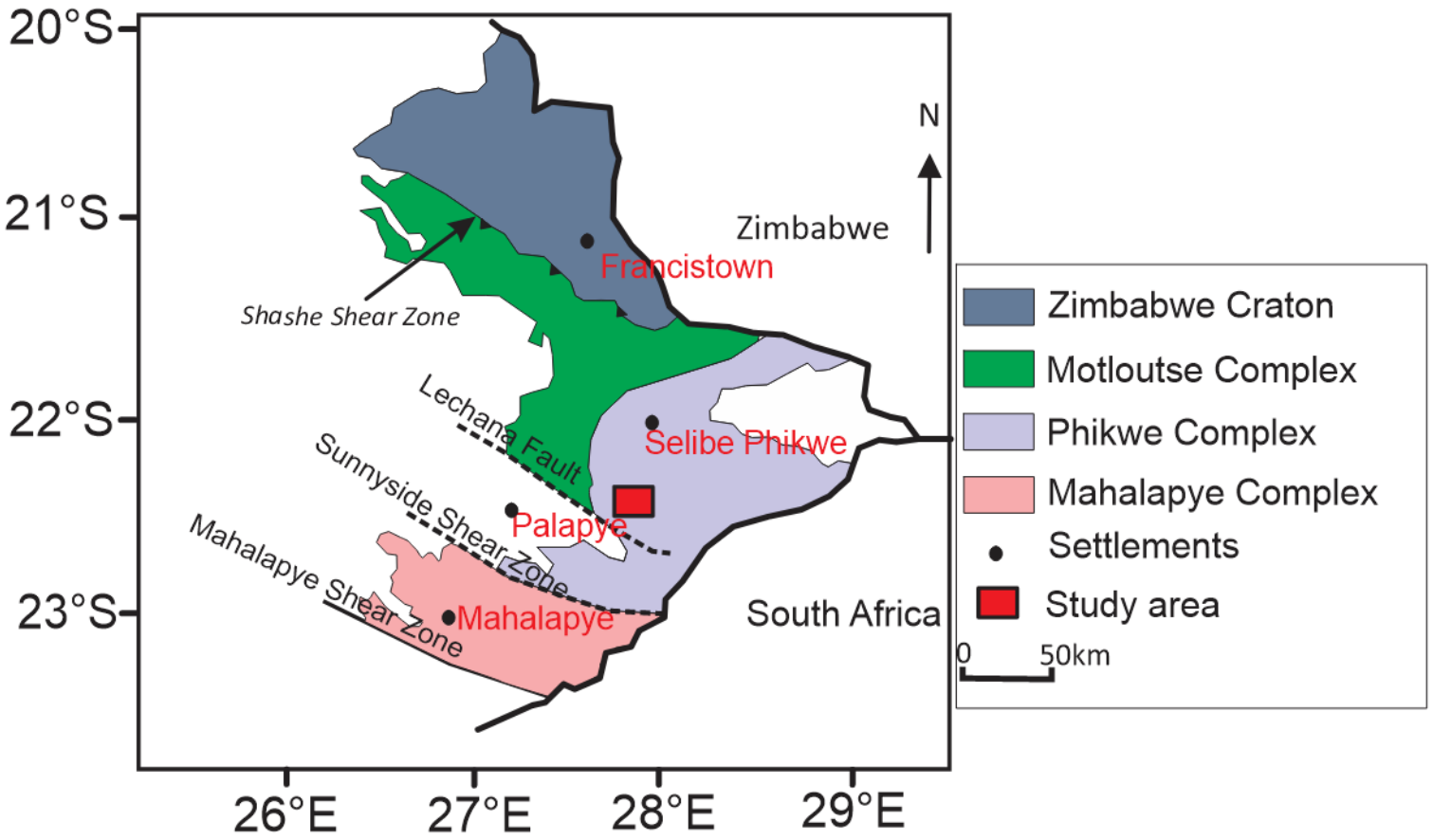

Figure 2.2. Map showing the location of the Kgagodi basin and the Archean to Paleoproterozoic terrains in eastern Botswana (McCourt et., al 2004).

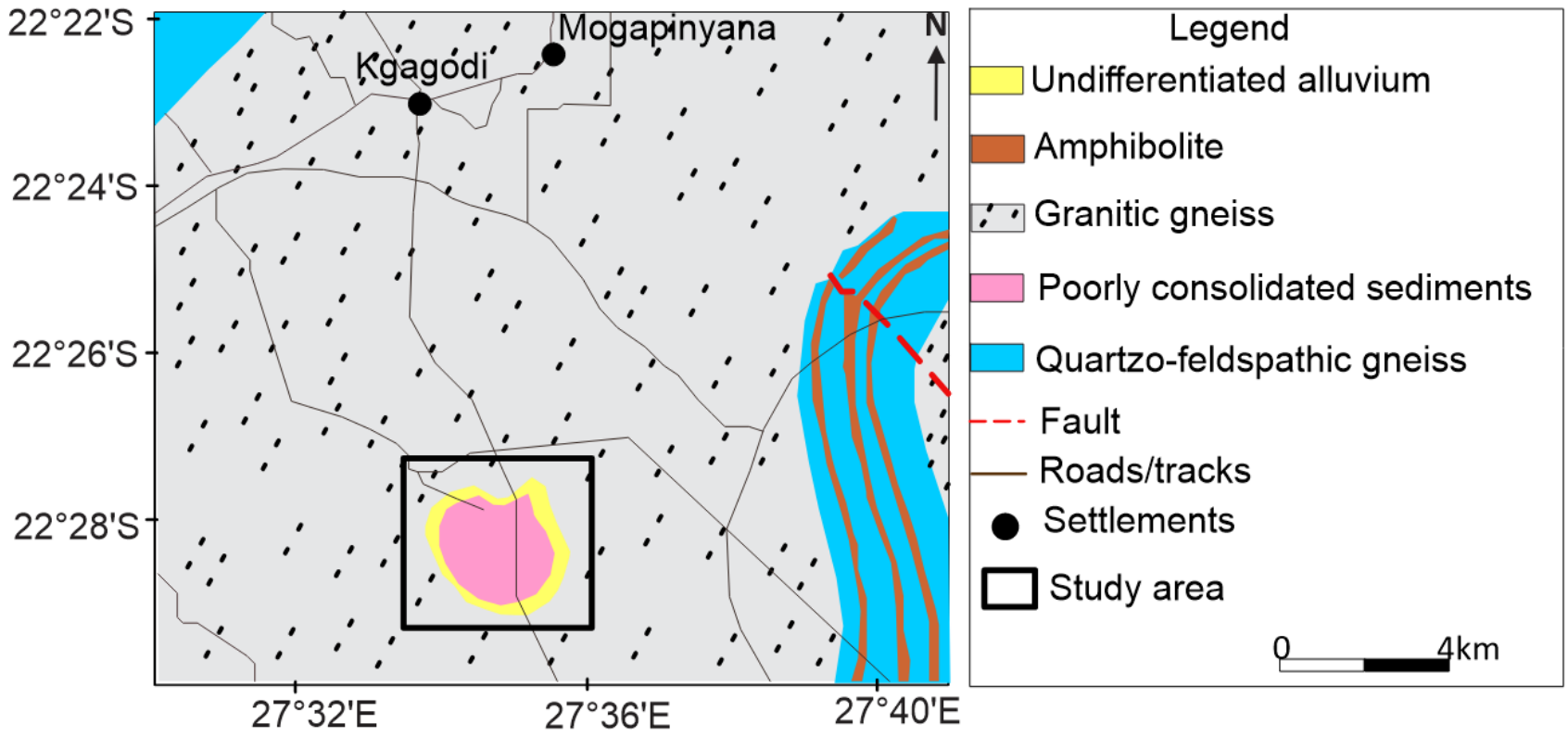

Figure 2.3. Geology of the Kgagodi basin and surrounding areas (Brandt et al.,2002).

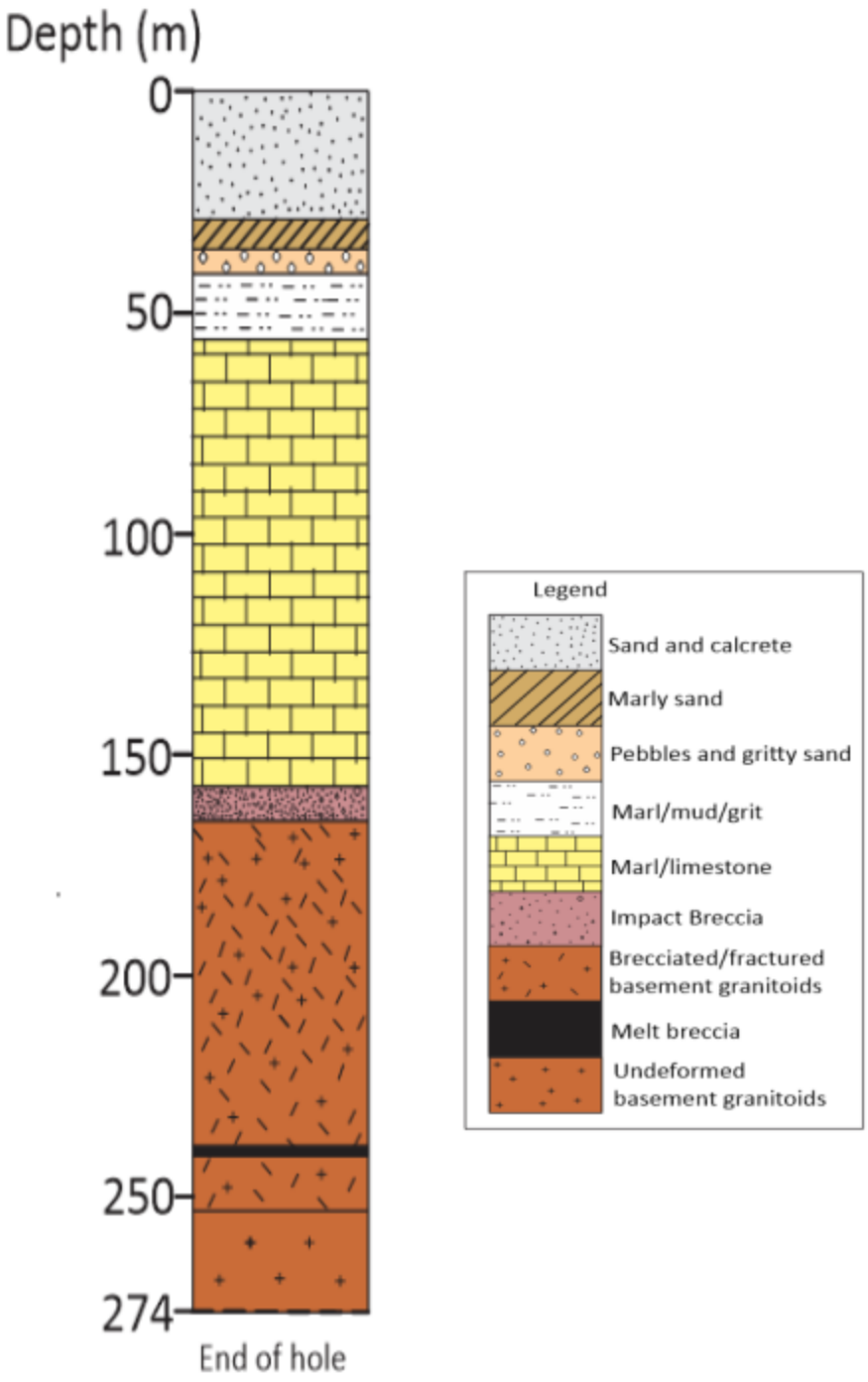

Figure 2.4. Schematic borehole log for the drill core obtained in the Kgagodi basin (Brandt et al., 2002).

Chapter 3

Materials and methods

3.1. Magnetic method

3.1.1 Theoretical fundamentals of the method

The magnetic method measures the existing magnetic field strength; It does not strengthen or change it, therefore it is referred to as a passive geophysical method (Haldar, 2018). This method is used to investigate variances in the Earth's magnetic field which are caused by the magnetic properties of the existing primary rocks (Kearey et al., 2002). The Earth's magnetic field is a dipole; thus, it has a positive and a negative magnetic pole. A force **F**, existing between two magnetic poles having strength m_1 and m_2, separated by distance r, is given by equation 1.1. If the poles are the same, they will repel and if the poles have an opposite polarity, the force will pull the poles towards each other (Kearey et al., 2002; Reynolds, 2011).

$$\mathbf{F} = \frac{\mu_0 m_1 m_2}{4\pi \mu_R r^2} \quad \text{.....} \quad (1.1)$$

Where μ_0 and μ_R are constants corresponding to the magnetic permeability of the vacuum and the relative magnetic permeability of the medium separating the poles.

In a magnetic survey, to measure the force due to a magnetic field, a more practical **F** is needed (Casto, 2001). The magnetic field strength **B** is defined as the force applied on a unit positive pole of strength at a distance r from the pole (Kearey et al., 2002). It is expressed by equation (1.2).

$$\mathbf{B} \equiv \frac{\mu_0 \mathrm{m}}{4\pi\, \mu_R \mathrm{r}^2} \quad \text{.....} \quad (2.2)$$

Magnetic fields are produced as a direct result of the flow of electric current (Casto, 2001; Kearey et al., 2002; Reynolds, 2011). A current flowing through a circular loop act as a magnetic dipole in the loop's centre (Casto, 2001). The magnetizing force **H** arises when a current is passed through a coil consisting of several turns of wire, resulting in the flow of magnetic flux through and around the coil annulus. The magnetic field **B**, of the coil, is the density of the magnetic flux or closeness of the flux lines, measured over an area perpendicular to the flow direction (Kearey et al., 2002; Reynolds, 2011). The magnetic moment **M**, of a dipole with poles of strength m separated by a distance l apart, is given by:

$$\mathbf{M} = \mathrm{ml} \quad \text{.....} \quad (1.3)$$

The magnetic moment **M,** of a current-carrying coil, is proportional to its number of turns, cross-sectional area A, and current magnitude I, (equation 1.4), and it is expressed as Am^2 (Casto, 2001; Kearey et al., 2002).

$$\mathbf{M} = \mathrm{iA} \quad \text{.....} \quad (1.4)$$

When a material is exposed to a magnetic field, it becomes magnetized in the field's direction. This field is lost when the material is removed and is referred to as induced magnetization or magnetic polarization (Casto, 2001; Kearey et al., 2002). The alignment of elementary dipoles within the material in the direction of the field causes this magnetization (Kearey et al., 2002).

The dipole moment per volume of a material describes the intensity of the induced magnetization $\mathbf{J_i}$ (equation 1.5). Where **M** is the magnetic moment, V is the unit volume of the material and $\mathbf{J_i}$ is expressed in Am^{-1}.

$$\mathbf{J_i} = \frac{\mathbf{M}}{\mathrm{V}} \qquad \text{.....} \qquad (1.5)$$

The degree to which a material can be magnetized is known as magnetic susceptibility (k) (Casto, 2001; Kearey et al., 2002; Reynolds, 2011). This is the most important physical property measured in magnetic methods and it is defined by equation (1.6).

$$\mathrm{k} = \frac{\mathbf{J_i}}{\mathbf{H}} \qquad \text{.....} \qquad (1.6)$$

Where, $\mathbf{J_i}$ is the intensity of magnetization, **H** is the magnetization field, and are both measured in Am^{-1}.

In the absence of an applied field **H**, there is still detectable intensity of magnetization that is maintained by the internal field strength resulting from permanent magnetic particles (Reynolds, 2011). This permanent magnetisation is called remanent magnetisation. In a rock containing magnetic minerals, there will be both induced and remanent magnetization (Figure 3.1), which may have varying strengths and directions (Clark & Emerson, 1991; Kearey et al., 2002; Reynolds, 2011).

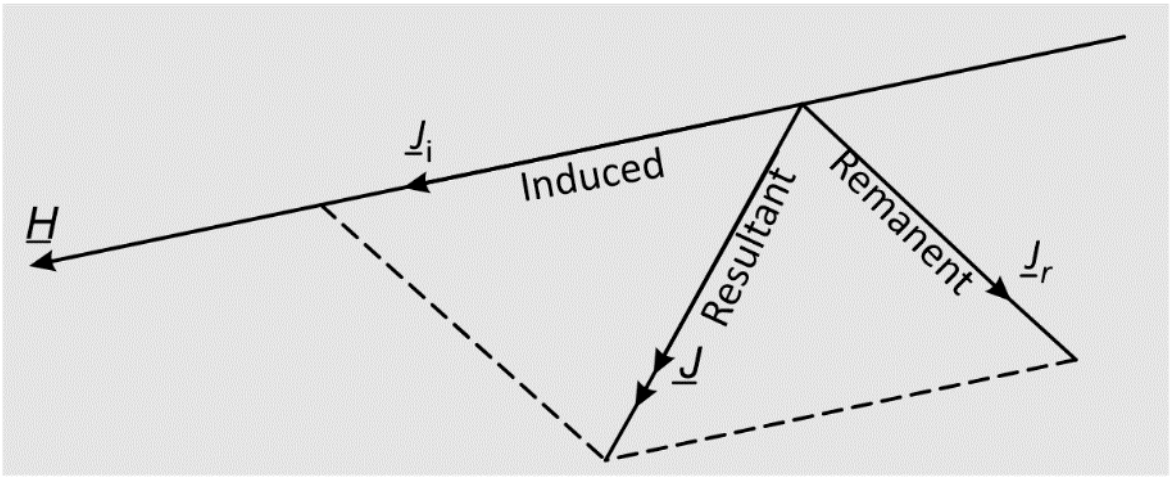

Figure 3.1. Vector diagram showing the relationship between remanent (J_r), induced (J_i), and total magnetization components Reynolds (2011).

A material's magnetic behaviour is defined by the arrangement of atomic dipoles within the material (Casto, 2001). Materials can be categorized as either diamagnetic or paramagnetic. Diamagnetic materials like halite have weak and negative susceptibility. Materials that are paramagnetic such as amphiboles, pyroxenes, olivines, garnets, and biotite a weak positive susceptibility which is generally at least an order of magnitude stronger than diamagnet materials (Casto, 2001; Kearey et al., 2002; Reynolds, 2011). Basic igneous rocks normally have high magnetic susceptibilities because of the high magnetite content (Kearey et al., 2002). Intermediate-to-low susceptibility values characterize acidic igneous and metamorphic rocks whereas sedimentary rocks have quite low susceptibility values (Figure 3.2).

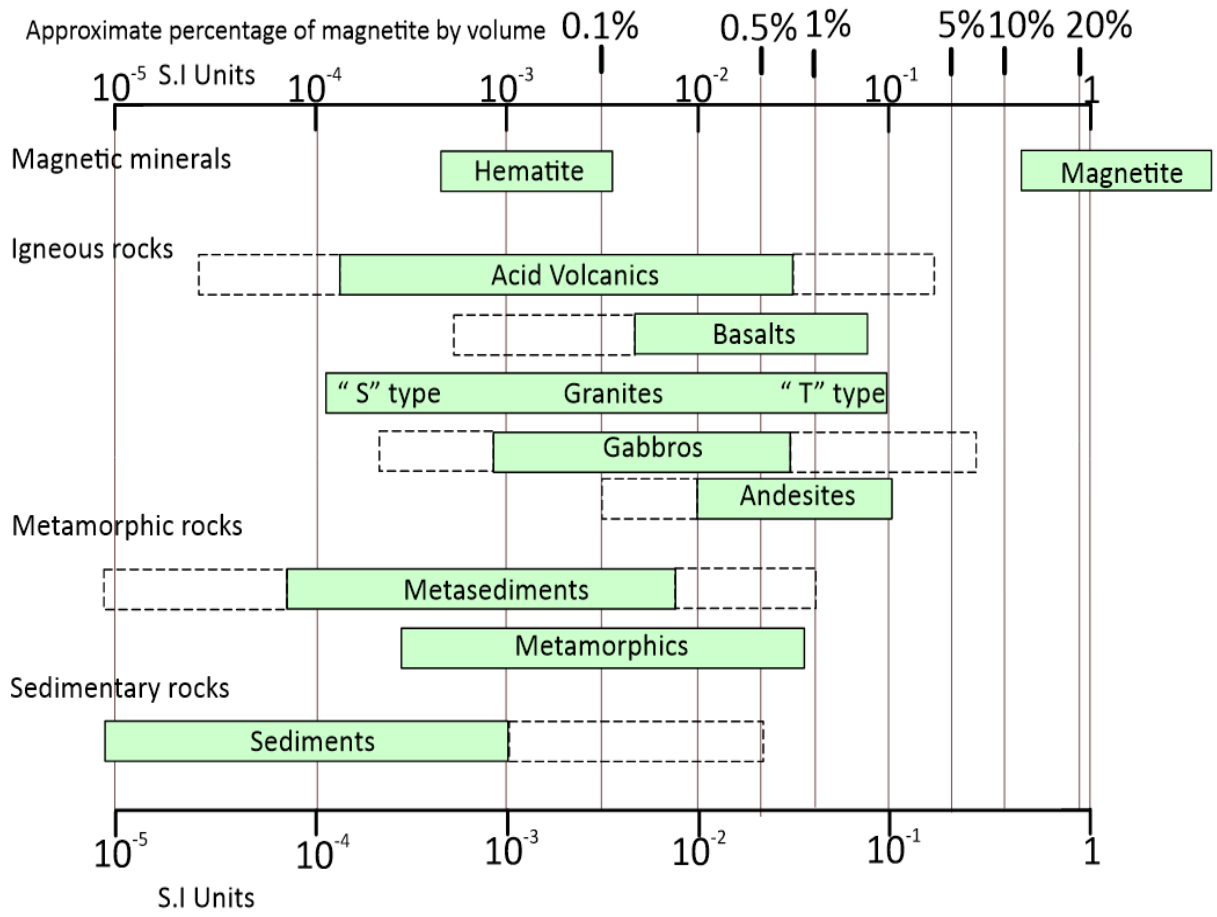

Figure 3.2. Magnetic susceptibilities for some common minerals and rock types. Adapted from Clark and Emerson (1991).

The geomagnetic field is the consequence of localized effects overlaid on the Earth's normal magnetic field, resulting in magnetic anomalies caused by the behaviour of underlying rocks (Kearey et al., 2002). It is a result of electric currents induced within the conductive liquid outer core because of slow convective movements within it (Reynolds, 2011). This field has certain elements that describe its magnitude and direction at any given point (Figure 3.3). These elements are the declination D, inclination I, and the total field vector **F** (Kearey et al., 2002; Reynolds, 2011; Haldar, 2018). **F** has a vertical component Z and a horizontal component H in the

direction of the magnetic north. The inclination I is the dip of **F** and the horizontal angle between geographic and magnetic north is the declination D (Reynolds, 2011; Haldar, 2018).

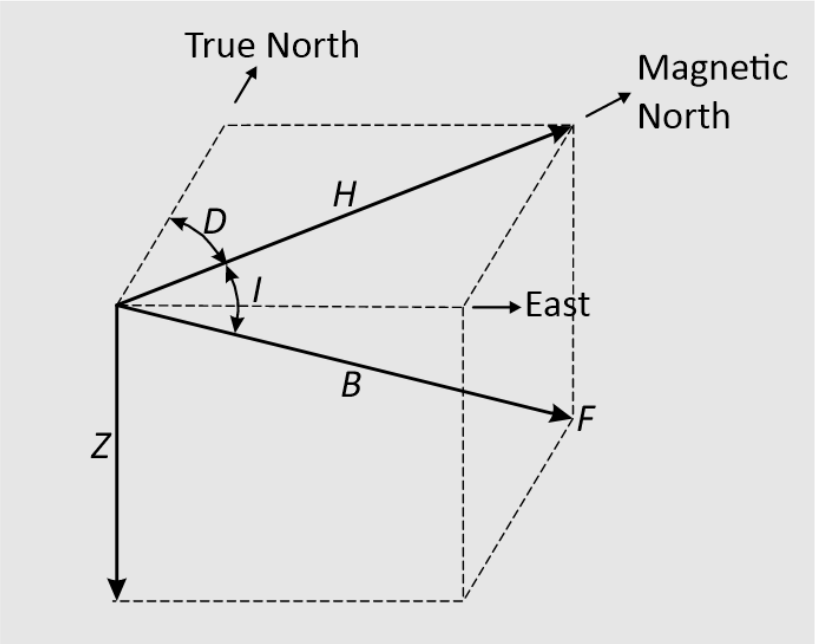

Figure 3.3. Schematic diagram of geomagnetic elements; the inclination (I), the declination (D) of the total field vector (**F**) (Kearey et al., 2002).

The common magnetic surveys are ground surveys and aeromagnetic surveys. Ground surveys are normally carried out over quite small areas on a previously identified anomaly/target (Kearey et al., 2002). Airborne magnetic surveys are carried out using an aircraft and are used for regional surveys. Compared to land surveys, aeromagnetic surveys are fast and cost-effective.

3.1.1.1 Data enhancement techniques

Reduction to pole (RTP)

Magnetic anomalies are naturally shifted laterally from the causative body, complicating their interpretation (Abraham, 2004). The reduction to pole filter (equation 1.71), simplifies the shapes

of magnetic anomalies and overcomes undesired distortions like shape, size, and location due to the effects of the inclination of the Earth's magnetic field (Ibraheem et al., 2018). The anomalies are translated so that they are centred directly above the causative body/magnetic source (Abraham, 2004; Ibraheem et al., 2018).

$$L(\theta) = \frac{1}{(\sin I_a + i \cos I \,.\, \cos(D - \theta))^2} \quad \text{.....} \quad (1.71)$$

Where I is the geomagnetic inclination, I_a is the Inclination for amplitude correction (which is never less than 1) and D is the geomagnetic declination.

Regional- residual separation

Magnetic anomalies observed in geophysical surveys include the superposition of the effects of all underground magnetic sources (Li & Oldenburg, 1998; Tsivouraki-Papafotiou et al., 2003). Targets in small-scale surveys are usually small, shallow depth anomalies that are embedded in a regional field arising from larger and deeper magnetic anomalies with long wavelengths. Estimation and removal of the regional field produce the residual field caused by the target sources (Li & Oldenburg, 1998; Tsivouraki-Papafotiou et al., 2003; Ilugbo et al., 2020). The reliability of interpretation of magnetic data is best attained when conducted on the residual data field (Li & Oldenburg, 1998).

Analytical signal

This filter is used for edge detection and depth estimation of causative bodies (Ndlovu et al., 2015). The Analytic signal (equation 1.72) is computed in three dimensions, as the magnitude of

the sums of the square root of the vertical and horizontal components of the magnetic response (Osinowo & Taiwo, 2020; Ejike Kingsley et al., 2021).

$$\mathrm{AS} = \sqrt{\left(\frac{\partial \mathrm{T}}{\partial \mathrm{x}}\right)^2 + \left(\frac{\partial \mathrm{T}}{\partial \mathrm{y}}\right)^2 + \left(\frac{\partial \mathrm{T}}{\partial \mathrm{z}}\right)^2} \quad \text{..... (1.72)}$$

Where T is the observed magnetic field at (x, y, z) directions.

Its form over the causative body does not depend on its magnetization direction but on the horizontal coordinate and depth (Ansari & Alamdar, 2009; Ndlovu et al., 2015). This data enhancement method is ideal because its amplitude function is always positive and does not need to make any assumptions about the direction of the magnetization of the source body (Jeng et al., 2003; Ndlovu et al., 2015).

Tilt angle or tilt derivative

The arctangent of the ratio of the vertical derivative of the potential field and its total horizontal derivative gives the tilt angle or tilt derivative (Ibraheem et al., 2019; Yeomans et al., 2021). The tilt angle is defined by equation 1.73 (Miller & Singh, 1994; Verduzco et al., 2004; Salem et al., 2008; Ibraheem et al., 2019).

$$\mathrm{TDR} = \theta = \tan^{-1}\left(\frac{\mathrm{VDR}}{\mathrm{THDR}}\right) \quad \text{..... (1.73)}$$

Where VDR and THDR are the vertical and total horizontal derivatives of the total magnetic intensity **M**, respectively.

$$\mathrm{VDR} = \frac{\partial \mathrm{M}}{\partial \mathrm{z}} \quad \text{..... (1.74)}$$

$$\mathrm{THDR} = \sqrt{\left(\frac{\partial \mathrm{M}}{\partial \mathrm{x}}\right)^2 + \left(\frac{\partial \mathrm{M}}{\partial \mathrm{y}}\right)^2} \text{..... (1.75)}$$

Where $\frac{\partial \mathrm{M}}{\partial \mathrm{x}}$ and $\frac{\partial \mathrm{M}}{\partial \mathrm{y}}$ are the two horizontal derivatives of the observed magnetic field **M**.

Therefore, the total horizontal derivative is defined as:

$$\mathrm{HD_{TDR}} = \sqrt{\left(\frac{\partial \mathrm{TDR}}{\partial \mathrm{x}}\right)^2 + \left(\frac{\partial \mathrm{TDR}}{\partial \mathrm{y}}\right)^2} \text{..... (1.76)}$$

The tilt derivative and its total horizontal derivative have been reported to be highly suitable for mapping geologic structures, magnetic fabric, lineaments, depths, determining the boundary of the source anomaly, and resolving basement structures (e.g. Fairhead et al., 2004; Yeomans et al., 2021).

First vertical derivative

The vertical derivative (VD) is generally applied to the total magnetic field data to enhance shallow sources. This filter attenuates deep-seated long-wavelength anomalies by resolving interfering effects of nearby anomalies thereby enhancing the magnetic components that are caused by shallow structures and it is insensitive to noise (Tarlowski et al., 1997; Ahmed et al., 2018; Tawey et al., 2020).

The first vertical derivative is used to delineate shallow lineaments, fractures, and faults by making their edges sharper (Tawey et al., 2020). Furthermore, it gives a better resolution to closely spaced magnetic sources since it is much more responsive to local influences than to broad or regional effects (Reeves, 2005; Bala et al., 2017; Tawey et al., 2020). The higher-order vertical derivatives (i.e. second order, third order, and above) can also be computed to pursue the high-resolution effect further, but this increases the noise-to-signal ratio, especially above the second vertical derivative (Reeves, 2005). This transform (equation 1.77) is a component of the rate of change of the anomaly values as the potential field data are upward continued (Ahmed et al., 2018).

$$(\mathrm{VD}) = \frac{\partial \mathrm{T}}{\partial \mathrm{Z}} \quad \text{..... (1.77)}$$

Where, $\frac{\partial \mathrm{T}}{\partial \mathrm{Z}}$ is the magnetic field in the Z direction.

3.1.1.2 Depth estimates

Euler deconvolution

This algorithm is considered a powerful tool for providing automatic initial estimates of the locations, depths, and delineation of a wide variety of geologic structures (Reid, 2003; Cooper, 2004; Zahra & Oweis, 2016). This depth estimation method is based on Euler's homogeneity equation (equation 1.8), where the magnetic field and its gradient are related to the location of the source of an anomaly. The degree of homogeneity is expressed as the structural index (SI) (Suleiman et al., 2020).

The depth estimates provided by this method are less determined than the positional estimates (McDonald et al., 1992; Ranganai et al., 2008). It has frequently been used in automatic interpretation because it requires no prior information on the source direction and assumes no particular interpretation model (Zahra & Oweis, 2016). Although it is an automated interpretation technique, the optimal use of the algorithm depends on the user's prior knowledge of the geology of the area, the quality of the data, and the selection of the processing parameters (McDonald et al., 1992; Ranganai et al., 2008; Finn & Anderson, 2015). In this method, simple magnetic bodies have assigned values of the structural index (SI) (McDonald et al., 1992; Reid, 2003). SI is the degree of fall of the field with distance from the causative body (Suleiman et al., 2020). Typical SI values are shown in Table 1. The standard 3-D form of Euler's equation is defined by equation 1.8 (Reid et al., 1990; Suleiman et al., 2020).

$$x\frac{\partial T}{dx} + y\frac{\partial T}{dy} + z\frac{\partial T}{dz} + \eta T = x_0\frac{\partial T}{dx} + y_0\frac{\partial T}{dy} + z_0\frac{\partial T}{dz} + \eta b \quad \cdots\cdots (1.8)$$

Where x, y, and z are coordinates of a measuring point; x_0, y_0, and z_0 are coordinates of the source location whose total field is detected at x, y, and z. b is the base level. η is the structural index and **T** is the potential field.

Table 3.1. Structural indices for Euler deconvolution of magnetic anomalies (Reid, 2003; Finn & Anderson, 2015).

Structural Index	Geologic Model/Source type	Depth type
0	Contact of considerable depth extent or high throw fault	Depth to top
0.5	Contact/edge/fault of intermediate relief or throw	Depth to top

1	Sill, dike, or low throw fault/Contact	Depth to top
2	Pipeline, narrow kimberlite pipe, etc	Depth to centre
3	Sphere or compact body at a distance	Depth to centre

3.1.2 Kgagodi basin pre-processed aeromagnetic data

Regional pre-processed aeromagnetic data of the Kgagodi basin was provided by Botswana Geoscience Institute, formerly the Department of Geological Surveys. The aeromagnetic data of Botswana was collected by several exploration companies and the government of Botswana, from 1962. These surveys were generally flown at a mean clearance of 80m in the direction N-S at a spacing of 200m. Recent surveys (2010-2011) of the whole country where tie lines running from E-W at 50m spacing, were conducted by Xcalibur Airborne Geophysics. In all the surveys, the main magnetic field was calculated using the International Geomagnetic Reference Field (IGRF). This data was provided as a grid with a 50m pixel size. It was projected to Botswana National Geodetic Reference System02 (BNGRS02), Projected Coordinate System (PCS), COLLINS coordinate system using the Geodetic Reference System of 1980 (GRS,1980) (Ramotoroko et al., 2021).

In the current study, from the pre-processed total magnetic field (TMI) data, a 6 km X 6 km grid was windowed for structural interpretation of the study area using the Geosoft Oasis Montaj™ package. This grid was reprojected to UTM coordinate system zone 35S. A regional-residual separation was carried out on the TMI grid. To carry out this separation, the Butterworth

filter was applied. This filter allows the user to control the sharpness of the filter around the wavelength cut-off unlike other low and high pass filters which result in ringing. Ringing is known as the Gibbs phenomenon, and it usually manifests as waves originating from the edges of high amplitude anomalies (Li & Oldenburg, 1995). In addition, if ringing is observed the degree can be reduced until acceptable, therefore making the Butterworth filter good for applying straightforward high-pass and low-pass filters. The reduction to pole (RTP) was applied to the total field residual anomaly grid. Magnetic field parameters used to produce the RTP map at this location are Inclination I=-60.5, declination D=-13.6, and magnetic strength= 28952.25 nT. In the current study, the analytic signal, tilt angle, and the first-order vertical derivative were applied to the RTP of the residual grid.

Depth estimates to the top of magnetic sources (Euler deconvolution) were also carried out using the RTP of the residual grid. A structural index of 1 corresponding to Sill, dike, or low throw fault/contact as indicated by table 1 was used. An appropriate window size must be used (Suleiman et al., 2020). The window size must be small enough to capture features of interest but not too large that multiple anomalies are included (Finn & Anderson, 2015). To convert the window size to ground units the number of cells in window size is multiplied by the grid cell size. This data's grid cell size is 50m, which is 1/4 of the line separation distance (200m). After multiple attempts, the window size that gave the largest number of good solutions was 10, which corresponds to 500m in ground units. Additionally, an accurate flight height is important because if a poor flight height is used the depth estimates will be degraded (Finn & Anderson, 2015). The flight elevation used was 80m. The aeromagnetic data processing workflow for this study is summarized in Figure 3.4.

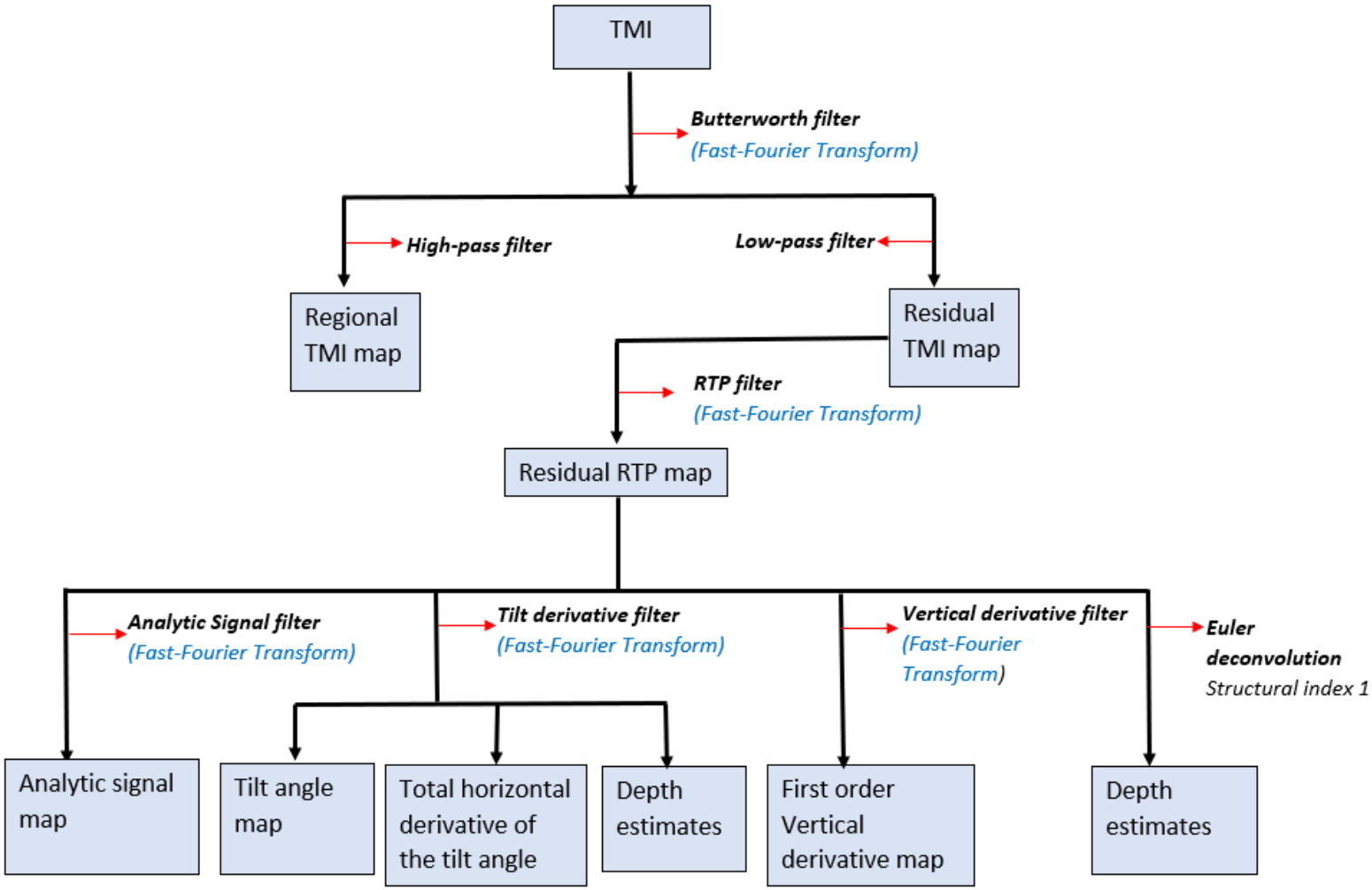

Figure 3.4. Aeromagnetic data processing workflow chart. The red horizontal arrows indicate processes/filters involved and black vertical arrows show the end products of processing.

3.2 Gravity method

3.2.1 Theoretical fundamentals of the method

The gravity method is based on Sir Isaac Newton's two laws; the Universal law of gravitation and the Second law of motion (Kearey et al., 2002; Reynolds, 2011). Newton's universal law of gravitation states that a particle attracts another particle using force **F**. The force is directly proportional to the product of their masses m_1 and m_2 and inversely proportional to the square of the distance r, between their centres (Kearey et al., 2002; Reynolds, 2011; Haldar, 2018).

$$\mathbf{F} = \frac{Gm_1m_2}{r^2} \quad \text{.....} \quad (2.0)$$

Where the gravitational constant (G) =6.67 $X10^{-11}$ N m^2 kg^{-2}.

Newton's second law of motion states that a force, **F** is equal to mass, m times acceleration, g (equation 2.1). If the acceleration is in the vertical direction, it is caused by gravity (Reynolds, 2011).

$$F = m \times g \quad \text{.....} \quad (2.1)$$

Combining equations (2.1) and (2.2):

$$F = \frac{Gm_1m_2}{r^2} = m \times g \text{.....} \quad (2.11)$$

Therefore

$$g = \frac{G \times M}{R^2} \quad \text{.....} \quad (2.2)$$

Where *g* is the gravitational acceleration.

Although gravity is measured in g.u, these units have not yet been widely accepted hence mGal and μGal are still used (Kearey et al., 2002). 1 g.u is equivalent to 0.1 mGal (10 g.u = 1 mGal). Gravity readings define contrast in densities within the Earth. This method works best when there is a difference in the mass of buried objects, caused by the difference in their densities with the surrounding medium (El Hidayah et al., 2018). Density variation is dependent on the material of which the rock consists, the degree of consolidation, and the porosity (Kearey et al., 2002; Reynolds, 2011). Igneous and metamorphic rocks have little to no porosity hence the composition of these rocks is the main cause of density variations. In sedimentary rocks, porosity is the main cause of density variation. Moreover, density generally increases with the depth, compaction, and age of the rock due to cementation.

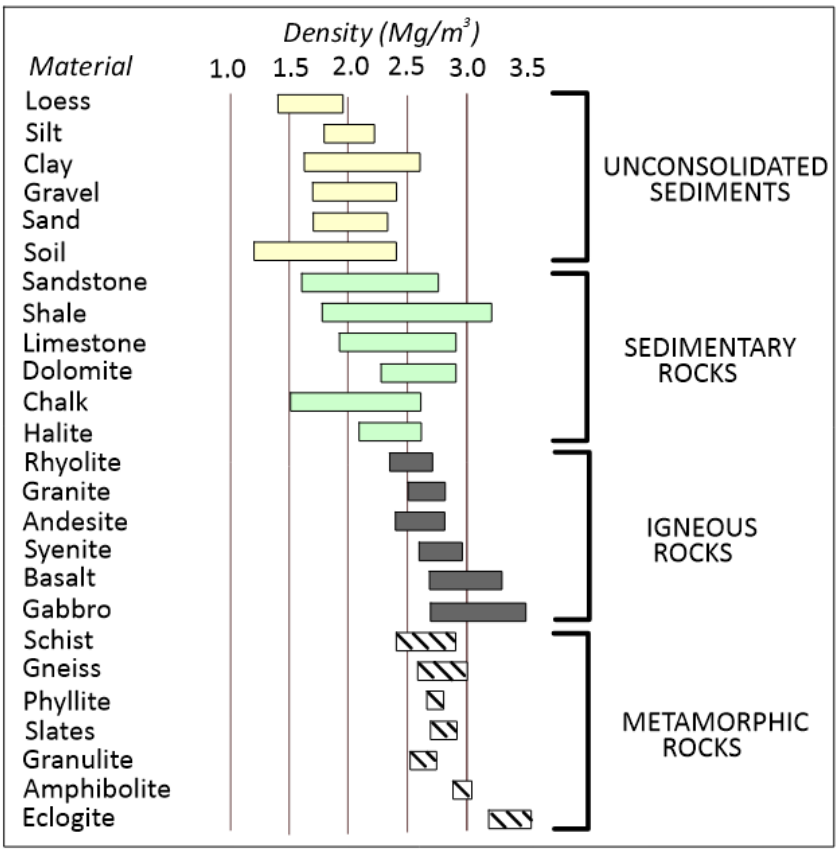

Figure 3.5. Variations in rock density for different rock types (Reynolds, 2011).

3.2.1.1 Gravity data corrections

Before gravity data can be interpreted it is subjected to some corrections to account for variations in the Earth's gravitational field that are not caused by differences in the underlying rock densities (LaFehr, 1991; Kearey et al., 2002). This data has to be corrected to a common datum such as the sea level (geoid) to remove the effects of features that are of indirect geologic interest (Kearey et al., 2002; Reynolds, 2011).

Drift correction

When a relative gravimeter is left at the same place, the measurement recorded tends to change slowly (or drift) due to thermally induced variations in the elastic characteristics of the gravimeter spring (Williams, 2008; Reynolds, 2011; Pumphrey, 2014). This is called instrumental drift. To account for this effect, repeated readings at a base station are recorded at the beginning and the end of the day/survey (Kearey et al., 2002; Pumphrey, 2014). Assuming that the drift between repeated measurements has been linear, the linear drift can be subtracted from all other readings (Blakely, 1996; Kearey et al., 2002). The difference in gravity between an observation point and the base is found by multiplying the difference in meter reading by the calibration factor of the gravimeter (Kearey et al., 2002; Reynolds, 2011). The absolute gravity at an observation point (g_{obs}) can be derived from the known gravity at the base (Kearey et al., 2002).

Latitude correction

Due to the non-spherical shape of the Earth, gravity varies with latitude (Kearey et al., 2002; Mallick et al., 2012). Gravity increases from zero at the poles to a maximum at the equator. The

variation of gravity with latitude is explained by the normal gravity formula (Kearey et al., 2002; Williams, 2008; Pumphrey, 2014):

$$g_{\emptyset} = g_0 (1 + k_1 \sin^2 \emptyset - k_2 \sin^2 2\emptyset) \quad \text{(2.31)}$$

Where $g_{\emptyset}$ is the predicted gravity value at latitude $\emptyset$, g_0 is the gravity value at the equator and k_1, k_2 are constants that are dependent on the shape and speed of rotation of the Earth. An accurate representation of the Gravity Formula 1967 is:

$$g_{\emptyset} = 9\,780\,318.5\,(1 + 0.005278895 \sin^2 \emptyset + 0.000023462 \sin^4 \emptyset)\ \text{gu} \quad \text{(2.32)}$$

The predicted gravity value calculated using the gravity formula at sea level at any point on the Earth's surface ($g_{\emptyset}$)is subtracted from the observed gravity value (g_{obs}) to correct for latitude variations (Kearey et al., 2002; Reynolds, 2011).

Elevation corrections

Elevation corrections are carried out in three stages: the free air correction (FAC), the Bouguer correction (BC), and the terrain correction (TC) (Kearey et al., 2002).

(i) Free Air correction (FAC)

This is used to correct for the decrease in the magnitude of gravity with height in the free air due to increasing distance from the centre of the Earth, irrespective of the nature of the rock below (Kearey et al., 2002; Reynolds, 2011). The FAC is the difference between measured gravity at the datum/sea level and at an elevation of h meters with no rock between (Reynolds, 2011). The accepted value of the FAC is:

$$\mathrm{FAC} = 3.086\mathrm{h\ gu\ (h\ in\ meters)} \quad \text{..... (2.41)}$$

(ii) Bouguer Correction (BC)

Since the FAC does not consider the rock mass existing between the observation point and the datum another correction is required, the Bouguer Correction (BC). The BC calculates the extra gravitational pull exerted by the rock beneath the observation point with a thickness of h meters and mean density ρ (Mg/m^3) (Kearey et al., 2002; Reynolds, 2011).

$$\mathrm{BC} = 2\pi \mathrm{G}\rho\mathrm{h} = 0.4191\rho\mathrm{h\ gu} \quad (2.42)$$

This value is subtracted from the observed gravity value (g_{obs}) for stations above sea level to prevent overestimation of (g_{obs}).

(iii) Terrain Correction (TC)

The Bouguer correction assumes the topography around the gravity station is flat (Kearey et al., 2002; Reynolds, 2011). This is not usually the case hence an additional correction, the terrain correction(TC), must be applied in areas where there are considerable variations in elevation (Kearey et al., 2002; Reynolds, 2011). Terrain effects are minimum in flat-lying areas, normally less than 10 gu hence this correction is normally ignored in such areas (Kearey et al., 2002).

Tidal corrections

Gravity measurements repeated at a fixed location vary over time due to the periodic variation in the gravitational effects of the Sun and Moon linked to their orbital motions (Kearey et al., 2002). Within a minimum of about 12 hours, the Earth's tides cause a change in gravity of up to three gu (Reynolds, 2011). In addition to determining the instrumental drift for a gravimeter, repeated measurements at the same observation point allow for corrections due to tidal effects

over short intervals to be estimated. Tidal effects can be considered part of the instrumental drift (Blakely, 1996).

Free Air Anomaly (FAA) and Bouguer Anomaly (BA)

After applying all the required corrections, the Free Air Anomaly (FAA) and Bouguer Anomaly (BA) are defined as:

$$\mathrm{FAA} = \mathrm{g_{obs}} - \mathrm{g_{\emptyset}} + \mathrm{FAC} \quad \text{(2.5)}$$

and

$$\mathrm{BA} = \mathrm{FAA} - \mathrm{BC} \quad \text{(2.6)}$$

The Bouguer anomaly is the main end-product of gravity data reduction and gives the basis for the interpretation of gravity data on land (Kearey et al., 2002; Reynolds, 2011). The BA should correlate with the lateral variations in density of the near-surface environment (Reynolds, 2011).

3.2.1.2 Gravity data enhancements

Bouguer Anomaly separation

The BA is a sum of high and low-frequency components as indicated by equation 2.7. The Bouguer anomaly consists of gentle varying anomalies with large wavelengths (Kearey et al., 2002; Reynolds, 2011; Mallick et al., 2012; Zakariah et al., 2021). These anomalies are attributed to deep-seated geological features and are known as the regional anomaly ($\mathrm{G_{reg}}$). The BA also contains short wavelengths anomalies referred to as the residual anomaly ($\mathrm{G_{res}}$), caused by shallow, local anomalies that are superimposed in the regional field and are normally isolated for further analysis.

$$G_{BA} = G_{reg} + G_{res} \quad (2.7)$$

Vertical derivative

The vertical derivative filter has been applied to improve the measured gravity field for many years and it is commonly used when the gravity fields of multiple sources interfere (Fedi & Florio, 2001; Tatchum et al., 2011). To determine the location of the source's contacts, it is more accurate to use the vertical derivative of the Bouguer anomaly rather than the Bouguer anomaly itself. This is due, in part, to the vertical derivative's increased ability to isolate the gravity effects of individual sources over the Bouguer anomaly (Tatchum et al., 2011). As a result, the vertical derivative response can be used to identify the signatures of small features that are difficult to identify in the Bouguer anomaly maps. However, this filter can amplify short wavelengths noise caused by poor data processing. This filter employs potential field derivatives to minimize deep seated long wavelength anomalies while enhancing the shallow field components (Ahmed et al., 2018).

3.2.2 Data collection

In this study, a Scintrex™ CG5 gravimeter (figure 3.6), was used to collect gravity measurements. A total of 267 gravity stations were collected along access roads at an average station spacing of 200m (Figure 3.7). The collected gravity measurements were tied to an established gravity station at the centre of the basin. At every gravity station, the elevation data was obtained using the Leica Viva™ Differential Global Positioning System (DGPS). During data collection, the Base station was always set up in a securely fixed station which was almost at the centre of the basin where the gravity base station was established.

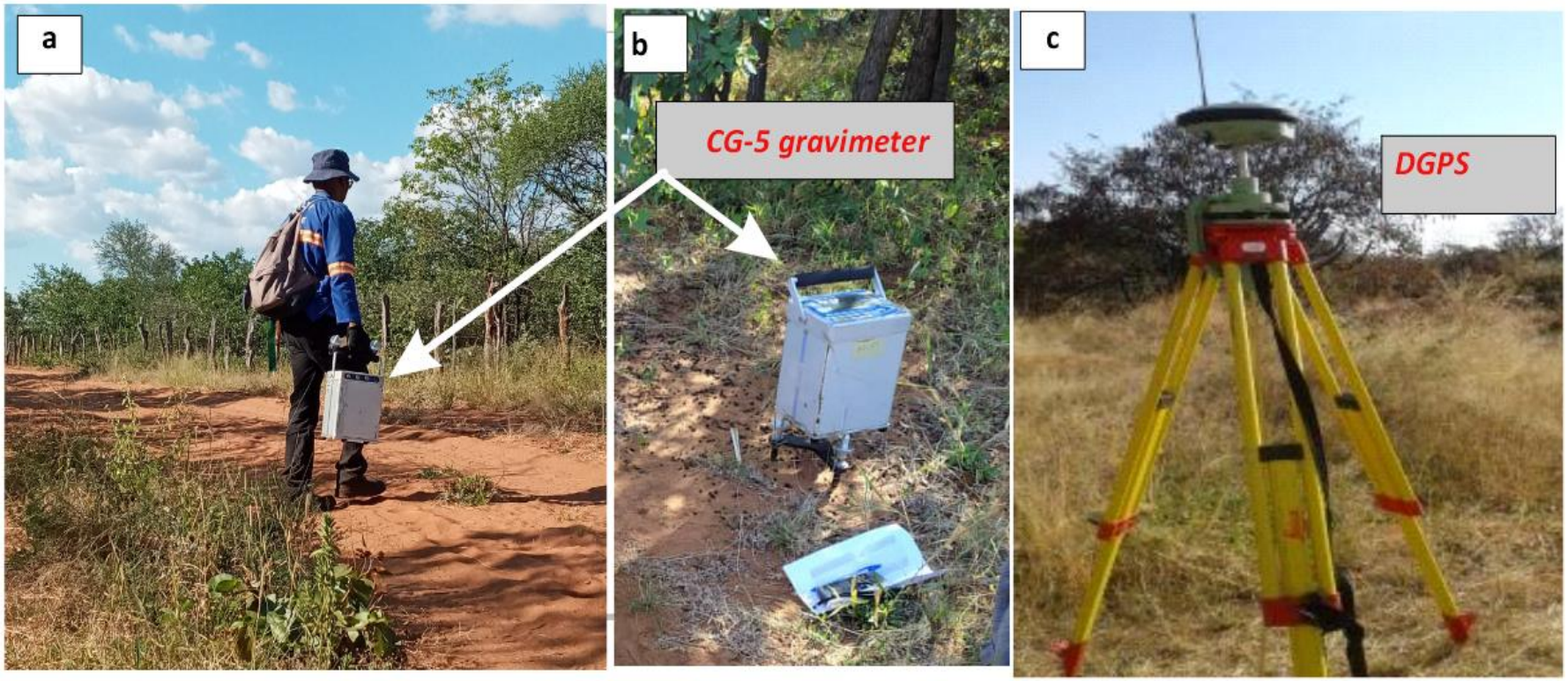

Figure 3.6. Gravity survey fieldwork photos showing the Scintrex™ CG5 gravimeter and the Leica Viva™ DGPS.

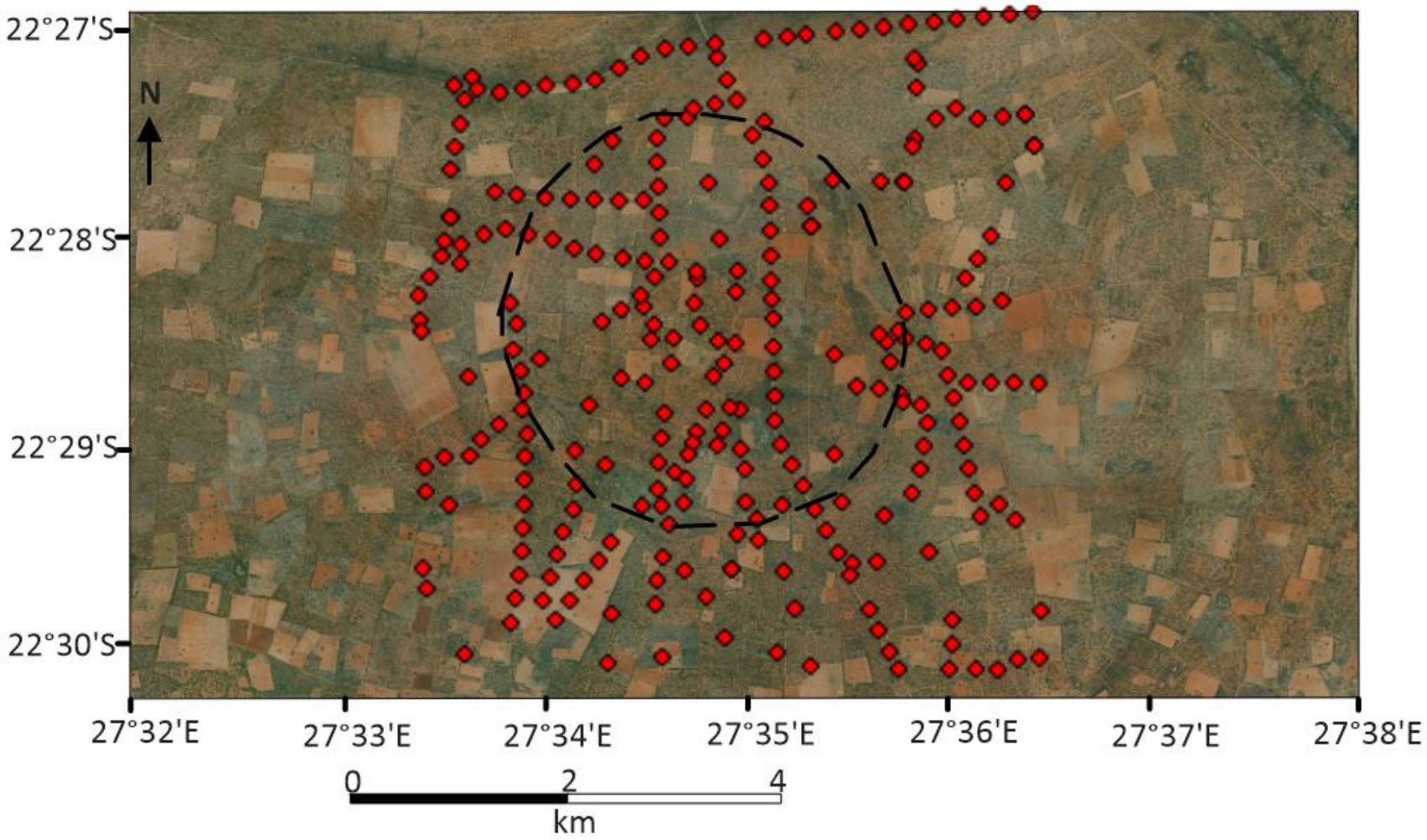

Figure 3.7. Google Earth image showing the location of collected gravity stations/readings. The stations are represented by red dots.

3.2.3 Data processing

Data reduction and processing were done in Oasis Montaj Geosoft™ as illustrated in Figure 3.9. The area around the Kgagodi basin is generally flat (Figure 3.8), therefore the terrain correction was not applied to the data. The Butterworth filter was applied to the Bouguer anomaly to obtain the regional anomaly and the residual anomaly maps. The regional gravity anomaly was obtained by applying low-pass filtering (long wavelengths) which reveals deep-seated structures whereas the residual gravity anomaly is a product of high-pass filtering (short wavelengths) showing the shallow structures. To further enhance the shallow structures in the area, the first-order vertical derivative was also applied to the Bouguer anomaly.

3-D Modelling

The Bouguer anomaly was used to estimate the three-dimensional (3-D) density contrast of the Kgagodi basin. This model was calculated using the GRABLOX version 1.7. This is a gravity interpretation and modelling software that computes the synthetic gravity anomaly of a 3-D block model and can be used for both inverse and forward modelling (Pirttijarvi, 2008). To minimize the difference between the measured and the computed gravity data, the inversion method optimizes either the height of the individual blocks or the density (Pirttijarvi, 2008). The Grablox 1.7 software combines two inversion methods which are processed sequentially; the Singular Value Decomposition (SVD) and the Occam inversion (Pirttijarvi, 2008; Titi & Minarto, 2017; Indragiri, 2019). The Singular Value Decomposition (SVD) is a factorization of a rectangular matrix or square matrix A into orthogonal matrices as described by equation (2.9) (Zhou & Tao, 2011; Ganguli & Dimri, 2013; Indragiri, 2019).

$$A = USV^T \quad \text{.....} \quad (2.9)$$

Where U is the left orthogonal matrix, S is the diagonal matrix, V is the right orthogonal matrix and T is the transpose matrix.

The Occam inversion pursues a smooth model that reasonably satisfies the observational data that is, it minimizes the roughness of the model as well as data misfit (Constable et al., 1987; Li & Yang, 2011; Pirttijarvi, 2008; Indragiri, 2019). Geological interpretation can be done based on the density contrast and overburden layer thickness and variations can be determined (depth to the basement) (Pirttijarvi, 2008).

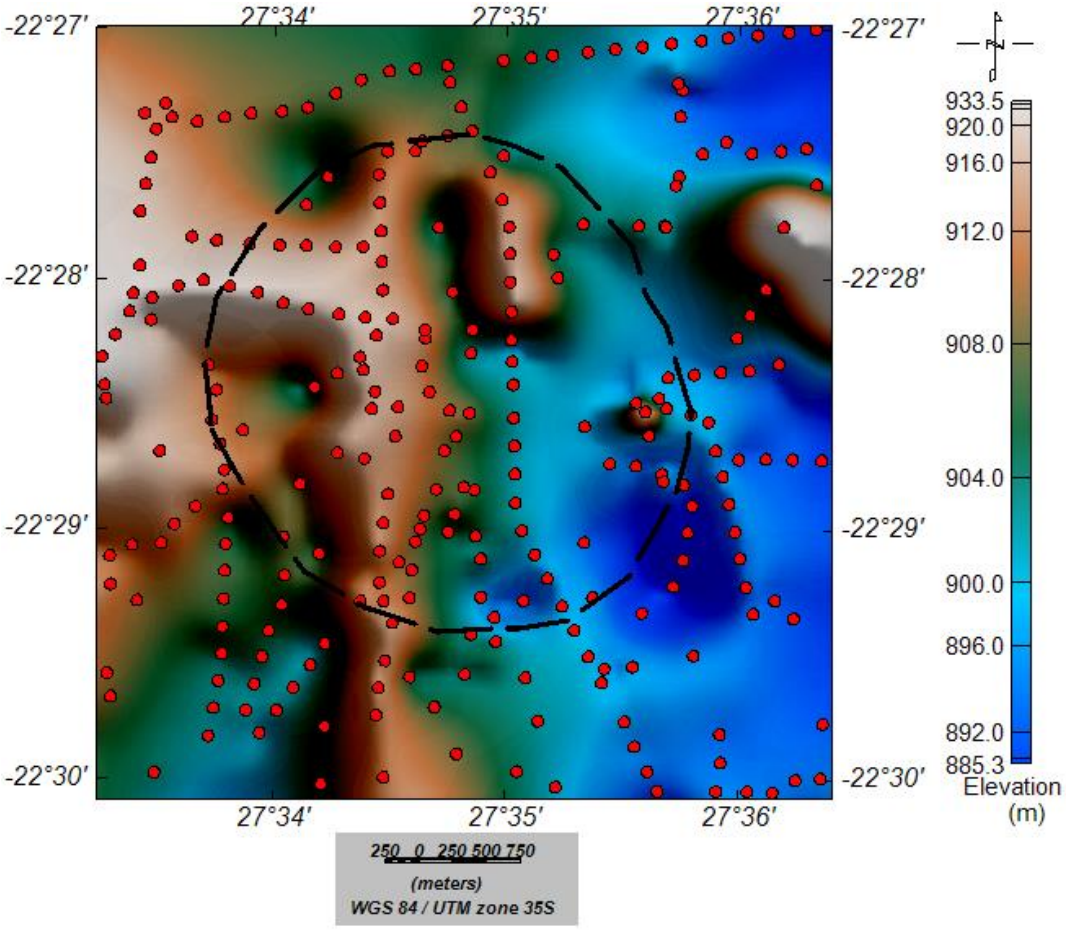

Figure 3.8. Elevation map of Kgagodi basin. Collected gravity stations are shown by red dots.

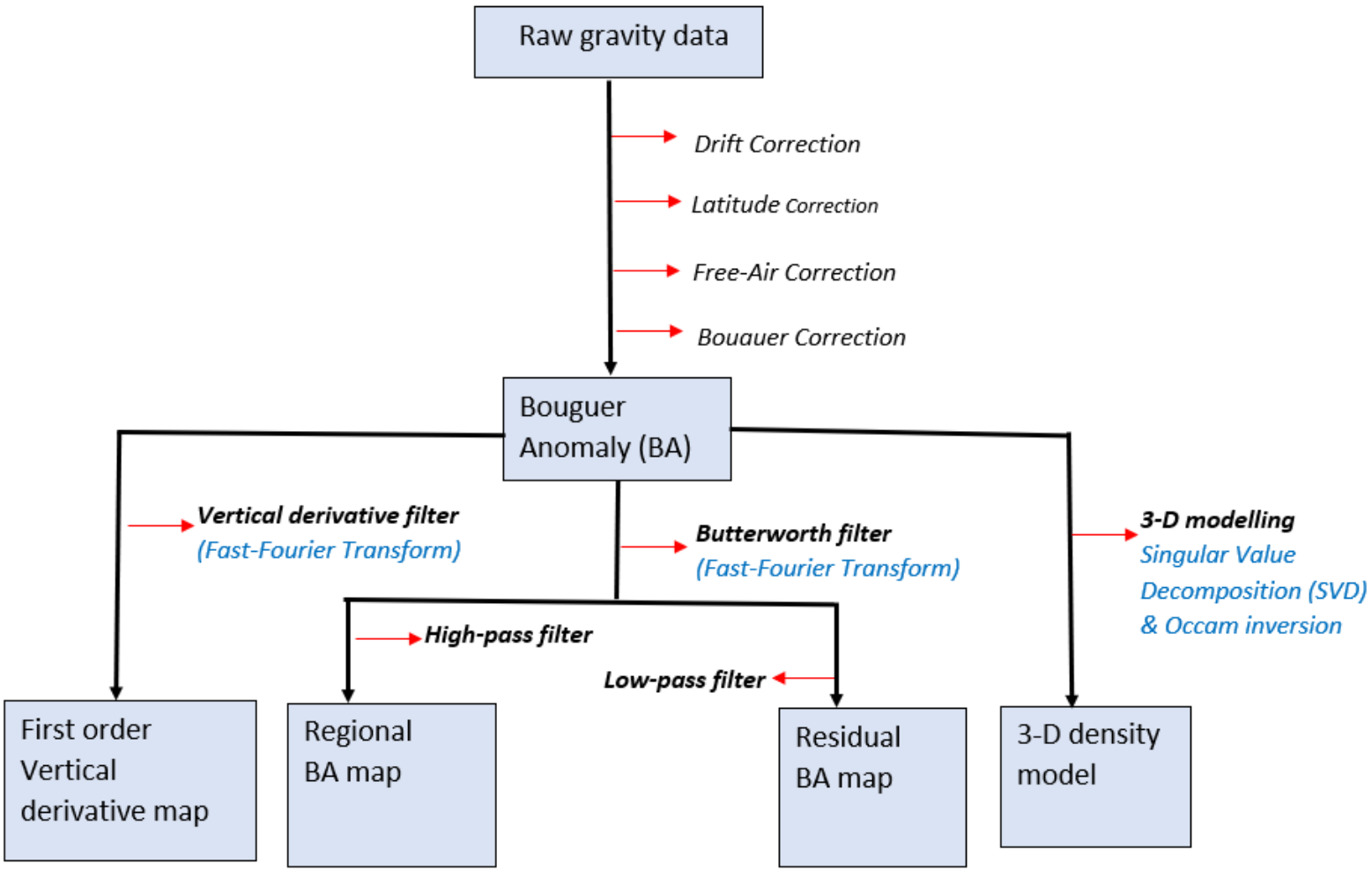

Figure 3.9. A workflow diagram summarizing the gravity data correction and processing. The red horizontal arrows indicate processes/filters involved and black vertical arrows show the end products of processing.

3.3 Vertical Electrical Sounding (VES) method

3.3.1 Theoretical fundamentals of the method

Electrical resistivity is a measure of the difficulty in passing an electric current through a volume of material with a given cross-sectional area and length (Kearey et al., 2002; Loke, 2004). The fundamental physical law used in resistivity surveys is Ohm's Law. This law governs the flow of current in the ground. It states that the electrical current I (measured in Amperes) through a material is directly proportional to the potential difference ΔV (measured in volts), as indicated by Equation 3.1 (Loke, 2004).

$$R = \frac{V}{I} \qquad \text{(3.1)}$$

The resistance in ohms between the opposite faces of a unit cube of material is the resistivity of that material (Kearey et al., 2002). To calculate the resistivity of a conducting cylinder (Figure 3.10) of resistance δR, cross-sectional area δA, and length δL equation 3.2 is used.

$$\rho = \frac{\delta R \delta A}{\delta L} \qquad \text{(3.2)}$$

Electrical methods are the most widely used geophysical methods in both exploration and environmental studies because the subsurface electrical properties can be well correlated to the physical and chemical properties of fluids in pore spaces (e.g. salinity, and saturation) and lithological properties (e.g. clay content and porosity) (Binley, 2015). To pass electric current, geoelectrical methods depend on the conductivity and resistivity properties of the subsurface rock (Haldar, 2018). These methods involve propagating current through a pair of electrodes connected to a transmitter and measuring the resulting potential difference using another pair

of electrodes connected to a voltmeter (Figure 3.11) (Kearey et al., 2002; Binley, 2015; Haldar, 2018).

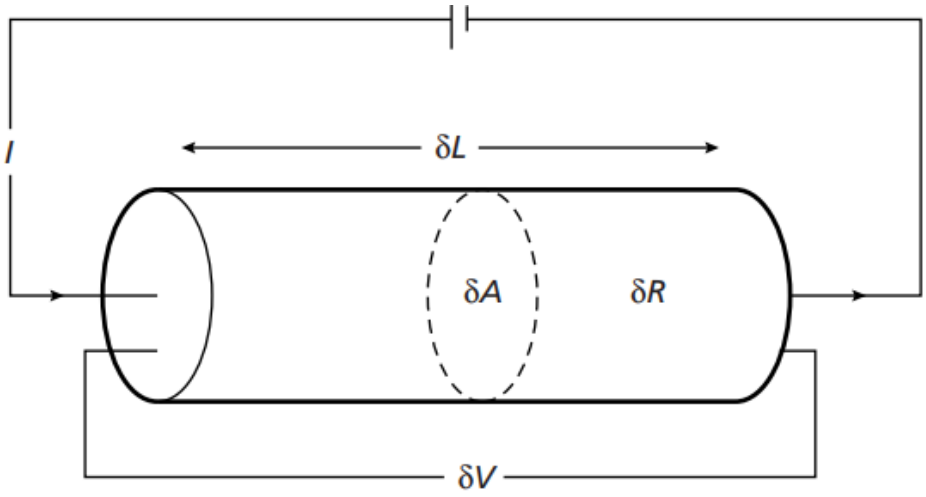

Figure 3.10. Parameters used in defining resistivity (Kearey et al., 2002).

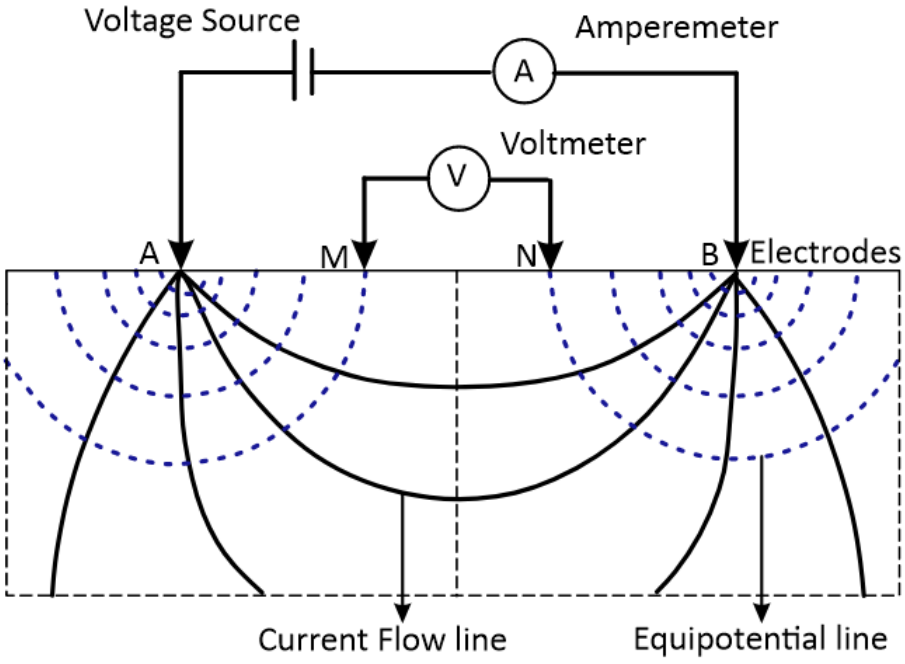

Figure 3.11. Illustration of the basic measurements using the method of electrical resistivity (Modified from Muchingami et al., 2012).

The direct current Vertical Electrical Sounding (VES) method or Electric drilling method uses four electrodes placed along a straight line at the same spacing around a fixed central point to measure the apparent resistivity of the subsurface (Khalil, 2012; Binley, 2015; Haldar, 2018). This method infers the variation of resistivity with depth from a given point on the ground for horizontal or sub-horizontal layers (Haldar, 2018). Two more conditions should be satisfied for VES to provide an accurate geoelectrical structure of the subsurface; the layers should be homogenous in all directions and the terrain should be relatively flat (Karriqi & Alikaj, 2011).

Given a non-uniform subsurface, the resistivity will vary with the relative locations of electrodes. Any calculated value is known as the apparent resistivity, which is a homogeneous earth model that will give the same potential value as the true earth model for the same electrode arrangement and current injected (Kearey et al., 2002). The apparent resistivity ρ_a, of a subsurface material (equation 3.3) is a function of the current magnitude, recorded potential difference, and the geometry of the electrode configuration used (Binley, 2015; Selvakumar et al., 2015).

$$\rho_a = \frac{k\Delta V}{I} \quad \text{.....} \quad (3.3)$$

Where k is the geometric factor expressed as:

$$k = \frac{2\pi}{\frac{1}{AM} - \frac{1}{BM} - \frac{1}{AN} + \frac{1}{BN}} \quad \text{.....} \quad (3.4)$$

The commonly used electrode arrays are Schlumberger, Wenner, and dipole-dipole which are shown in Figure 3.12 (Reynolds, 2011; Haldar, 2018).

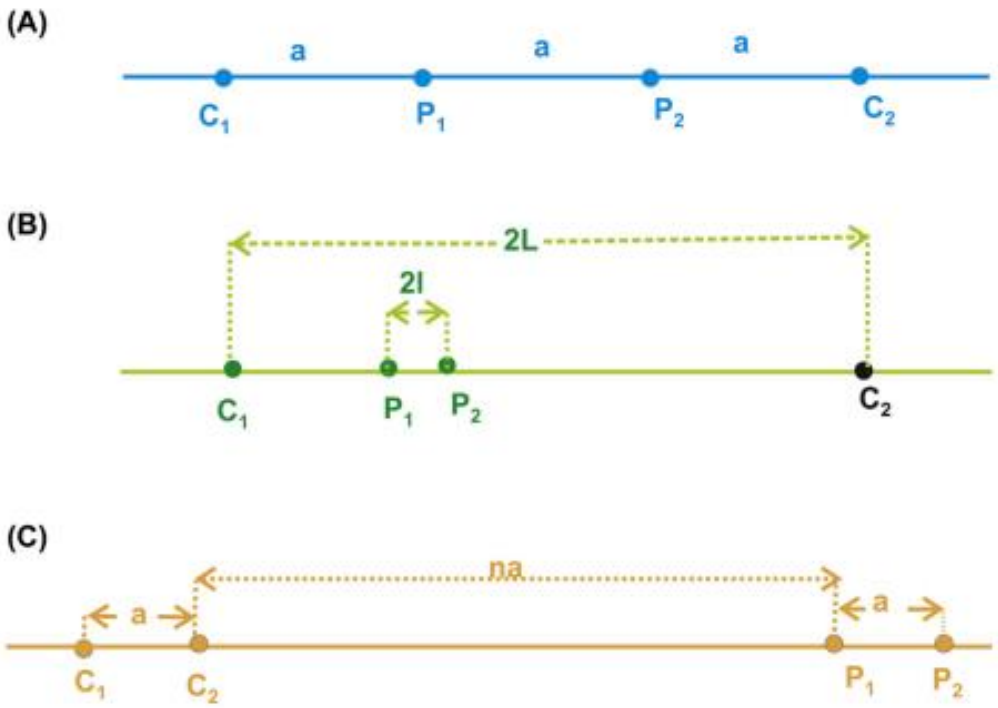

Figure 3.12. Schematic diagram of common electrode configuration types used in resistivity surveying: (A) Wenner configuration, (B) Schlumberger configuration, and (C) dipole/dipole configuration .C_1 and C_2 are current electrodes, P_1 and P_2 are the potential electrodes (Haldar, 2018).

Wenner electrode configuration: When using this electrode arrangement, all four electrodes are kept along at an equal electrode spacing *a,* and are all moved between successive readings (Kearey et al., 2002; Binley, 2015).

Schlumberger electrode configuration: In this configuration, the current electrodes C_1 and C_2 remain outside the potential electrodes P_1 and P_2 (Reynolds, 2011; Binley, 2015). The distance between P_1 and P_2 is much smaller than the distance between C_1 and C_2 (i.e., P_1 and P_2 distance < 0.2 x C_1 and C_2 distance). To account for the gradually decreasing potential gradient with increasing current electrode spacing which causes the measured voltage between P_1 and P_2 to

fall to very low values, the spacing between the potential electrodes is increased (Reynolds, 2011).

Dipole-Dipole electrode configuration: With this electrode configuration P_1 and P_2, remain outside C_1 and C_2. Each pair of electrodes has a constant spacing of *a*. If the distance between the two pairs of electrodes *na* is big, the current source is treated as an electric dipole (Haldar, 2018).

It is a typical rule of thumb in the VES techniques that the depth of investigation should be on the order of 0.1 to 0.3 times the C_1-C_2 length (Bernard, 2003). For example, a 500m C_1-C_2 line gives a depth of 50m to 150m depending on the layering type. A resistive basement has a long C_1-C_2 line than a conductive basement; however, the signal in the first case is usually higher than in the second one.

Table 3.2. Comparison of common electrode arrays for electrical resistivity measurements (Binley, 2015).

	Schlumberger configuration	Dipole-Dipole Configuration	Wenner configuration
Depth of investigation	Medium	High	Low
Vertical resolution	Medium	Low	High
Signal strength	Medium	Low	High
Suitability for Vertical sounding	High	Low	Medium
Suitability for lateral profiling	Low	High	Medium

The resistivity values of different rocks, soil materials, and water are indicated in Figure 3.13. The electrical resistivity of a particular soil or rock sample depends on some factors e.g. porosity, the degree of water saturation, and dissolved salts concentration (Kearey et al., 2002; Loke, 2004). Nonetheless, porosity is the major determinant of rock resistivities; resistivity generally increases with decreasing porosity (Kearey et al., 2002).

Metamorphic and igneous rocks typically have high resistivity values ranging from about 1000 to 10 million Ω.m, depending on the degree of fracturing and water-filled fractures (Loke, 2004). Sedimentary rocks have lower resistivities as compared to crystalline rocks because of the increased porosity and water content. Their resistivities range from 10 to 10000 Ω.m and they are dependent on the porosity and the salinity of the water in the pores. Resistivity values of unconsolidated sediments are generally lower than those of sedimentary rocks, ranging from about 10 to less than 1000 Ω.m. Their resistivities are dependent on the porosity and the clay content. High clay content results in lower resistivity values (Loke, 2004; Loke, 2013). The concentration of dissolved salts in groundwater determines its resistivities which typically range from 10 to 100 Ω.m.

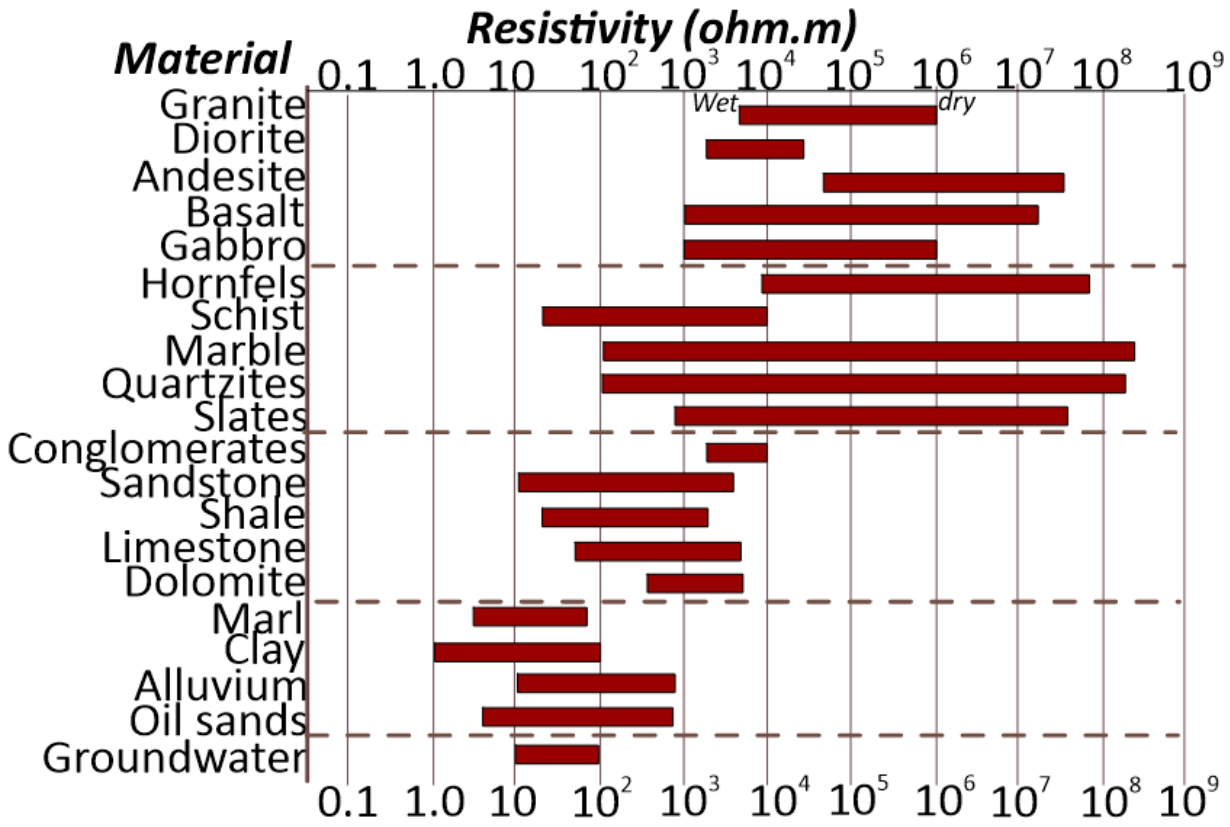

Figure 3.13. Resistivity values for different earth materials (Loke, 2013).

Classifying the shape of the sounding curve obtained is the first step in any interpretation of apparent resistivity sounding data (Reynolds, 2011). The curves can be classified into one of the four basic curve shapes for a three-layer resistivity medium (Figure 3.14 A-D). In a multiple layer setup, more complex curves are obtained therefore the 3-layer curves can be used in conjunction (e.g., Figure 3.14 E-F).

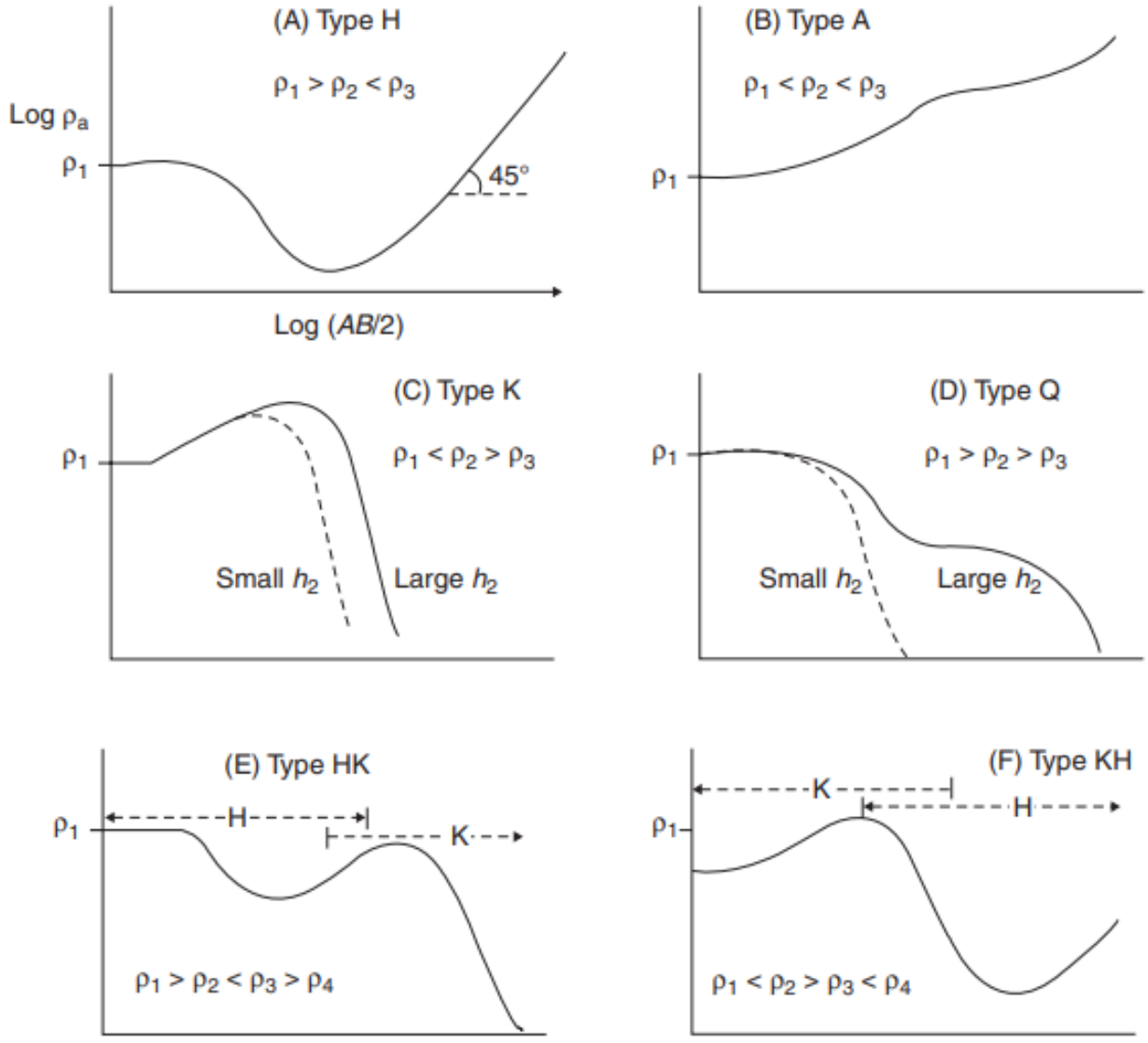

Figure 3.14. Shapes of apparent resistivity curves for various resistivity structures. A-D show curves for a 3-layer resistivity model and E-F indicate curves for a 4-layer resistivity structure (Reynolds, 2011).

3.3.2 Data collection

The IRIS Syscal Pro resistivity/IP unit (Figure 3.15) was used in this study to collect resistivity data. This is a multi-electrode, and multi-channel equipment containing the transmitter, receiver, and booster. This unit computes and displays apparent resistivity for different electrode

configurations. To attain high signal-to-noise ratios, high resolution of vertical layers, and good sensitivity, the Schlumberger array configuration was employed (Binley, 2015; Mankhemthong et al., 2020). This electrode array is widely used in VES surveys because the fixed potential electrode dipoles make surveys be to be completed faster and efficiently, with less manpower required since only one of the dipoles is moved for each measurement (Binley, 2015).

Using the general expression for the geometric factor (equation 3.4), the apparent resistivity ρ_a for this configuration is expressed as:

$$\rho_a = \frac{\pi\,(s^2 - a^2)}{4a}\,\frac{\Delta V}{I} \quad \text{.....} \quad (3.5)$$

Where s and a are the distances between AB and MN respectively, I is current, and V is voltage

Resistivity measurements were collected over 25 stations with an average station spacing of 1000m across the basin (Figure 3.16). Due to the limited accessibility in the survey area, the current electrode spacing (AB) ranges from 3.6 to 500 m (AB/2 = 1.8 m to 250 m). The distance used for potential electrode spacing (MN) ranged from 2 m to 80 m (MN/2 = 1m to 40 m). To reduce the ground resistance both current and potential electrodes were hit as deeply as possible into the ground. In very dry and hard areas the contact resistance between the ground and the electrodes was reduced by moistening the ground around all electrodes with saline water. To improve the data quality, only resistance of less than 10 Kohm was allowed and a standard deviation of less than 5% was set. The data was generally acquired by moving two or four of the electrodes used, between each measurement.

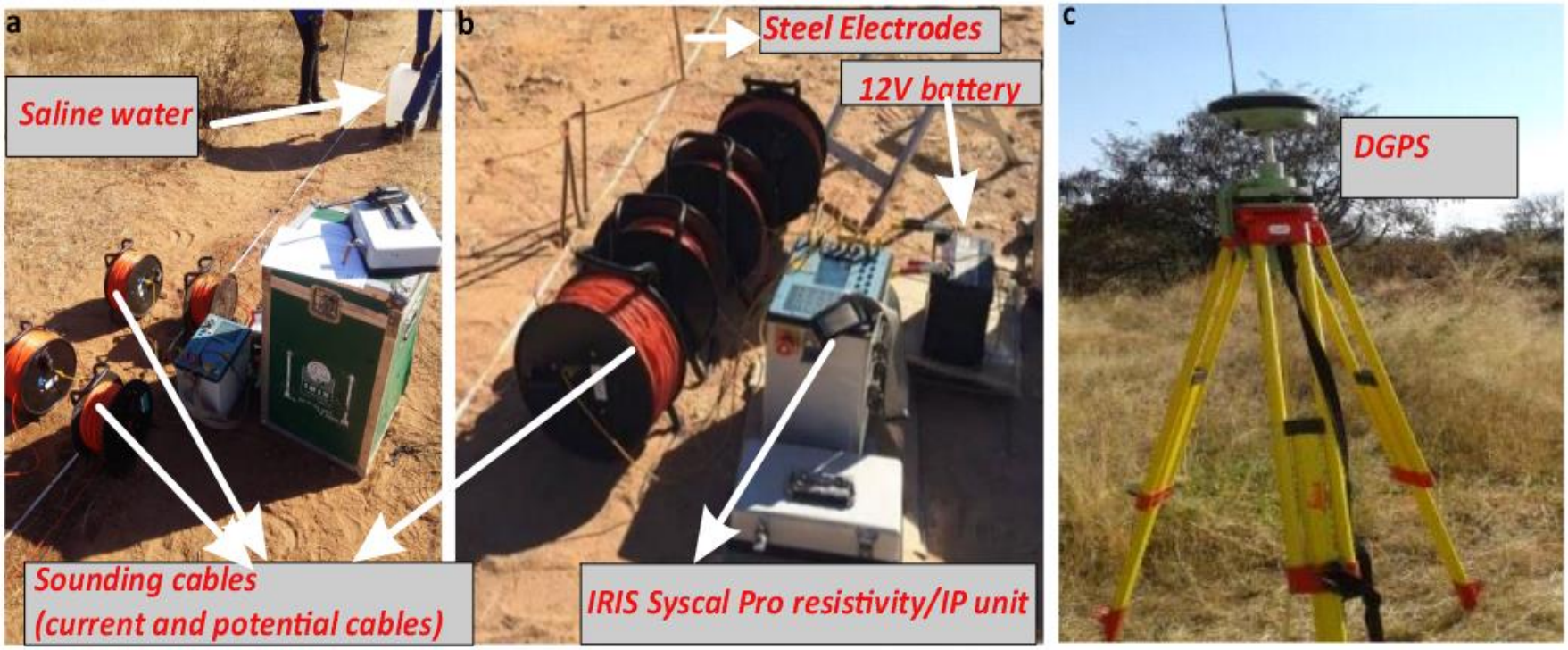

Figure 3.15. Fieldwork photos showing some of the materials and equipment used for VES data collection.

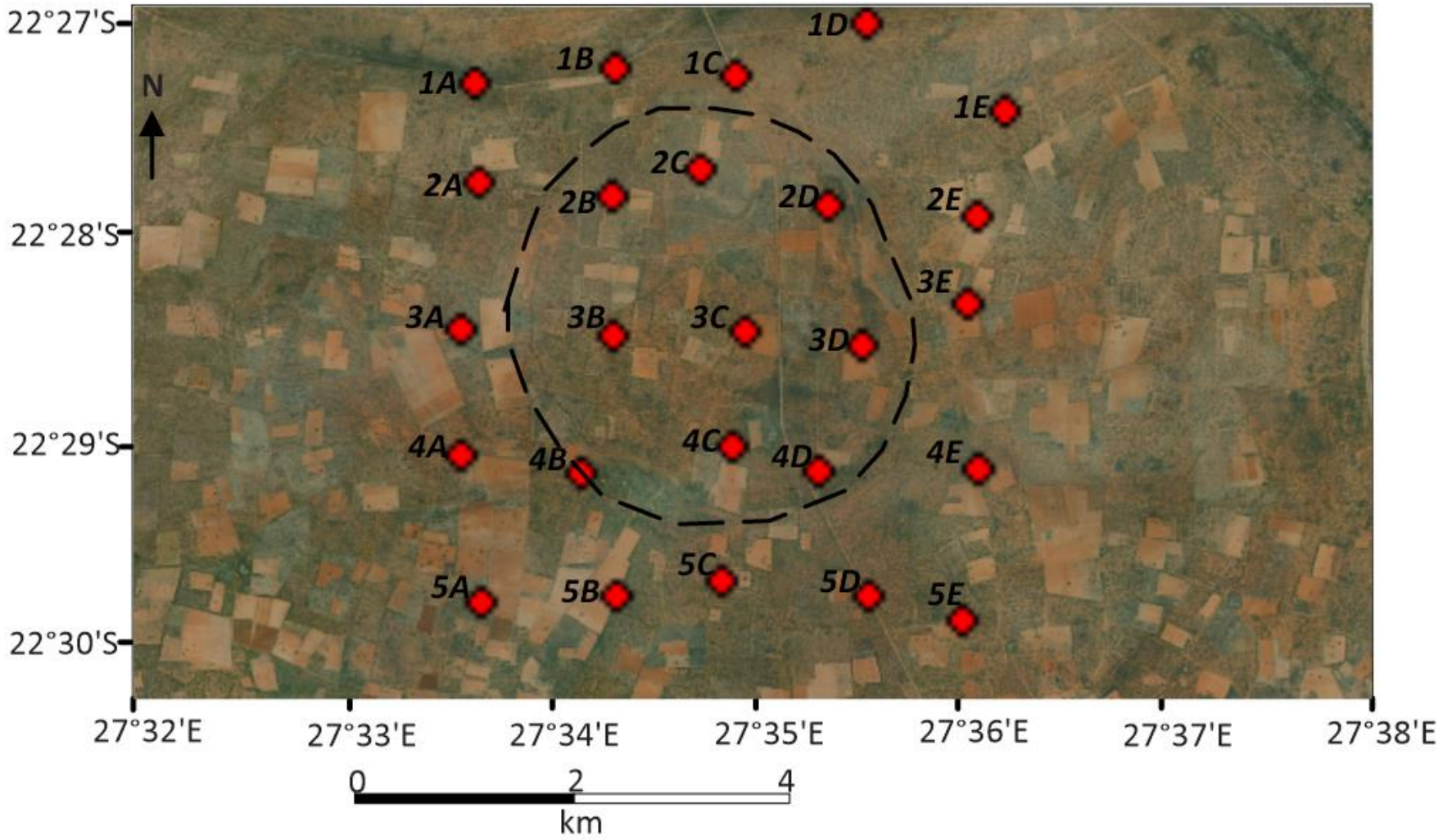

Figure 3.16. Google earth image showing VES locations in the study area. The stations are represented by red dots.

3.3.3 Data processing

Raw field data was open in Prosys II to remove spurious data points from the dataset and to ensure that only good quality data is used in processing. The raw data file was saved as a *.dat file and imported into Interpex's IXID V3*TM* software. This is an interactive, graphically oriented program used for interpreting and recovering VES data in terms of a layered (1-D) model (a series of layer thicknesses and associated resistivity) that is consistent with the measured response for each VES (Binley, 2015). Iterations were carried out to reach the best fit between the calculated curve and the smoothed field curve for estimating a 1-D lithological model of the subsurface. The maximum Root Mean Square (RMS) error allowed was 5%.

The qualitative interpretation was done by visual inspection of the shape of the sounding curves produced to characterize them according to their resistivity signatures, to show the distribution of the curves across the study area, and to assess the number of resistivity layers, whereas, in the quantitative interpretation, the true resistivity and layer thickness of geoelectrical units were obtained (Selvakumar et al., 2015; Ibraheem & El-Qady, 2017). Iso-apparent resistivity maps were generated using apparent resistivity values in the commercially available Surfer™ software. These maps give an idea about the electrical structure of an area by showing the lateral variations in the measured apparent resistivity at the same current electrode spacing (El-Sayed et al., 2021). The maps provide information on the homogeneity and heterogeneity of apparent resistivity values in different locations at almost the same depth (Reynolds, 2011; El-Sayed et al., 2021). 2-D geoelectrical sections were also generated in Surfer™ software.

Chapter 4

Results and interpretation

4.1 Aeromagnetic method

The TMI map of the Kgagodi basin and the surrounding environment (Figure 4.1), reveals a distinctive smooth magnetic texture over the basin which is likely attributed to basin-fill mainly made up of post-impact material like sediments. Surrounding this signature is a noisy, complex magnetic signature representing the surrounding metamorphic basement terrain. This map highlights a prominent lineament that is oriented NW-SE with a high magnetic intensity of up to 1099 nT, cutting through the study area. This lineament, presumed to be a dyke, seems to be discontinuous at the edges of the basin.

The analytic signal and the greyscale vertical derivative (Figure 4.2a and 4.2d) show a change in magnetic signature on the north-eastern side of the basin, possibly attributed to faulting. In addition, a low magnetic signature anomaly trending NE-SW, possibly a fault is revealed in the tilt angle map and the reduced to pole map (Figure 4.2a and 4.2c).

The results of the tilt angle depth (figure 4.3) and those from the standard Euler deconvolution algorithm (Figure 4.4) correlate. The two depth estimate techniques picked the same magnetic bodies in the study area corresponding to those observed in Figure 4.2. The maximum estimated depth to the top of the magnetic source in the area is 500m. Magnetic bodies within the basin generally have depths ranging from 100-300 m and those outside the basin have depths less than 100m. It is observed that the lineament previously interpreted as a dyke trending NW-SE has an estimated depth of about 100m.

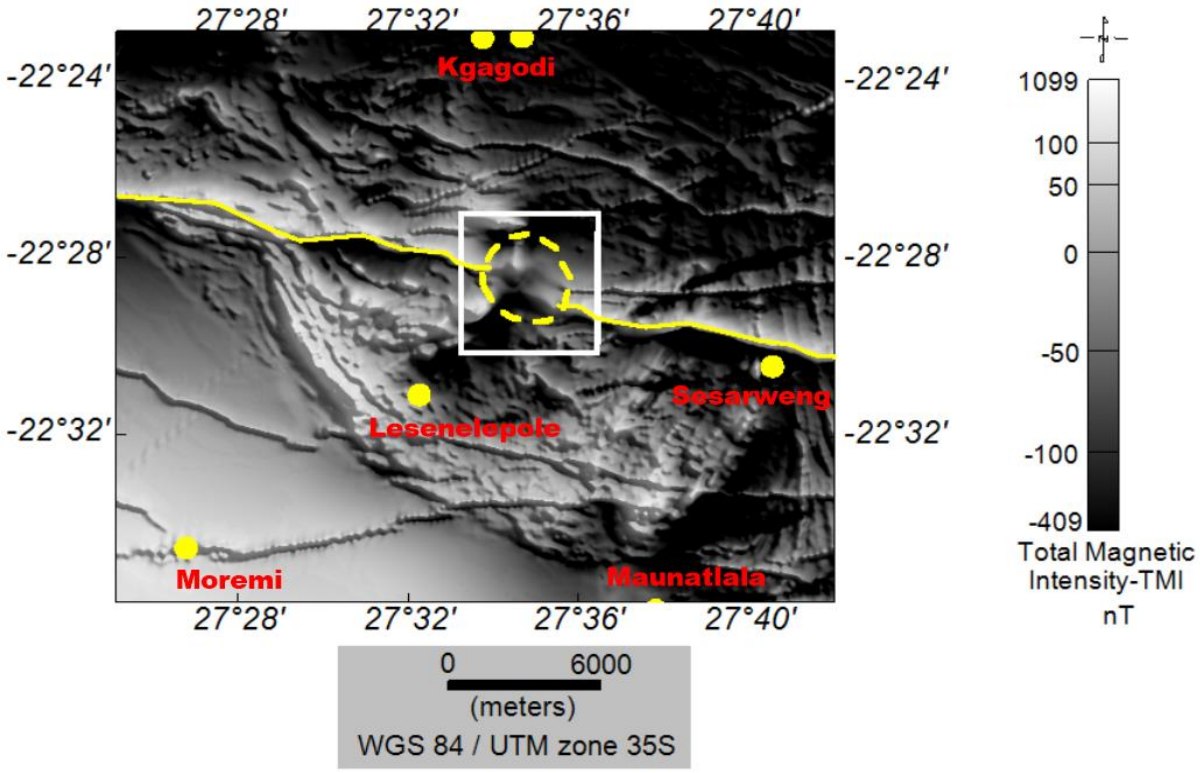

Figure 4.1. The greyscale Total Magnetic Intensity (TMI) map of the area around the Kgagodi basin. The white box is the section windowed for further magnetic analysis. The yellow dashed circle and the solid line represent the Kgagodi basin boundary from the satellite image and the NW-SE lineament respectively. The yellow dots are the settlements/villages around the study area.

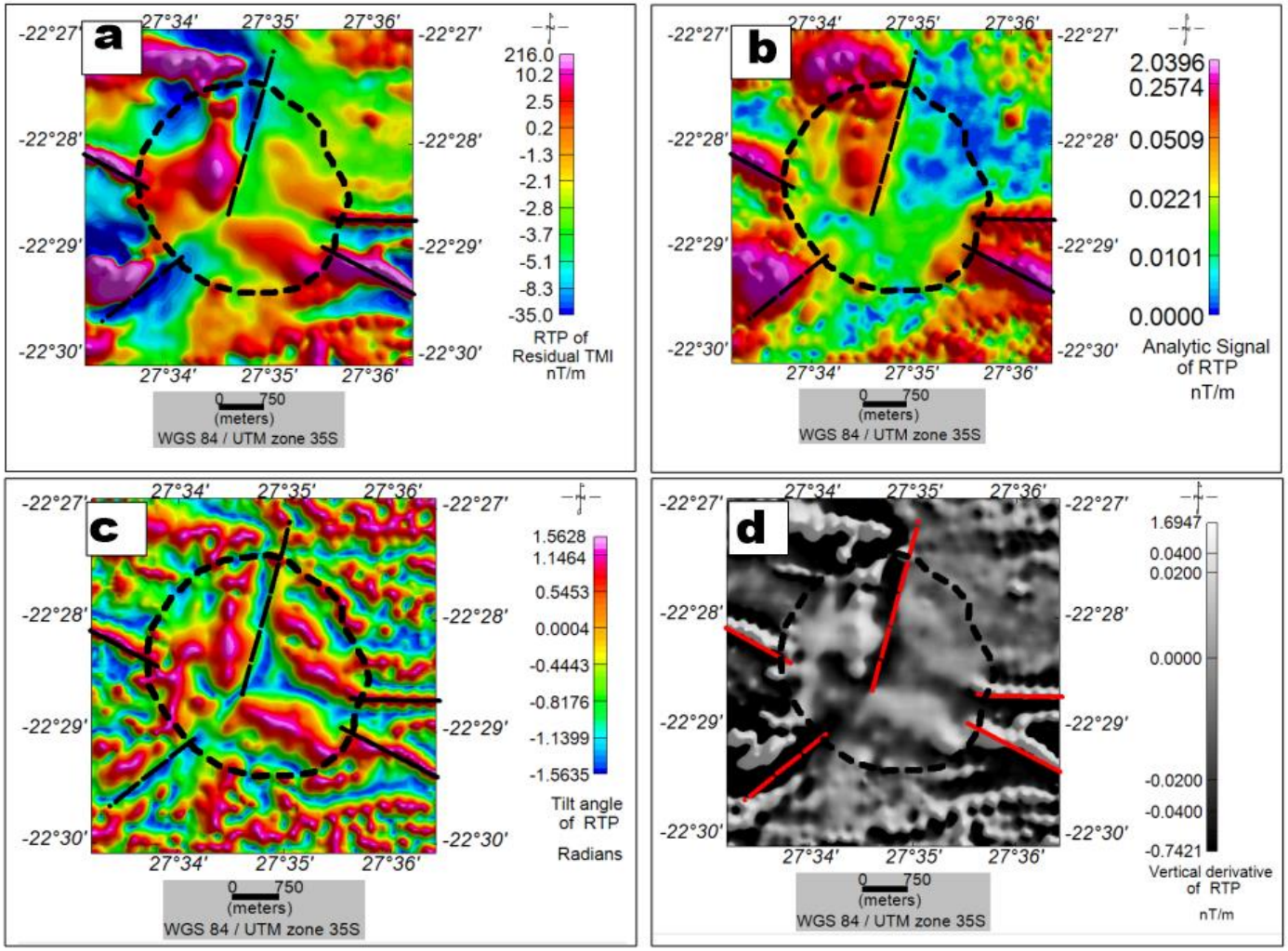

Figure 4.2. windowed maps(a) Reduced to Pole map, (b) Analytic Signal map, (c) Tilt angle map, and (d) the first order vertical derivative. Dashed lines represent a possible fault and solid lines represent the dykes. The circle represents the Kgagodi basin boundary from the satellite image.

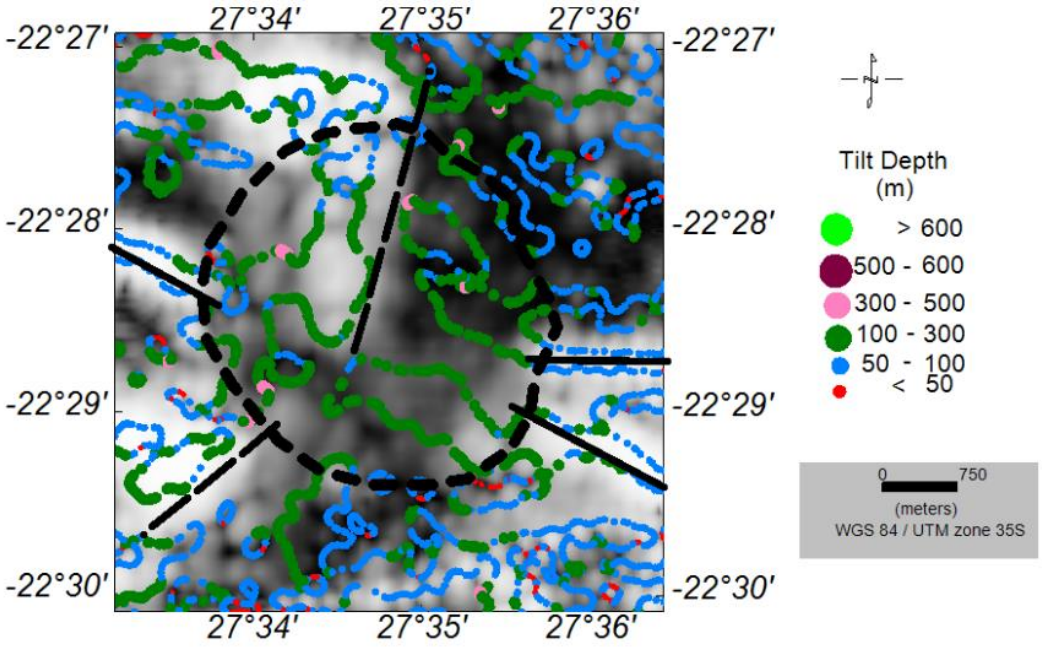

Figure 4.3. Tilt depth estimates are overlain on the greyscale analytic signal map. The bright areas are the high magnetic anomalies, and the dark areas are the low magnetic anomalies.

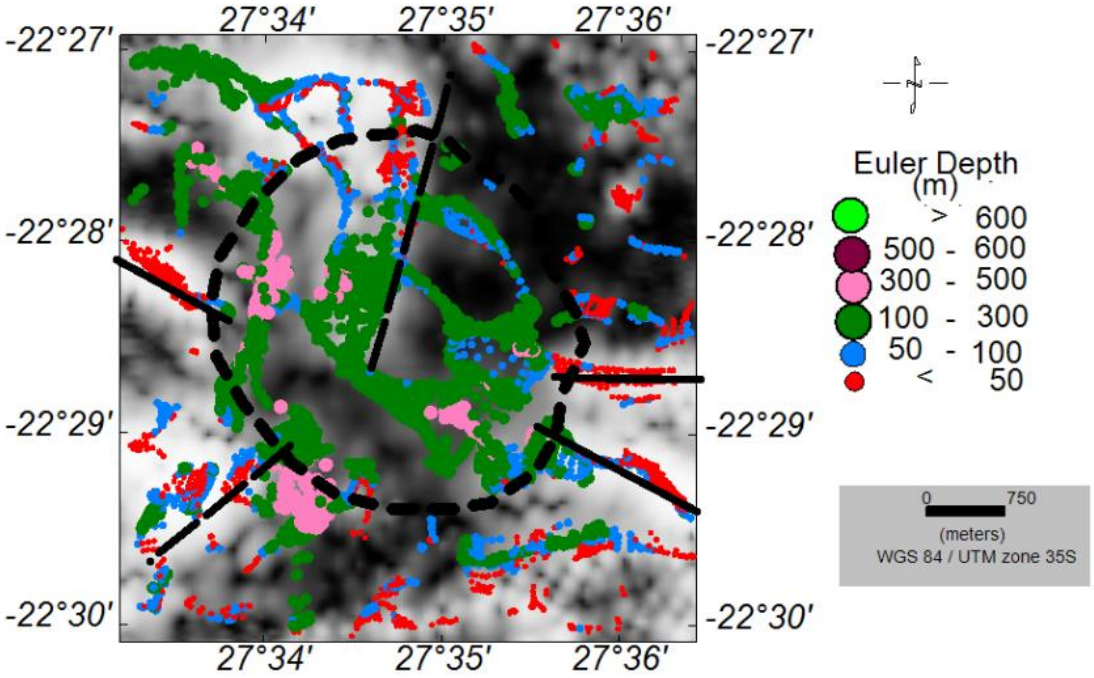

Figure 4.4. Euler deconvolution depth estimates are overlain on the greyscale analytic signal map. The bright areas are the high magnetic anomalies, and the dark areas are the low magnetic anomalies.

4.2 Gravity method

Results of the gravity data reveal the heterogeneous nature of the Kgagodi basin with the surrounding environment (Figure 4.5). Two main signatures were observed in the Bouguer Anomaly (BA) map (Figure 4.5a): a pronounced density low (-127.8 to – 119.4 mGal) over the basin which is associated with the basin fill and high densities (-119.5 to -112.2 mGal) representing the metamorphic basement terrain. The residual Bouguer anomaly map (Figure 4.5b) shows densities of up to 4.3 mGal in the Kgagodi basin and the surrounding environment. The central gravity low anomaly has densities ranging from -4.8 to -0.5 mGal. Anomalies observed in the residual Bouguer anomaly map correspond to those observed in the vertical derivative of the Bouguer anomaly map (Figure 4.5d). The gravity signature in the area is mostly controlled by the regional anomalies as indicated by Figure 4.5c which is similar to the BA map.

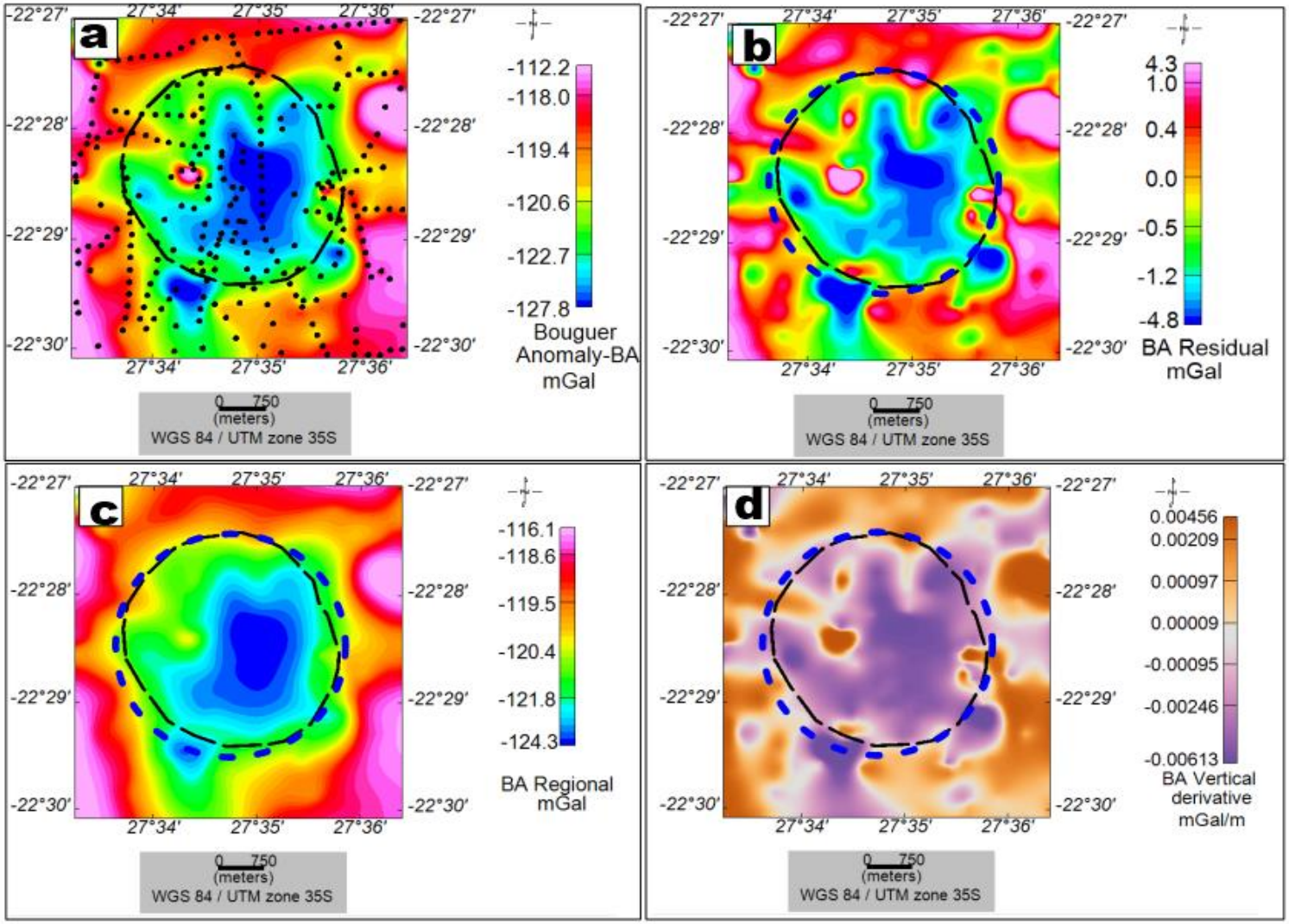

Figure 4.5. (a) Bouguer anomaly map overlain with collected gravity stations (shown by black dots), (b)Residual Bouguer anomaly, (c) Regional Bouguer anomaly, and (d) Vertical derivative of the Bouguer anomaly. The inner black dotted outline is the topographic expression of the basin from the satellite image, and the blue dotted outline is the basin outline derived from the gravity results of this study.

Depth slices obtained from the 3-D model (Figure 4.6) show a density contrast of 1.75 to 2.6 g/cm^3 from 0-969m which can be associated with the basin fill. From 970-2910 m, low densities ranging from 1.25 to 2.5 g/cm^3 can be observed at the centre of the structure. This may indicate highly fractured, brecciated, and possibly melted target material. The area covered by this signature reduces as depth increases. At a depth of 2910 m, a signature of 2.5 g/cm^3 can be observed at the centre of the structure. From 3300m only high densities of ~3.0 g/cm^3 most likely representing the undeformed basement can be observed across the structure.

From the 3-D vertical slices obtained, slices for profile C, profile D (Figure 4.7), and profile D (Figure 4.8) cut through the center of the basin and give a clear image of the density distribution/contrast within this structure. The interpretation of the density model (vertical slices) therefore mainly refers to these slices. The densities obtained indicate a bowl-shaped structure. These densities can be categorized into 3; (1) A 970m thick medium-density layer ranging between 2.0-2.75 g/cm^3 at the top of the model. This layer is proposed to be the crater fill possibly made up of allochthonous material. The above suggests that the apparent crater depth is approximately 700-900m deep (2) A parabolic lens of low densities of 1-1.9 g/cm^3 can be proposed to be the breccia lens made up of both allochthonous material and highly shocked and melted target material. This material extends to depths of approximately 2700m at the center of the crater and is confined to a high-density layer (2-3 g/cm^3). The 2700m depth, might represent the true crater depth. (3) The bottom section with high densities of 2-3 g/cm^3 can be suggested to represent the parautochthonous material or undeformed layer.

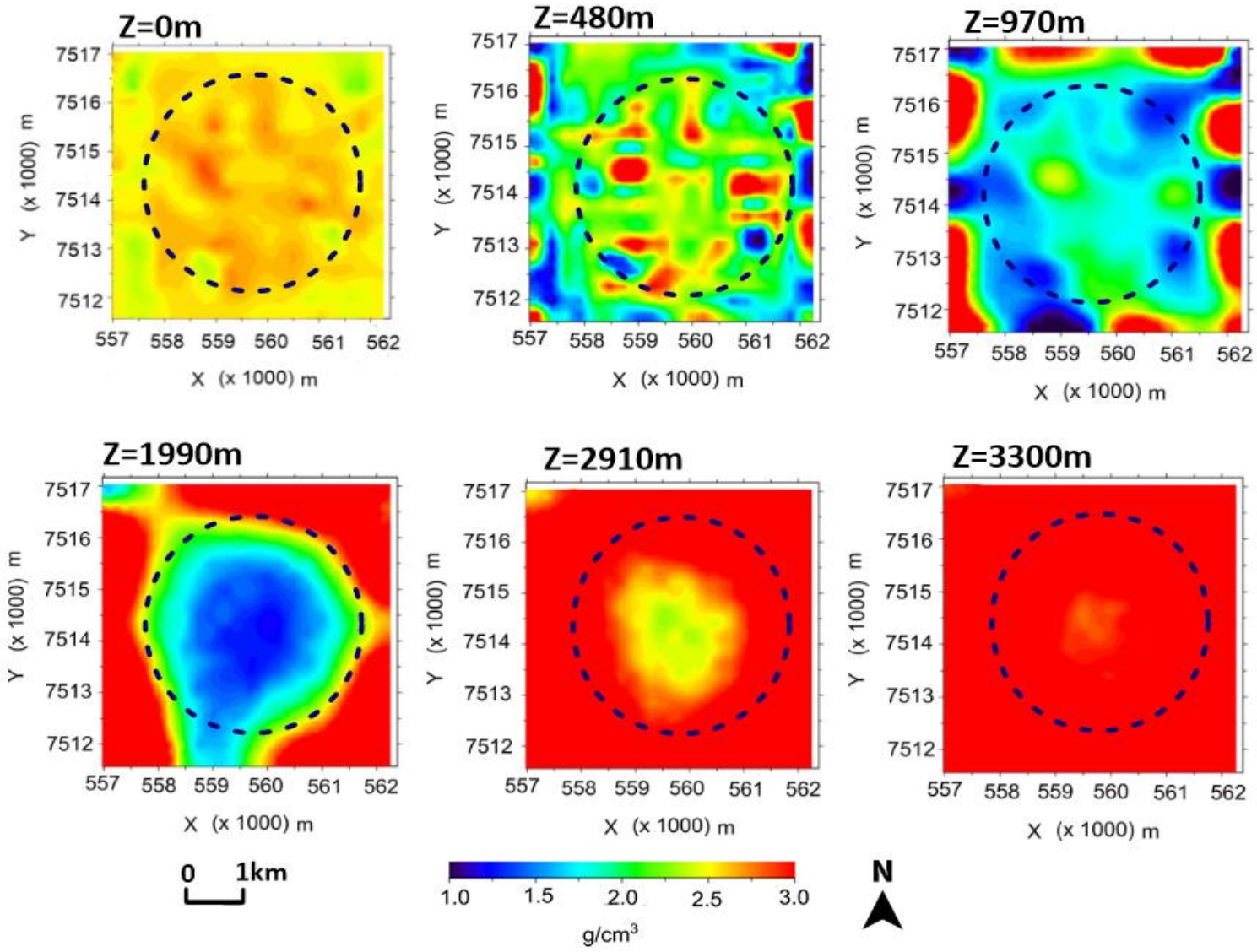

Figure 4.6. 3-D density model horizontal slices showing the variation of density distribution with depth, from the surface to the basement. The blue dotted outline is the basin outline derived from gravity results.

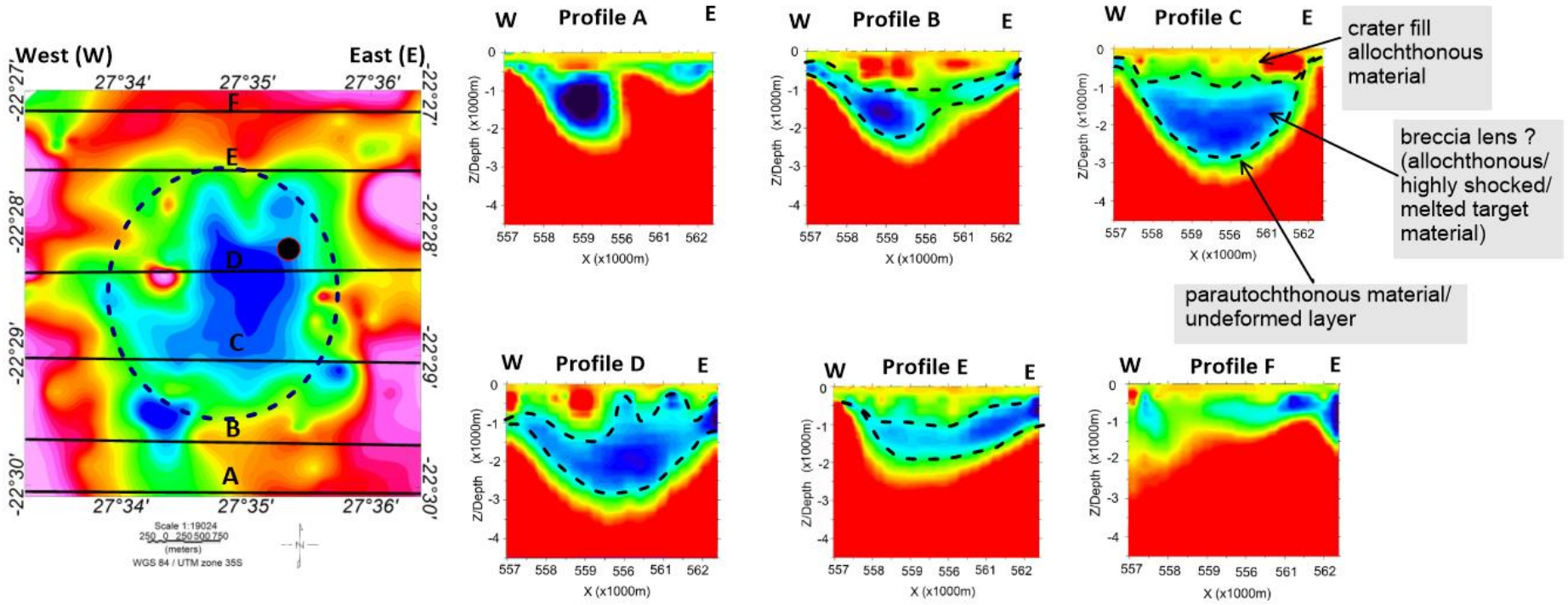

Figure 4.7. 3-D density model vertical slices showing density distribution in the West-East direction with depth. The black dot is the location of the borehole in the Kgagodi basin from Brandt et al. (2002).

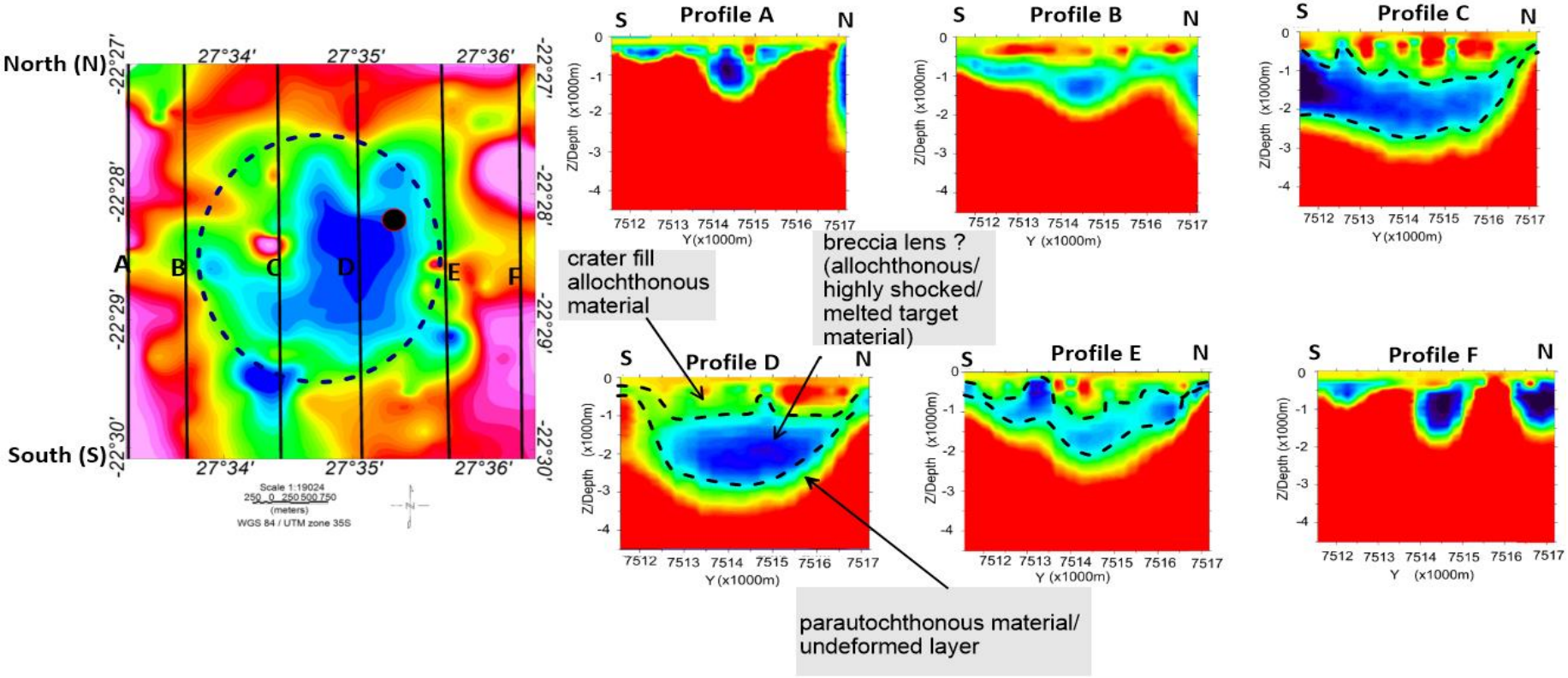

Figure 4.8. 3-D density model vertical slices showing density distribution in the South-North direction with depth. The black dot is the location of the borehole in the Kgagodi basin from Brandt et al. (2002).

4.3 Vertical Electrical Sounding method

From the 25 vertical electrical soundings carried out the following field curves were obtained from 1-D modeling of the data: H, K, and Q curves indicating a 3-layer geo-electrical surface (Figure 4.9). The AA, HA, HK, KH, KQ, and QH, reveal a 4-layer geo-electrical surface (Figure 4.10). The HKH, QHA, and QQH indicate a 5-layer geo-electrical surface (Figure 4.11).

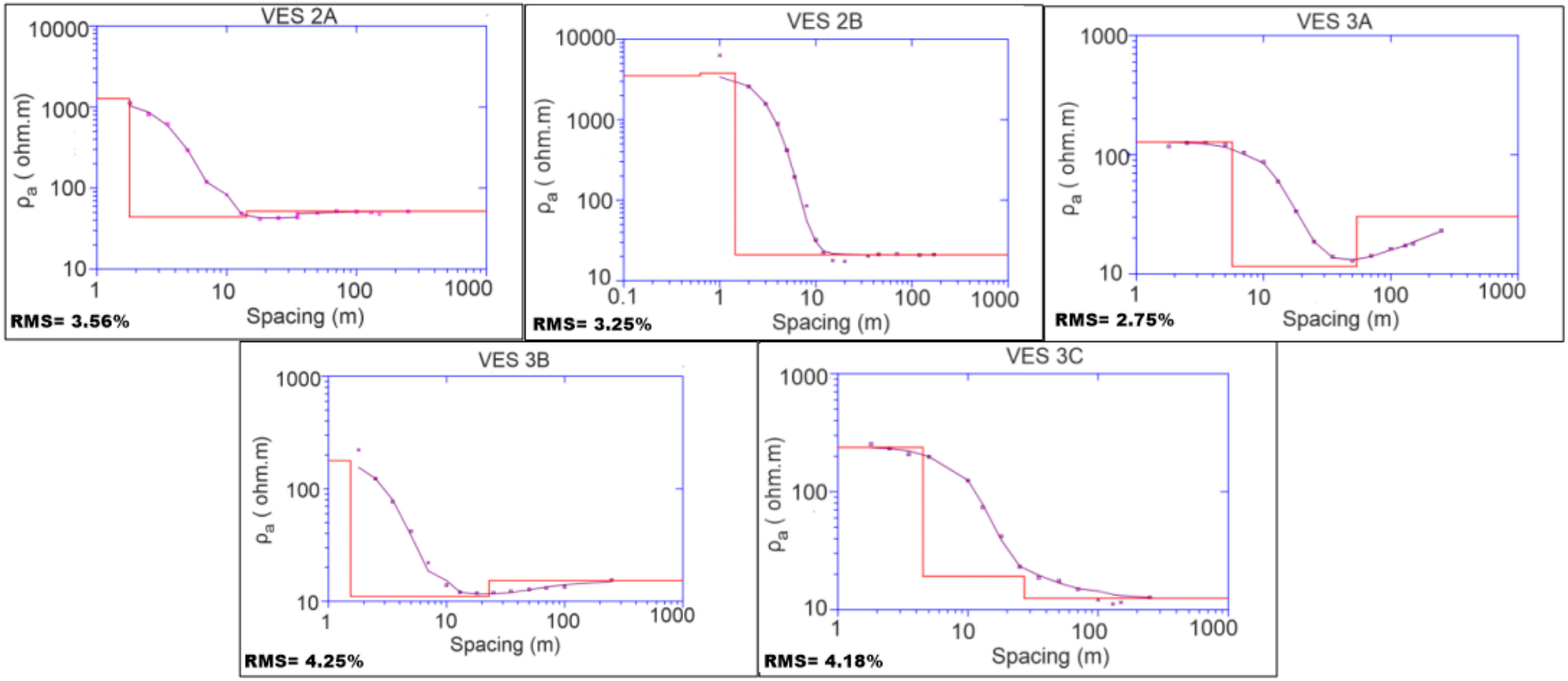

Figure 4.9. VES 3-layer models, showing the H, K, and Q field curves.

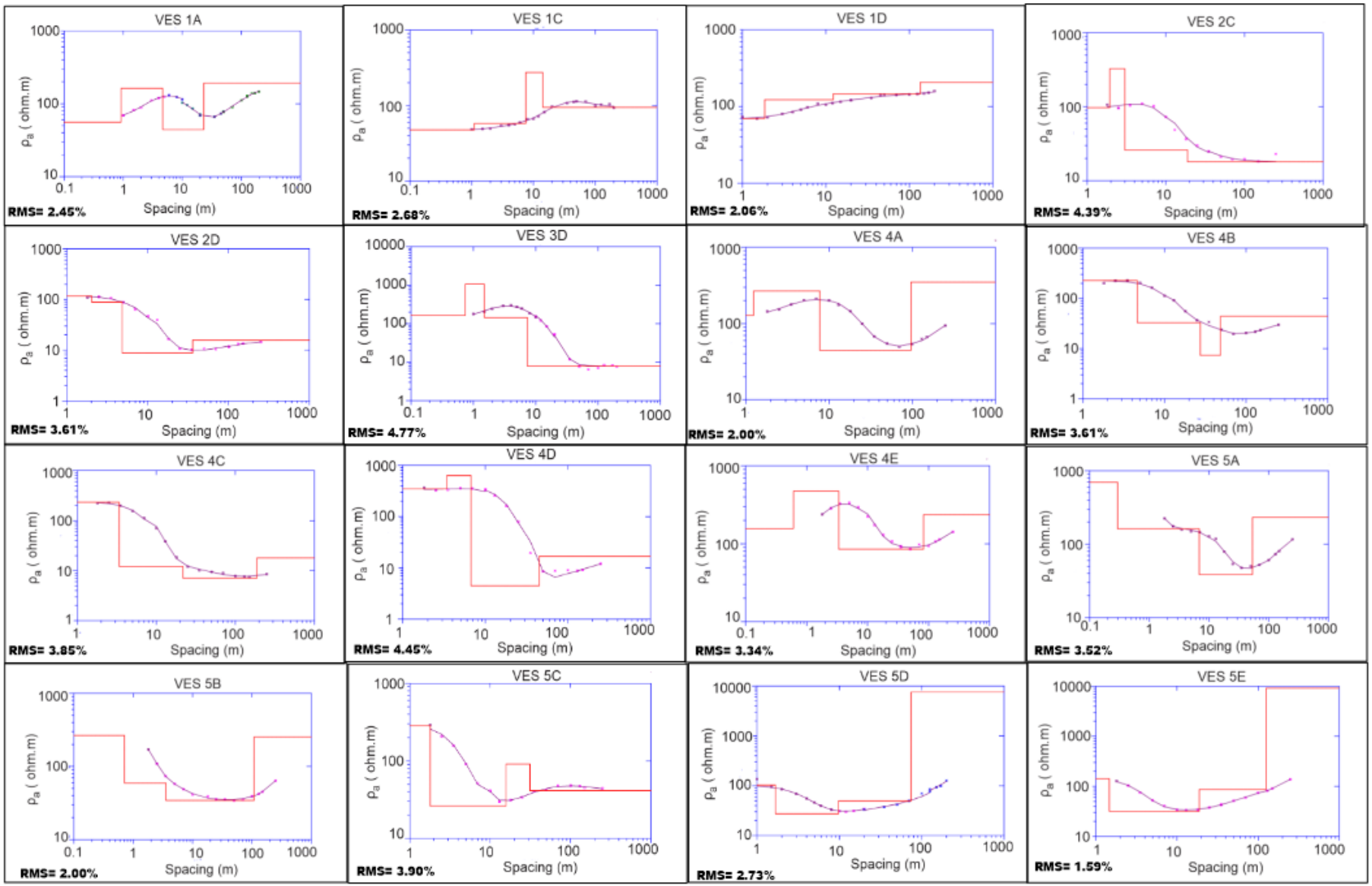

Figure 4.10. VES 4-layer models showing the AA, HA, HK, KH, KQ, and QH field curves.

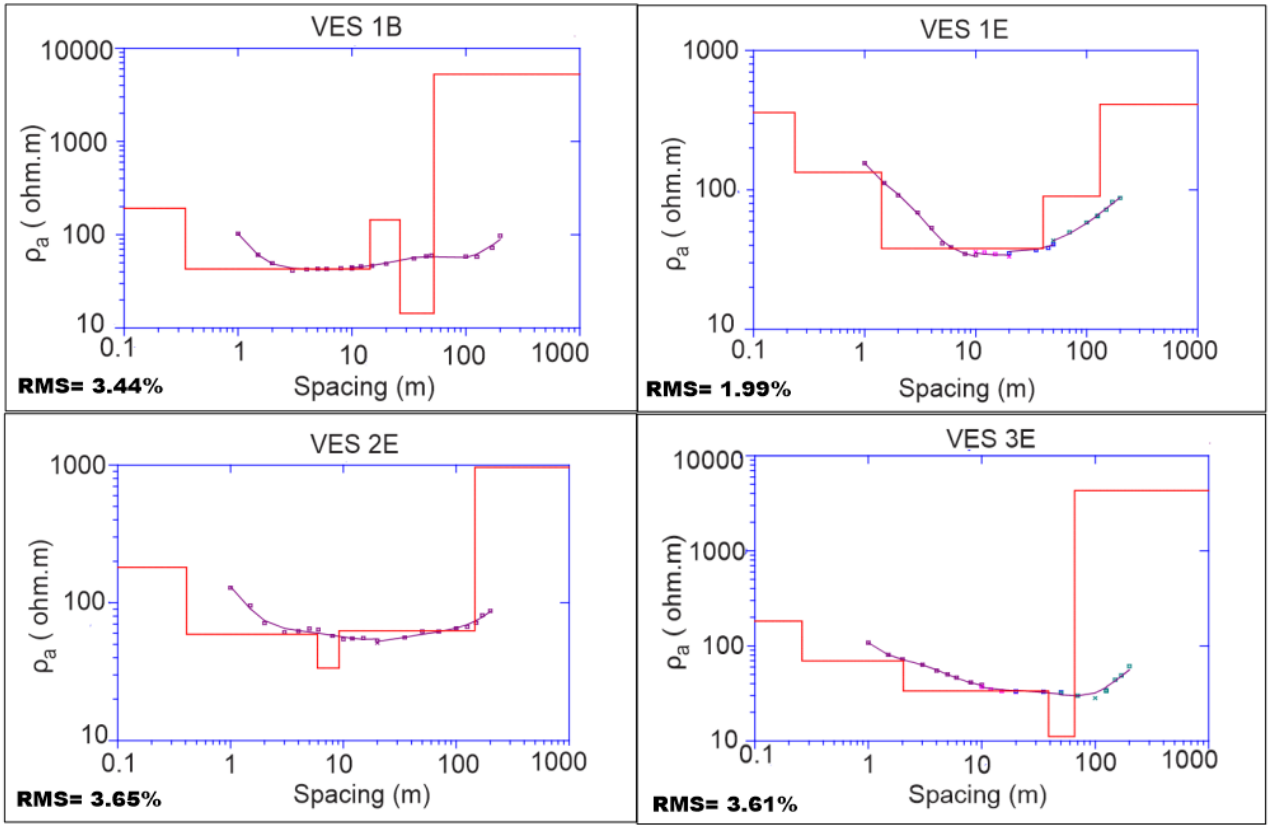

Figure 4.11. VES 5-layer models showing the HKH, QHA, and QQH field curves.

The resistivity values obtained across the basin were classified as low (<100 ohm.m), medium (100-1000 ohm.m), and high (> 1000 ohm.m). The distributions of the curve types are shown in (Figure 4.12) with the predominant field curve in the area being the H-type combination curves with mostly a three-layer and four-layer setup (Figure 4.13).

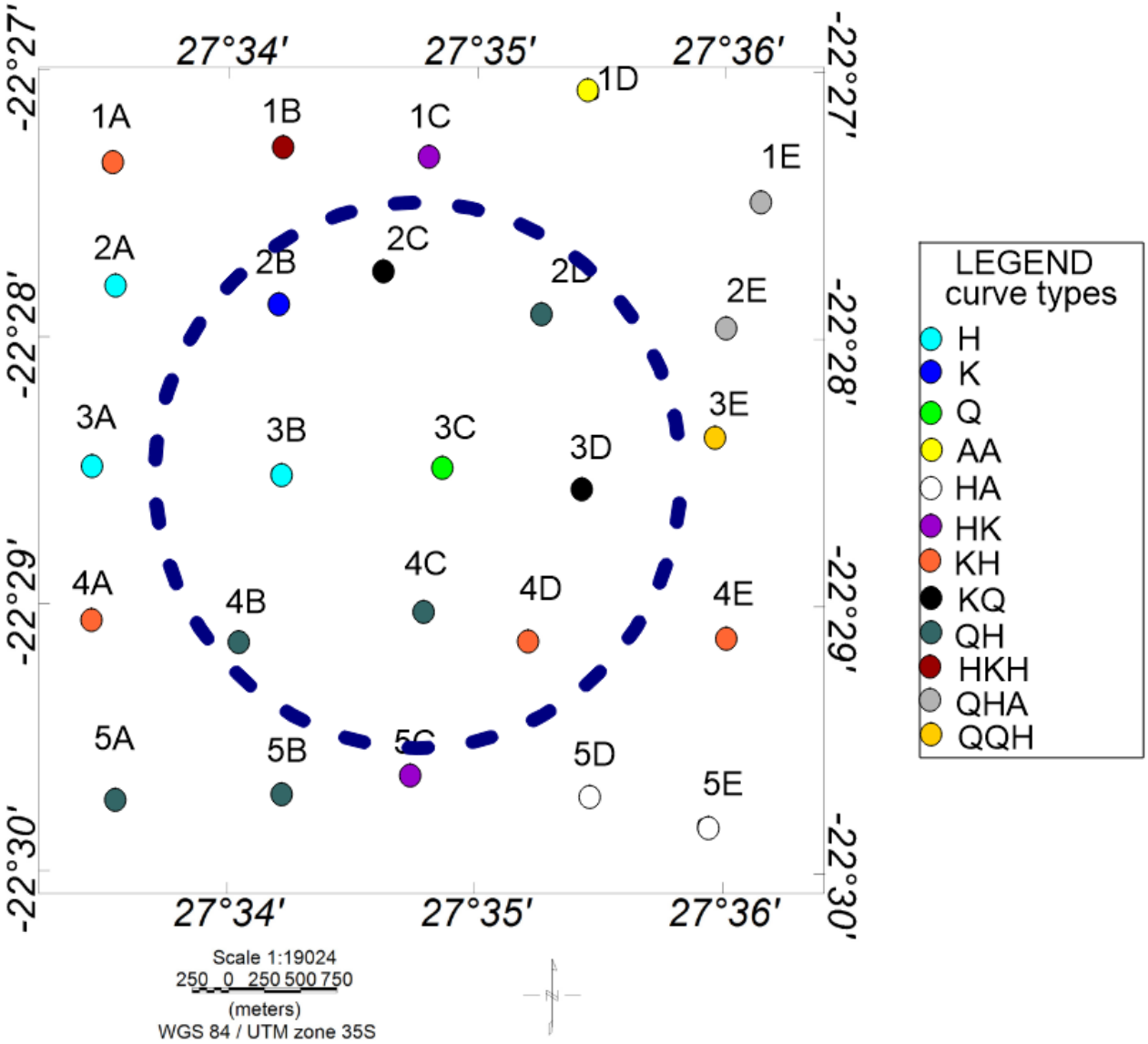

Figure 4.12. Map of study area showing the distributions of the curve types across the basin. Blue dotted lines represent the boundary of the basin derived from gravity analysis.

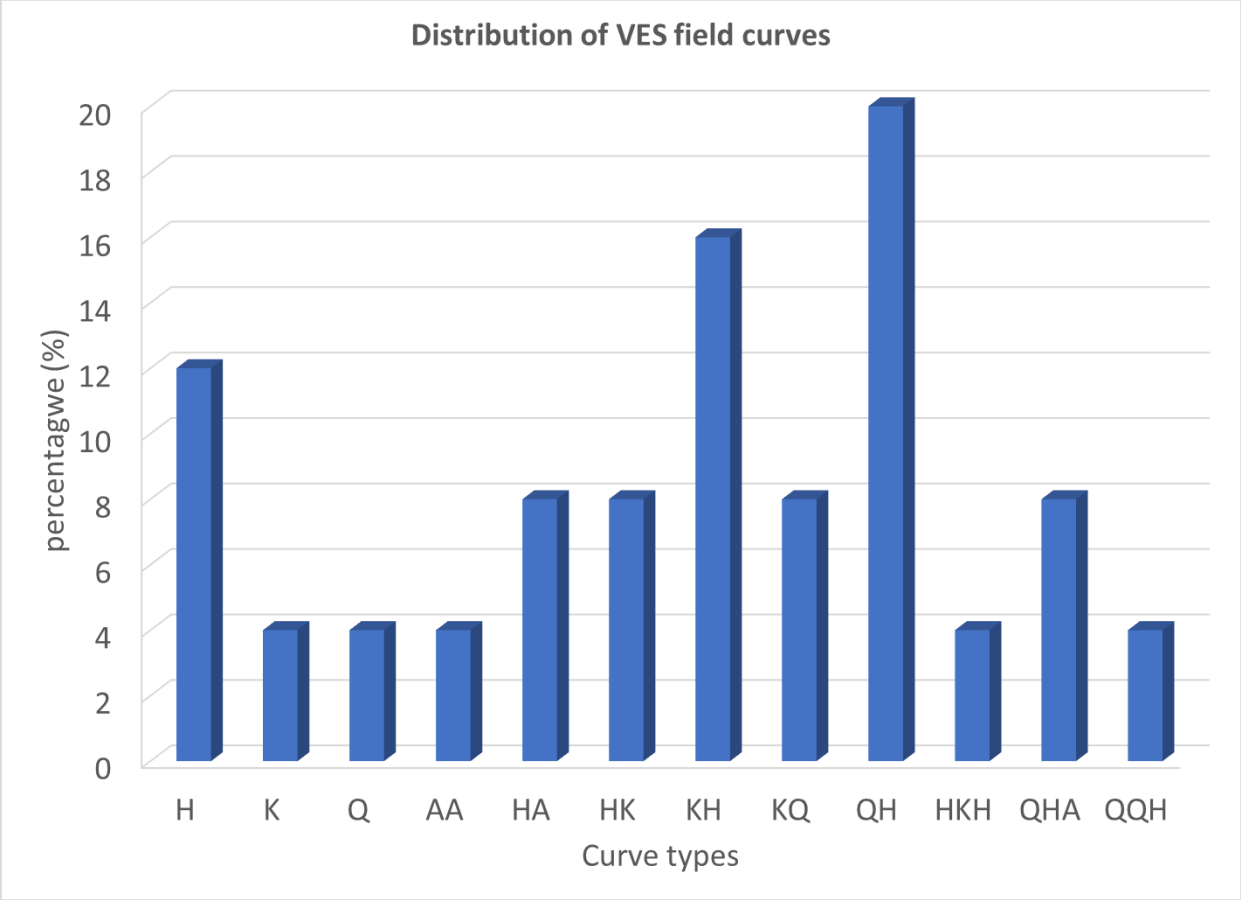

Figure 4.13. Graph showing the percentage distribution of curve types in the study area.

Iso apparent resistivity maps (Figure 4.14) were constructed for different electrode spacings (AB/2), to analyse the lateral distributions of the apparent resistivities on a horizontal plane at different depth penetrations. Resistivity signature corresponding to a range of sediments was observed. A central resistivity low is observed from AB/2= 50m to AB/2=500m. The resistivities are seen to gradually increase from the centre to the edges/boundary of the basin. Resistivities in the crater range from 6-193 ohm.m and those of the surrounding area range 43-3454 ohm.m, indicating that the sediments within the basin are more conductive as compared to those outside the basin.

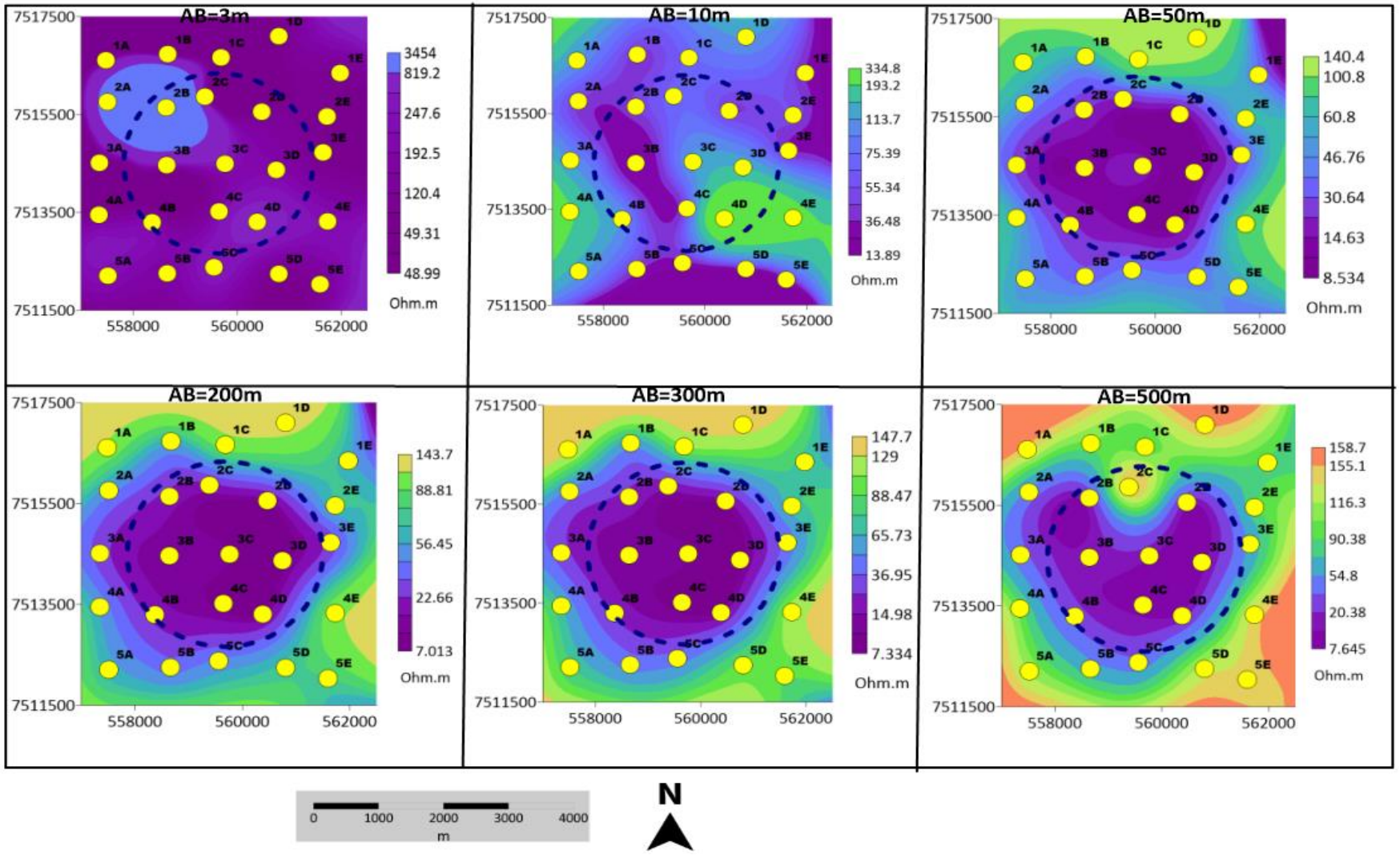

Figure 4.14. Iso apparent resistivity maps showing the distribution of electrical resistivity across the structure. Blue dotted lines represent the boundary of the basin derived from gravity analysis. Yellow dots represent the VES stations.

A Borehole of in the area (Figure 2.2), was used to provide the basis for calibrating geoelectrical sections as shown in Figure 4.15. The borehole used is located between VES 2C and 2D therefore these VES stations were correlated with the borehole log to estimate 2-D geoelectrical sections covering the top 100m of the basin. This correlation yielded a geoelectrical section interpreted as follows: low resistivity (<100 ohm.m) was suggested to be clay/mud/silt/marl/grit, medium resistivity (100-1000 ohm.m) might represent calcrete/sand and high resistivity (> 1000 ohm.m) can be gravel/conglomerate/sand.

The illustrated section setup was then used to formulate five geoelectrical sections of five profiles cutting across the structure in the W-E direction (Figure 4.16). The geoelectrical sections of these profiles obtained generally suggest that the shallow basin fill is made up of alternating layers of clay/mud/silt/marl/grit and calcrete/sand. A graben-like structure was observed in profile 1 (Figure 4.17a), suggesting that these sediments could be faulted or structurally controlled. In profiles 1, 2,3, and 5, (Figure 4.17a, 4.17c and 4.17e) the gravel/conglomerate/sand layer was mapped at or near the edges of the basin at depths between 60 to 65m.

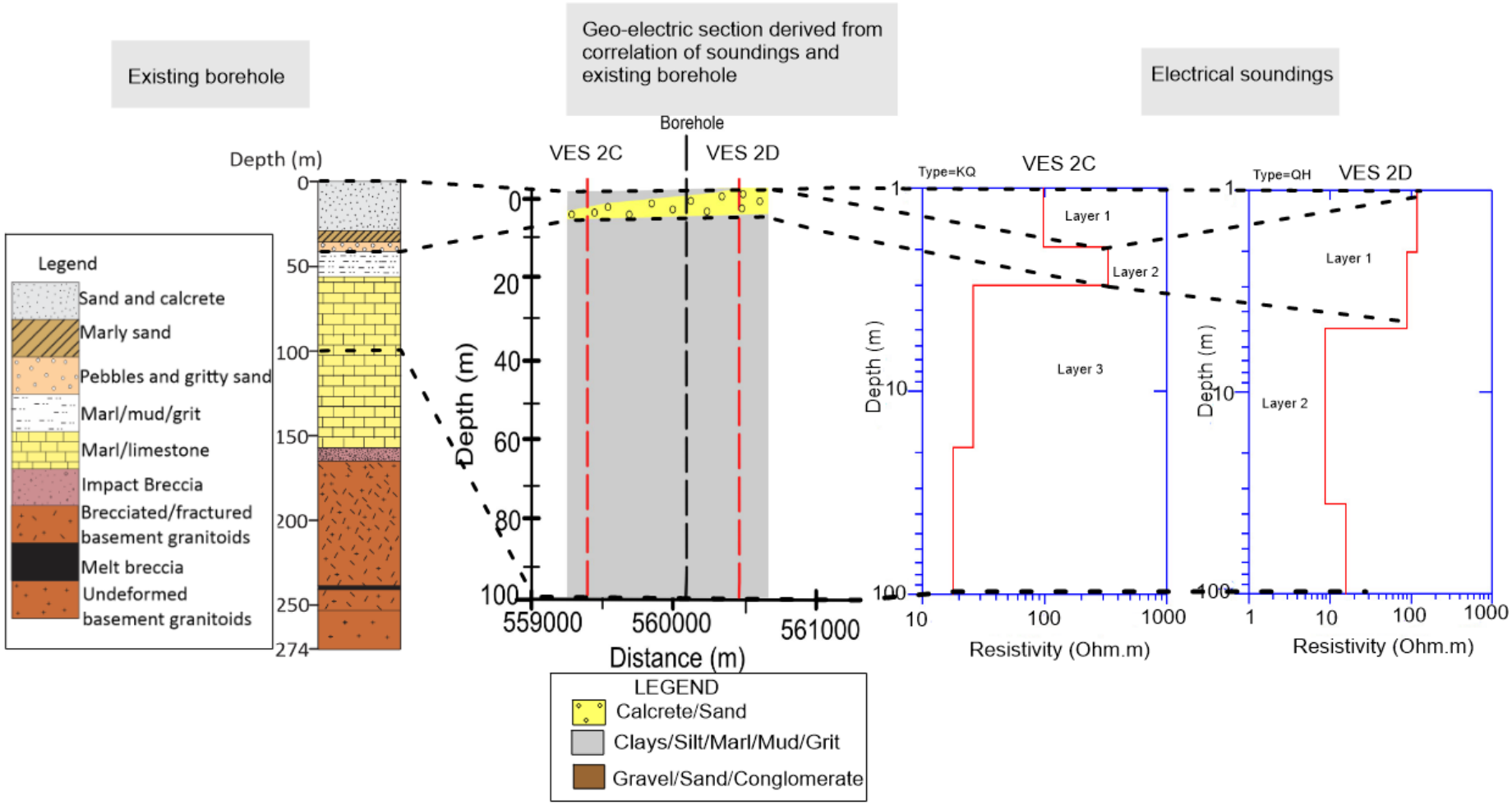

Figure 4.15. Borehole correlation with two VES stations near the borehole. A geoelectrical section was derived from this correlation.

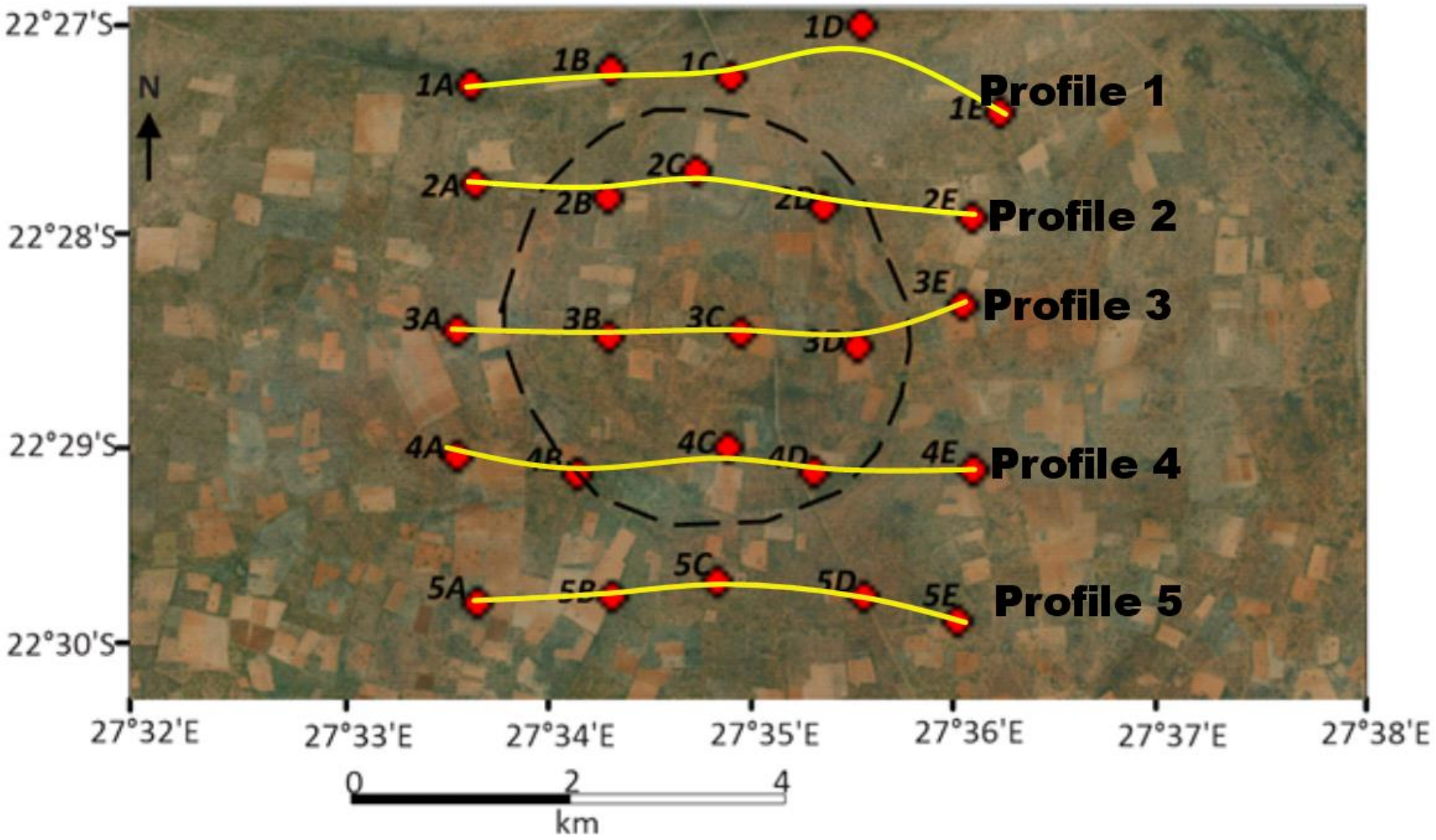

Figure 4.16. Map showing the location of the 2-D geoelectrical profiles.

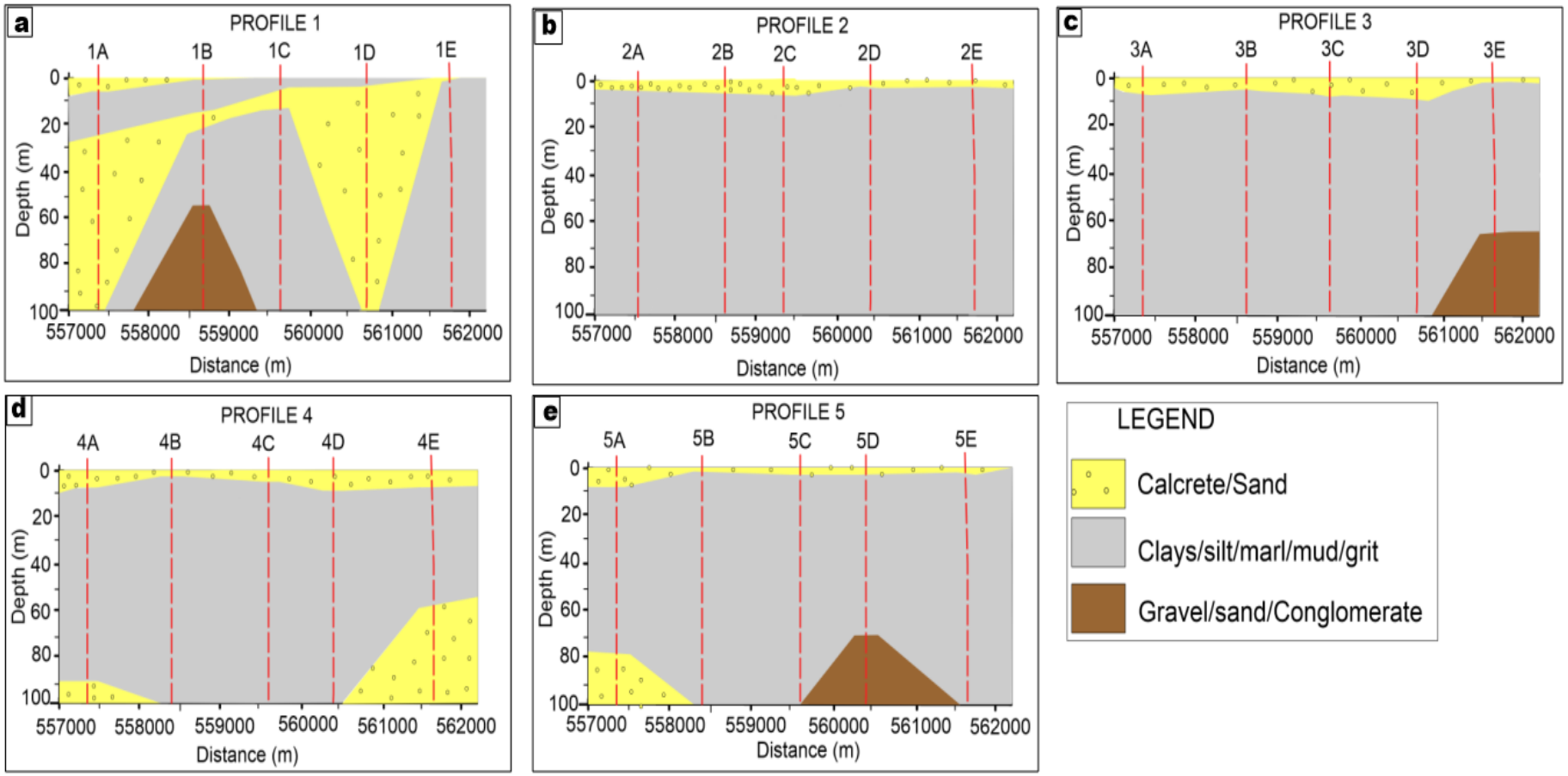

Figure 4.17. 2-D geoelectrical profiles in the West-East direction across the basin.

Chapter 5

Discussion

The predominant magnetic response of small impact structures is a magnetic low/ quiet zone which manifests as a deviation from the regional magnetic signature (Therriault et al., 2002). This magnetic response was observed over the Kgagodi basin, which showed a distinctive smooth magnetic signature compared to the complex and noisy signature of the surrounding environment. This signature observed correlates with the results of ground magnetics in the area by Brandt et al. (2002). The Kgagodi basin formed in the Archean granitoid basement which was already overlain and intruded by the Karoo dolerites (Brandt et al., 2002). The NW-SE trending regional lineament interpreted as a dolerite dyke (Figure 5.1) is discontinuous at the crater rim, suggesting that the dyke came earlier than the impact event. Brandt et al. (2002) constrained the upper age limit of the Kgagodi crater impact event at 180 Ma and indicated that Karoo intrusions of generally 180 Ma exist in most regions of southern Africa. Another suggestion is that the dyke and the impact crater might have formed around the same period. In addition, the Kgagodi basin has been suggested to present an intersection of two fault lines (Brandt et al., 2002; Reimold & Koeberl, 2014), hence the regional dyke observed could also represent a pre-existing regional fault line that intersects with a localized fault line, which was observed in the magnetics data trending NE-SW.

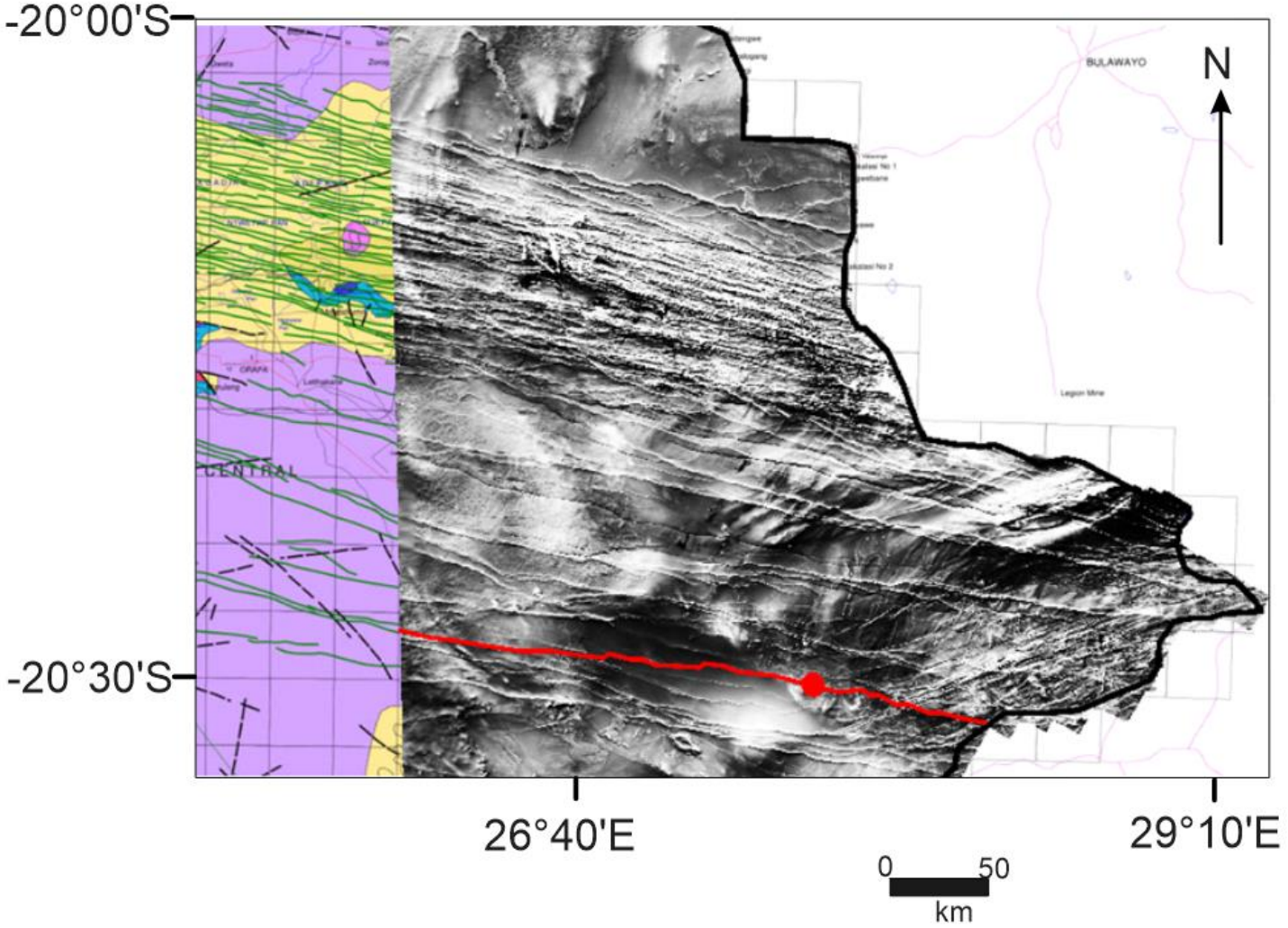

Figure 5.1. Greyscale TMI Map of Eastern Botswana overlain on Eastern Botswana geologic map showing regional structures. The geologic map is from (Key & Ayres, 2000). The green lines in the geologic map indicate the Karoo dolerite dykes and the black lines represent the faults. The red line in the grey image scale is the NW-SE trending lineament observed cutting across the Kgagodi basin. The Kgagodi basin is shown by the red dot in the greyscale image.

A gravity survey was carried out to define the 3-D geometry of the Kgagodi basin. An Impact structure that has not been eroded to or beyond the crater floor shows a negative gravity anomaly (Reimold & Koeberl, 2014). The expected results of a gravity survey over a simple impact crater is a negative and roughly circular anomaly (Brandt et al., 1998). The Bouguer anomaly obtained in this study over the Kgagodi basin showed a circular negative gravity anomaly. These results were in agreement with previous gravity surveys conducted in the area (Paya et al., 1999; Brandt et al., 2002). The negative anomaly in craters is caused by low-density material resulting from both physical and lithological changes associated with the cratering process (Pilkington & Grieve, 1992). This material includes post-impact sediment fill, however, the majority of the density contrast could mostly be due to fracturing and brecciation of the target rocks which leads to increased porosity, resulting in low densities in craters than their surrounding environment (Pilkington & Grieve, 1992; Raiskila, 2013; Reimold & Koeberl, 2014). Results of the Euler deconvolution depths overlain on the residual BA confirmed that the dolerite dyke is discontinuous at the rims of the basin (Figure 5.2). The proposed fault from the magnetics data can also be seen correlating with some high-density units within the basin (Figure 5.3).

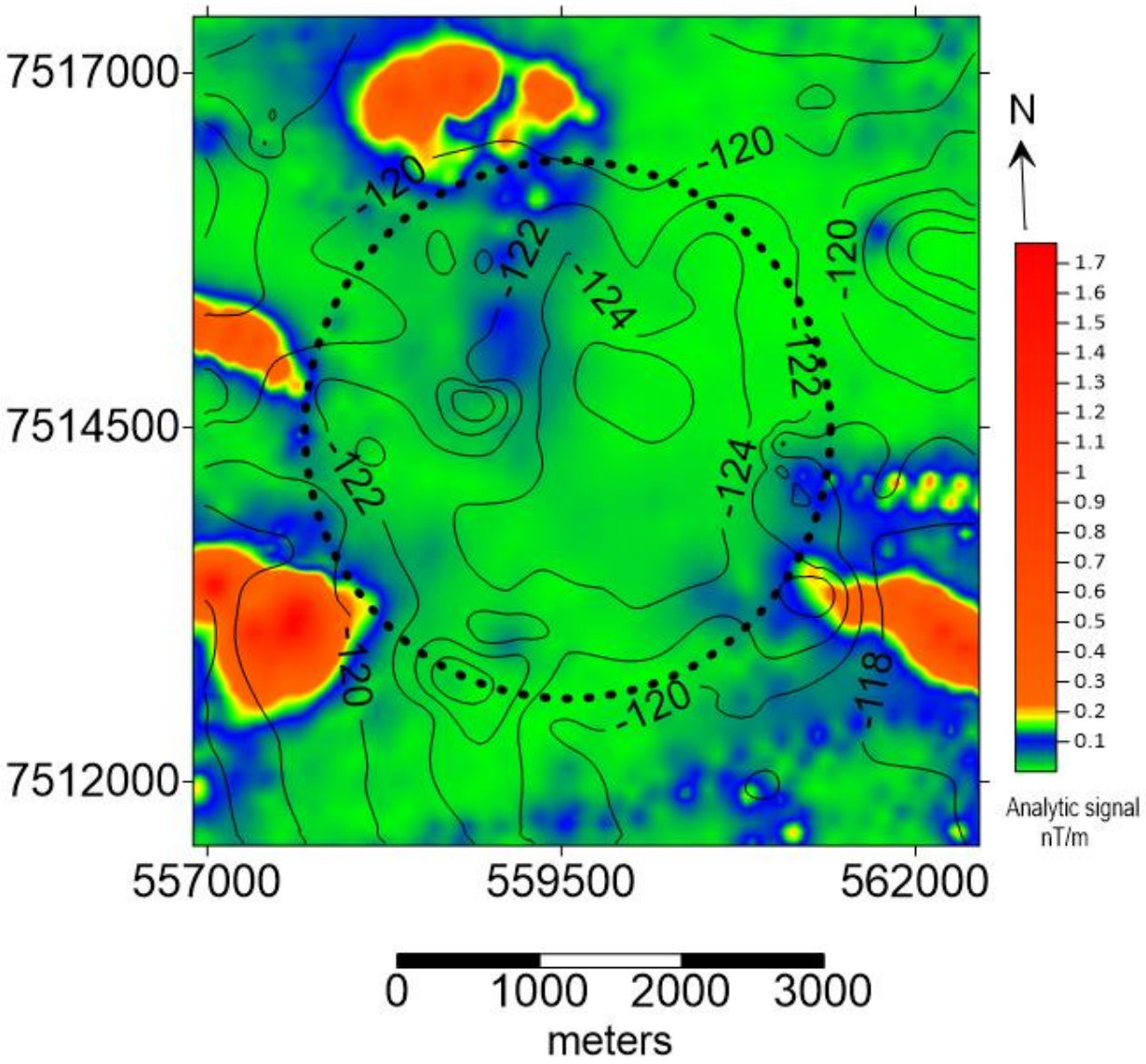

Figure 5.2. Map showing gravity contours overlain on Analytic signal grid. BA contours are in mGal. The circle is the Kgagodi basin boundary derived from gravity results.

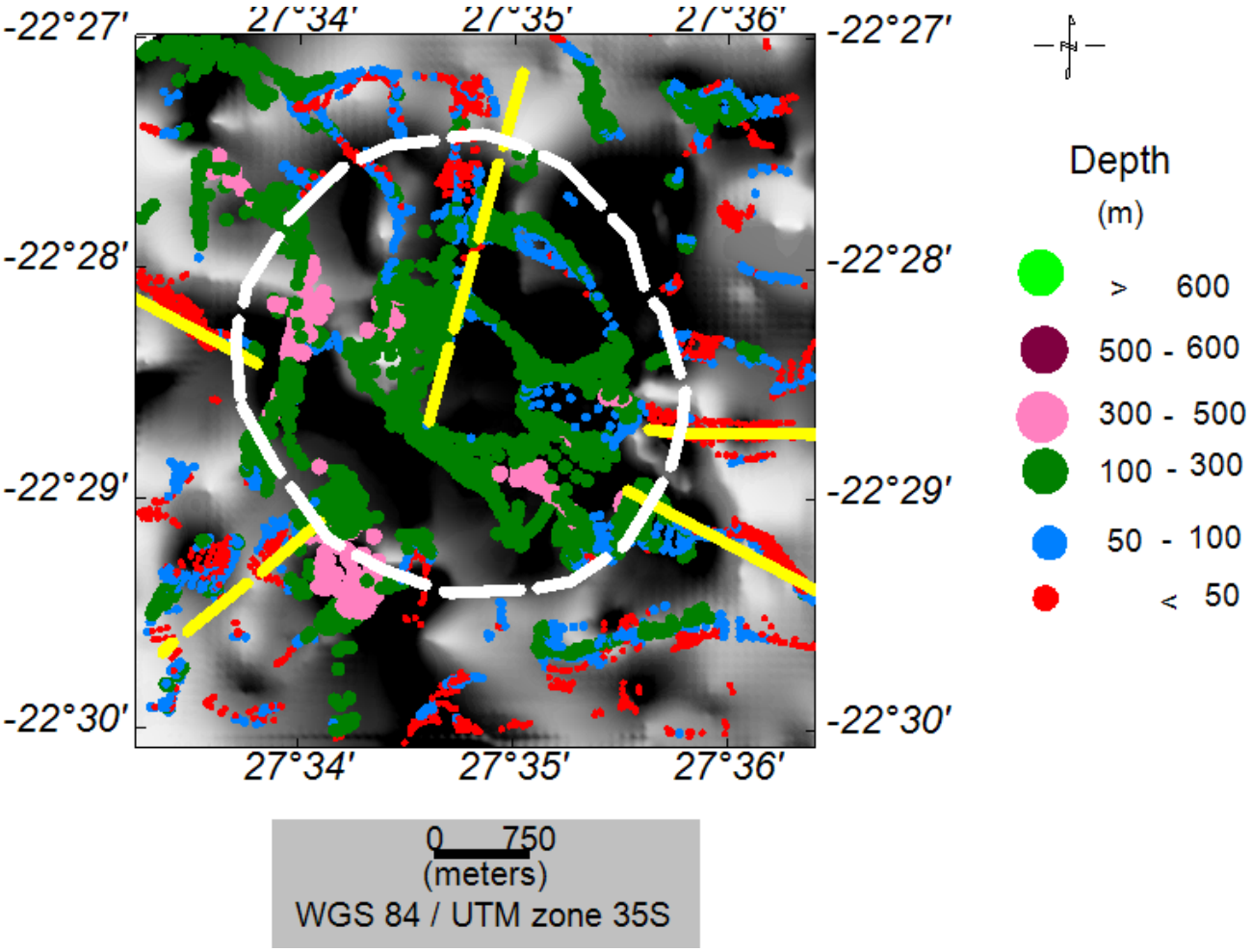

Figure 5.3. Euler depths are overlain on greyscale residual Bouguer anomaly. The bright areas are the high-density anomalies, and the dark areas are the low-density anomalies. Dashed lines represent a possible fault and solid lines represent the dykes. the circle represents the Kgagodi basin boundary from the satellite image.

Vertical slices from the 3-D density model cutting across the centre of the structure showed a bowl-shaped depression. The structure observed is similar to the morphological description of a simple crater by Grieve (2005) as indicated in Figure 5.5. Based on a borehole log (Figure 5.4) published by Brandt et al. (2002) obtained about 400 m from the impact crater rim, the constituents of the approximately 700-900m thick, low-density allochthonous material that occurs at the centre of the crater may be inferred to be mostly sand, calcrete, marl, mud, and limestone. Furthermore, this borehole log reveals that below this sedimentary sequence, there is some occurrence of impact breccia material, followed by fractured granitoid rocks with a small amount of melt breccia. This can be correlated with the parabolic lens of low densities observed in the 3-D density model, which is interpreted to be allochthonous material and highly shocked and melted target material (existing rock prior to impact). This lens is normally described as polymictic and the depth to the top of it (the breccia lens) is approximately 1/6 of the rim diameter and it marks the apparent crater (e.g. Therriault et al., 2002.; Grieve, 2005). The results obtained for this study indicate that the top of the lens is approximately 700-900m at the centre of the Kgagodi basin.

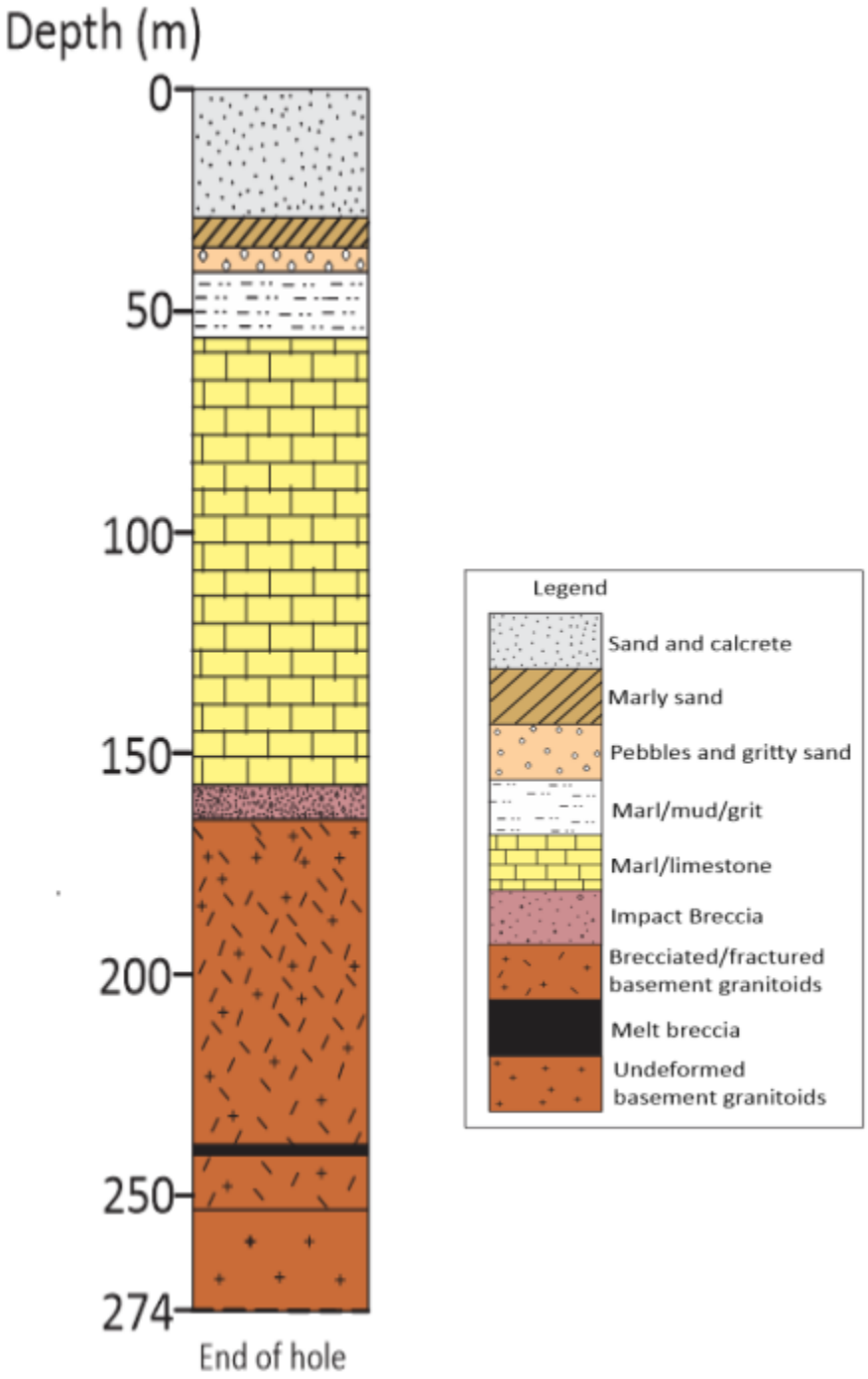

Figure 5.4. Schematic borehole log for the drill core obtained in the Kgagodi basin (Brandt et al., 2002).

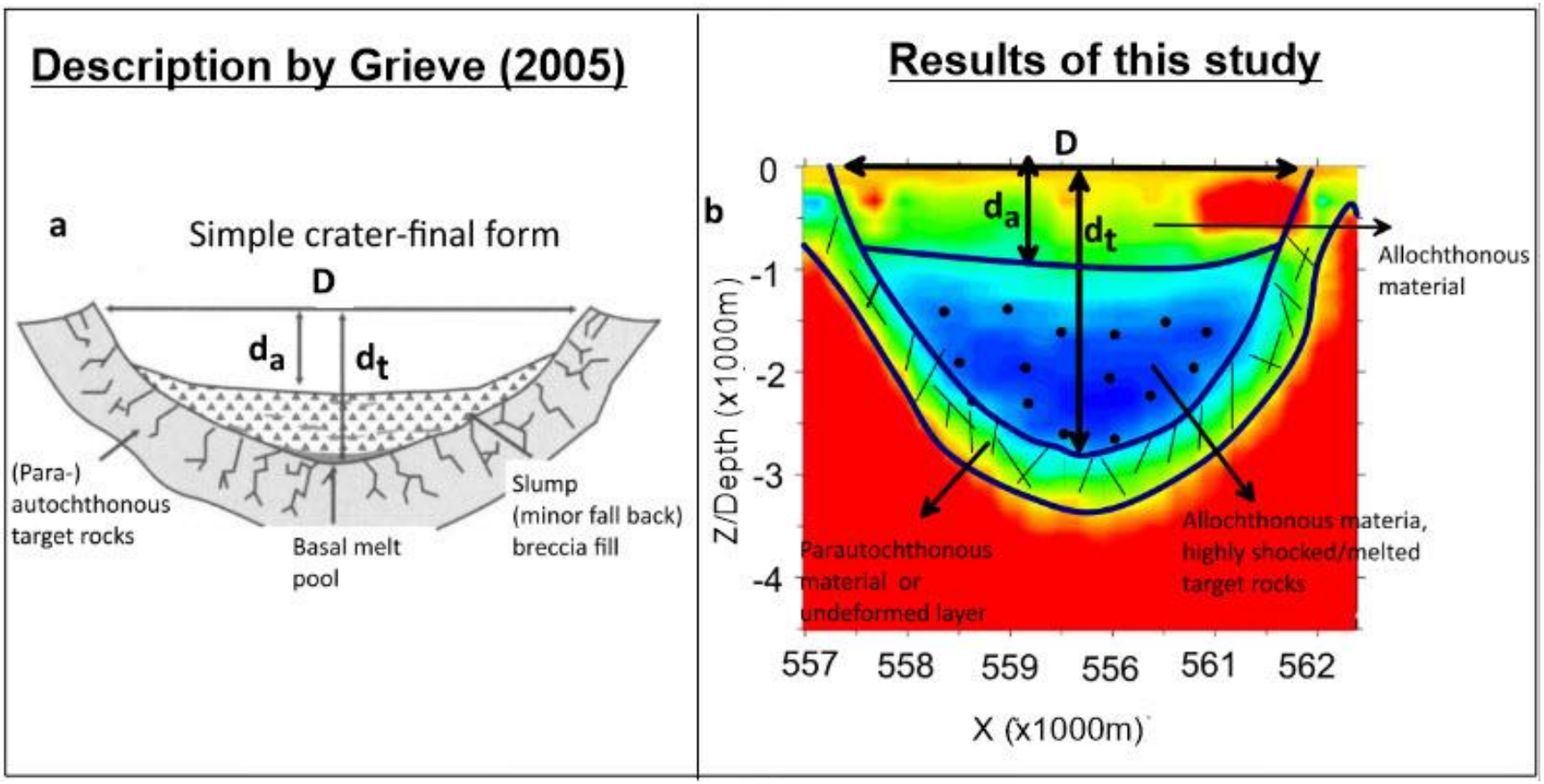

Figure 5.5. (a) This is a schematic cross-section of a terrestrial simple impact structure. No vertical exaggeration. D is diameter and da and d t are apparent and true depth, respectively (Grieve,2005). (b) shows a slice from the 3-D density model of the current study compared with the morphological description of a simple impact crater by Grieve (2005).

The borehole in the basin (Figure 5.4) further indicates that the bottom and final layer is made up of granitoids which grades with depth into a less fractured and finally undeformed basement. This layer can be correlated with the high-density layer beneath the breccia lens in the 3-D model which was interpreted as the parautochthonous material or undeformed layer. Parautochthonous fractured rocks define the walls and floor of the true crater (Therriault et al., 2002.; Grieve, 2005).

Brandt et al. (2002) estimated the diameter of this structure to be 3-4 km. The combined gravity results of the current study estimate the diameter of the Kgagodi basin to be approximately 3.5 km. Generally, the gravity low extends to or slightly beyond the crater rim (Pilkington & Grieve, 1992; Brandt et al., 1998) which might explain why the gravity low observed in this study extends to a diameter of approximately 4 km in the Bouguer anomaly. Simple impact structures generally have upraised rims but due to post-impact tectonic activities like erosion, their primary morphology can be changed (Grieve, 2005; Reimold & Koeberl, 2014). The rims of the Kgagodi basin are not clearly defined in the 3-D sections which might indicate that they have been affected by post-impact tectonic activities.

Geoelectrical methods have been successfully used to map the thickness of near-surface lithologies like the post-impact fill and breccia (Hawke, 2004; Tong et al., 2010). Traditionally, electrical imaging of impact structures involved the use of vertical electrical sounding and few impact structures have been surveyed using the method, possibly due to the expensive nature of these surveys compared to the potential field methods and the inability effectively resolve the internal structure of the crater (Pilkington & Grieve, 1992; Hawke, 2004; Tong et al., 2010). The

vertical electrical sounding survey in this study aimed to investigate the shallow geoelectrical units within the crater. Low resistivity values are expected for allochthonous post-impact sedimentary infill and breccia due to the high permeability and porosity of these layers whereas impact melt might be expected to have higher resistivities due to its low porosity (Hawke, 2004).

The lateral resistivity variations obtained in this study were generally weak which is typical of electrical soundings in sedimentary environments (Auken et al., 2005). In addition, electrical methods can fail to recognize the low contrast gap between low resistivity materials such as shale and clay (Yusoh et al., 2018). The maximum depth reached in this study was approximately 167m. The results of this study suggest that a highly conductive layer (6-100 Ω.m) made of clays/mud/sit/marl/grit is generally overlain and underlain by a less conductive layer (100-1000 Ω.m) made of calcrete/sand. This resistivity layer arrangement describes the H-type curve (i.e., a layer of good conductance in between two less conductive layers). Hence the H-type combination of curves is dominant in the area, suggesting the area has good water potential (Sajeena et al., 2015). This finding correlates with suggestions that the Kgagodi basin could be an important hydrological target (Brandt et al., 2002; Reimold & Koeberl, 2014). A sporadic layer of resistivities greater than 1000 Ω.m interpreted as gravel/conglomerate/sand was mapped near or at the edge of the crater and mostly at depths below 60-65m.

Isoapparent resistivity maps showed that the basin has a central resistivity low which is consistent with the BA anomaly obtained (Figure 5.6). The central resistivity low also corresponds to the smooth magnetic signature of the basin (Figure 5.7). In VES a small graben-like structure correlating with the proposed fault from aeromagnetic data was observed. All the resistivity

layers mapped in this study can be suggested to belong to the allochthonous section of the 3-D density model indicating that the VES technique only mapped part of the basin fill.

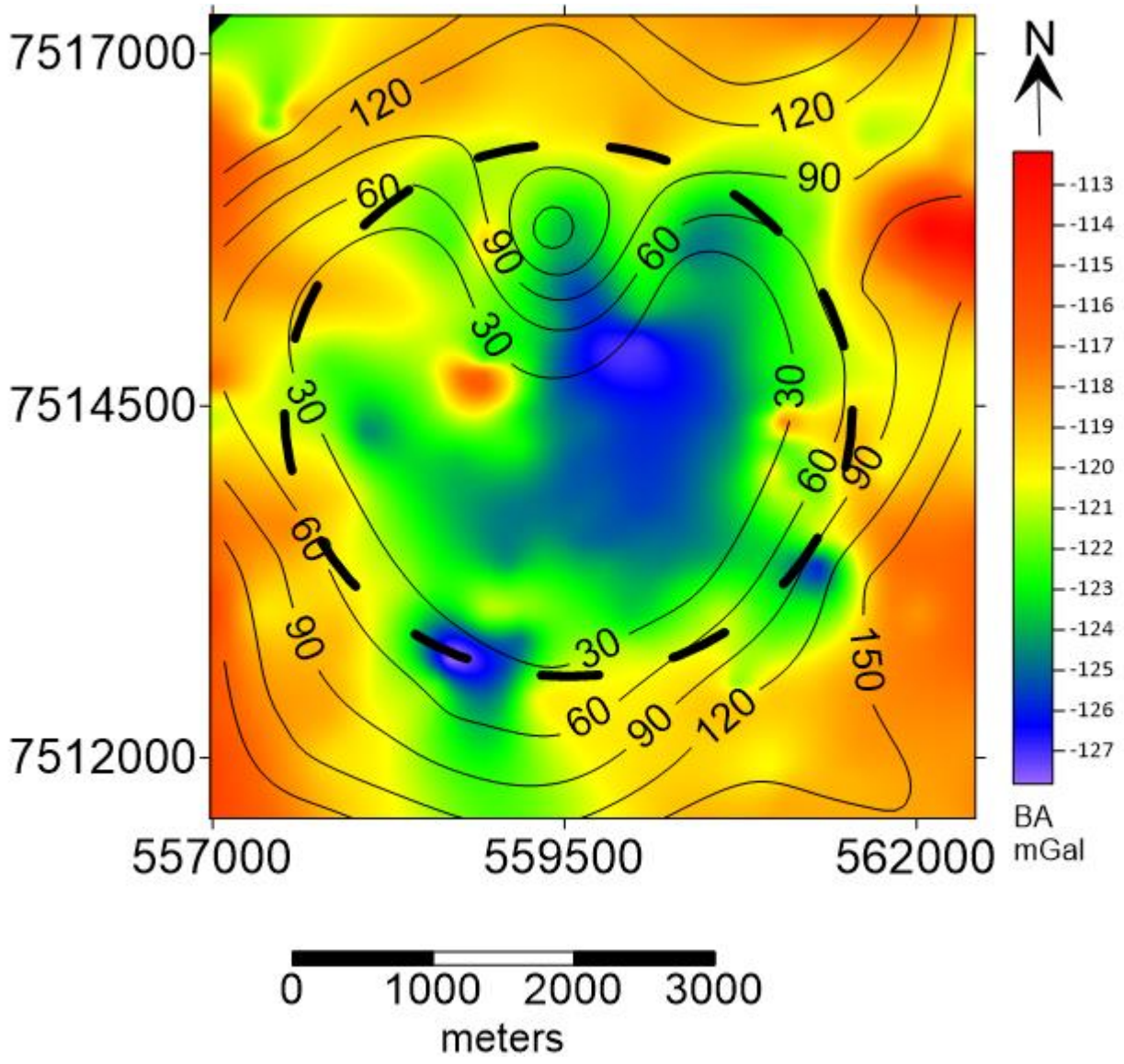

Figure 5.6. Map showing VES contours at AB=500m overlain on Bouguer anomaly grid. VES contours are in ohm.m. The circle is the boundary derived from gravity results.

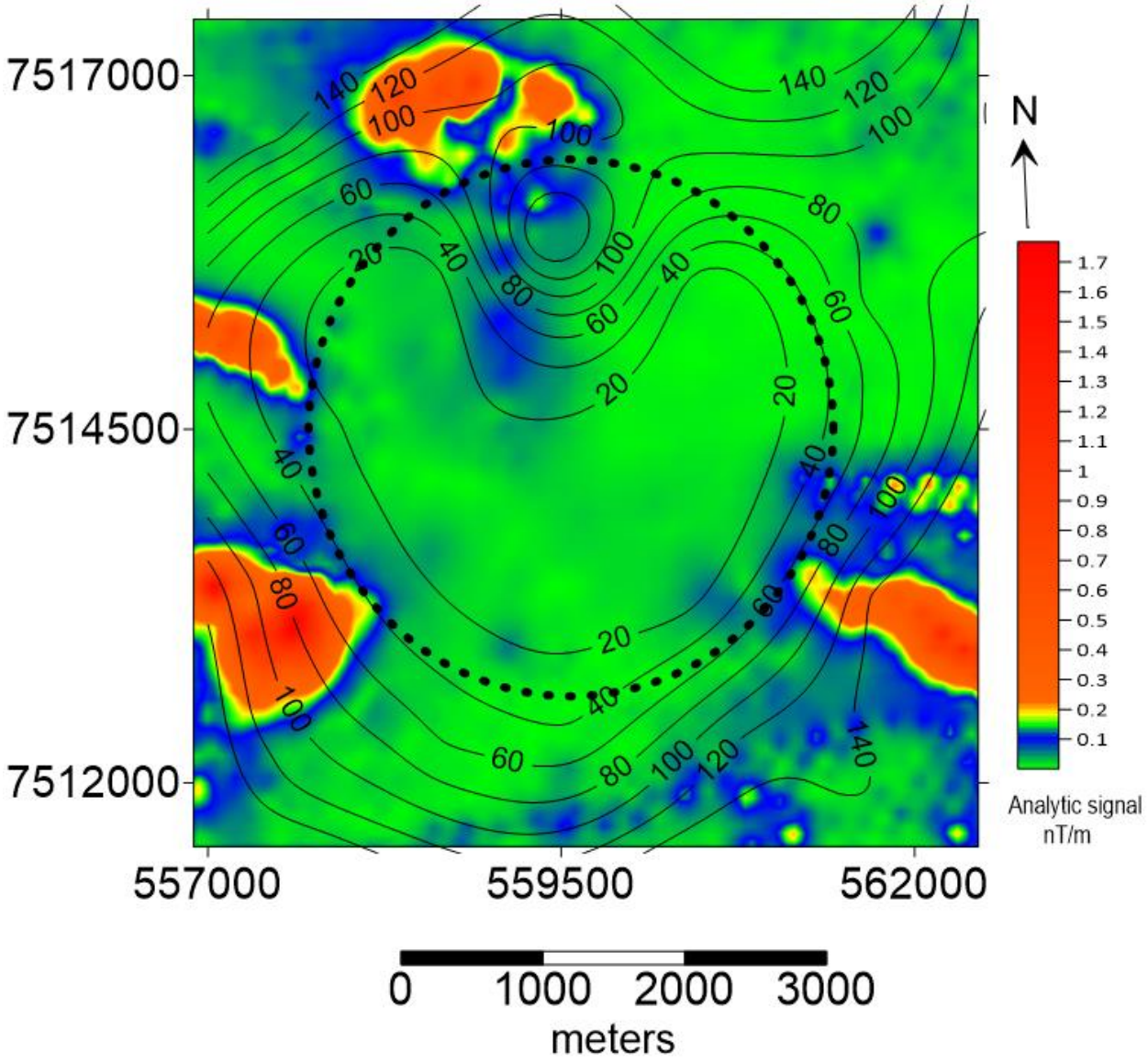

Figure 5.7. Map showing VES contours at AB=500m overlain on the analytical signal map grid. VES contours are in ohm.m. The circle is the boundary derived from gravity results.

The resistivity lows over craters normally match the extent of the magnetic and gravity anomalies and are related to fracturing (Pilkington & Grieve, 1992). This was observed to also be the case for the Kgagodi basin (Figure 5.8) confirming that the basin fill is made up of sediments and possibility fractured and brecciated geologic material.

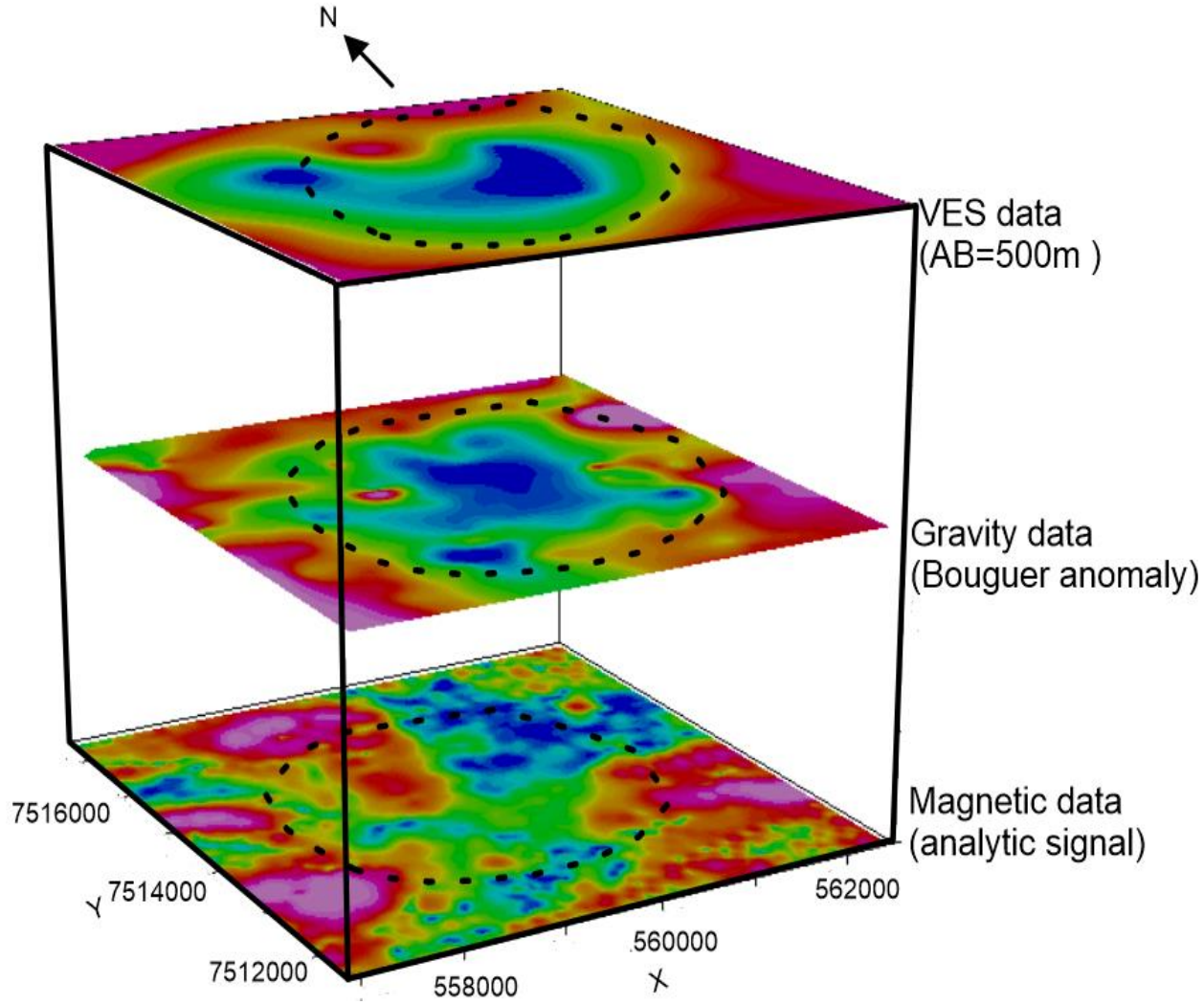

Figure 5.8. Grids showing the correlation of the aeromagnetic data, Gravity data, and the VES data. The red colours are the highs (I.e., high magnetic signature, high density signature, and high resistivity signature) and the blue and green indicate the lows (i.e., low magnetic signature, low density signature, and low resistivity signature).

Chapter 6

Conclusions

This study aimed at delineating the geologic structures within the Kgagodi basin and determining the 3-D geometry of the Kgagodi basin. To achieve this aim, three objectives were established. For each objective the following conclusions were made:

***Objective 1**: To Investigate the structural characteristics and evolution of the basin, from analysis of existing high-resolution aeromagnetic data.*

- Two major lineaments exist in the Kgagodi basin. A regional lineament trending NW-SE which was interpreted to be a dolerite dyke and a NE-SW trending lineament which was inferred to represent a localised fault. The two lineaments could be an intersection of two fault lines.
- The dolerite dyke in the basin area is discontinuous at the basin rims therefore referring to the principle of cross-cutting relations, this dyke can be suggested to be older than or relatively the same age as the Kgagodi basin (i.e., approximately more than or equal to 180 Ma).

***Objective 2**: To evaluate the basin fill thickness and morphology of the basin by interpretation of ground gravity data.*

- This study revealed that the Kgagodi basin has a simple bowl-shaped depression and a diameter of ~3.5 km.
- The apparent depth of the Kgagodi basin is ~900m, indicating that the post impact /basin fill material is about 900 m thick.

- A parabolic lens of possibly impact generated material exists at about 700-900m and extends to depths of approximately 2700m.

***Objective 3**: To investigate the shallow geoelectrical units within the basin using the Vertical Electrical Sounding (VES) technique.*

- The shallow basin fill (top 100m) is made up of possibly faulted low resistive materials, with signatures corresponding to those of sediments. Based on borehole information, literature review and resistivity signatures obtained these sedimentary units are sandstones, clays, silt, marl, gravel, conglomerate, and sands.
- The dominance of the H-type combination of curves obtained suggests that the area has good groundwater potential.

REFERENCES

Abraham, A. A., Flexor, J. M., & Fontes, S. L. (2004). Geophysical signature of Serra da Cangalha impact crater, Brazil. Meteoritics and Planetary Science Supplement, 39,5167. https://doi.org/10.1111/j.1945-5100.2004.tb00346.x.

Ahmed, Z., Lawal, K. M., & Ahmed, A. L. (2018). Interpretation of High Resolution Aeromagnetic Data of Part of Southwestern Nigeria for Subsurface Mapping. Dutse Journal of Pure and Applied Sciences, 4(2), 221-235.

Aldiss, D. T. (1991). The Motloutse Complex and the Zimbabwe craton/Limpopo belt transition in Botswana. Precambrian Research, 50(1-2), 89-109. https://doi.org/10.1016/0301-9268(91)90049-G

Ansari, A. H., & Alamdar, K. (2009). Reduction to the pole of magnetic anomalies using the analytic signal. World Applied Sciences Journal, 7(4), 405-409.

Auken, E., Christiansen, A. V., Jacobsen, B. H., Foged, N., & Sørensen, K. I. (2005). Piecewise 1-D laterally constrained inversion of resistivity data. Geophysical Prospecting, 53(4), 497-506. https://doi.org/10.1111/j.1365-2478.2005.00486.x

Bala, B., Lawal, K. M., Ahmed, A. L., Umar, M., Mohammed, M. A., & Adamu, A. the use of analytic and first derivative techniques to gain insight into aeromagnetic anomaly patterns in part of ikara, Nigeria.

Beard, L. P. (2012, March). Magnetic Anomalies of Impact Craters at Low Magnetic Latitudes. In 25th Symposium on the Application of Geophysics to Engineering & Environmental Problems (pp. cp-329). European Association of Geoscientists & Engineers. https://doi.org/10.4133/1.4721703

Bernard, J. E. A. N. (2003). Short note on the depth of investigation of electrical methods. IRIS Instruments.http://www.iris-instruments.com/Pdf_file/Resistivity_Imaging/methods_ depth_investigation. pdf.

Binley, A. (2015). DC electrical methods. In G. Schubert (Ed.), Treatise on geophysics (2nd ed., Vol. 11, pp. 233-259). Elsevier. https://doi.org/10.1016/B978-0-444-53802-4.00192-5

Blakely, R. J. (1996). Potential theory in gravity and magnetic applications. Cambridge university press. https://doi.org/10.1017/CBO9780511549816

Bodoky, T., Kis, M., Kummer, I., & Don, G. (2006). The telluric conductivity anomaly at Magyarmecske: is it a buried impact crater. In 40th ESLAB Proceedings CD–First International Conference on Impact Cratering in the Solar System, Noordwijk. https://doi.org/10.1556/ceugeol.50.2007.3.2

Brandt, D., Holmes, H., Reimold, W. U., Paya, B. K., Koeberl, C., & Hancox, P. J. (2002a). Kgagodi Basin: The first impact structure recognized in Botswana. Meteoritics & Planetary Science, 37(12), 1765–1779. https://doi.org/10.1111/j.1945-5100.2002.tb01162.x

Brandt, D., Remold, W. U., Franzsen, A. J., Koeberl, C., & Wendorff, L. (1998). Geophysical profile of the Roter Kamm impact crater, Namibia. Meteoritics & Planetary Science, 33(3), 447–453. https://doi.org/10.1111/j.1945-5100.1998.tb01649.x

Casto, D. W. (2001). Calculating depths to shallow magnetic sources using aeromagnetic data from the Tucson basin (Doctoral dissertation, US Department of the Interior, US Geological Survey). https://doi.org/10.3133/ofr01505

Clark, D. A., & Emerson, D. W. (1991). Notes on rock magnetization characteristics in applied geophysical studies. Exploration Geophysics, 22(3), 547-555.https://doi.org/10.1071/EG991547

Collins, G. S., Melosh, H. J., & Osinski, G. R. (2012). The Impact-Cratering Process. Elements, 8(1), 25–30. https://doi.org/10.2113/gselements.8.1.25

Constable, S. C., Parker, R. L., & Constable, C. G. (1987). Occam's inversion: A practical algorithm for generating smooth models from electromagnetic sounding data. GEOPHYSICS, 52(3), 289–300. https://doi.org/10.1190/1.1442303

Cooper, G. R. J. (2004). Euler Deconvolution Applied to Potential Field Gradients. Exploration Geophysics, 35(3), 165–170. https://doi.org/10.1071/EG04165

Earth Impact Database. (2018). http://passc.net/EarthImpactDatabase/New%20website_05-2018/Index.html

Ejike Kingsley, N., Daniel N, O., & Johnson C, I. (2021). Structural Interpretation and Depth to the Magnetic Basement, Using Aeromagnetic Data of Nkalagu and Abakaliki Areas, Southeastern, Nigeria. International Journal of Earth Science and Geophysics, 7(2). https://doi.org/10.35840/2631-5033/1854

El Hidayah, N., Muhammad, S. B., Saad, R., & Saidin, M. (2018). Analyses of Magnetic and Gravity Data in Search for Meteorite Impact Crater at Bukit Bunuh, Lenggong, Perak, Malaysia. Journal of Physical Science, 29(3), 109–119. https://doi.org/10.21315/jps2018.29.3.9

El-Sayed, H. M., Abdel Zaher, M., Soliman, S. A., & Mohamaden, M. I. I. (2021). Geophysical investigation for sustainable development at Alamein Area, Northwestern Coast, Egypt. The Egyptian Journal of Aquatic Research, 47(1), 45–52. https://doi.org/10.1016/j.ejar.2020.07.002

Ernstson, K. (1984). A gravity-derived model for the steinheim impact crater. Geologische Rundschau, 73(2), 483–498. https://doi.org/10.1007/BF01824969

Fairhead, J. D., Mackenzie, C., Green, C. M., & Verduzco, B. (2004). A new set of magnetic field derivatives for mapping mineral prospects. ASEG Extended Abstracts, 2004(1), 1–4. https://doi.org/10.1071/ASEG2004ab042

Fedi, M., & Florio, G. (2001). Detection of potential fields source boundaries by enhanced horizontal derivative method: Potential field sources boundaries by EHD method. Geophysical Prospecting, 49(1), 40–58. https://doi.org/10.1046/j.1365-2478.2001.00235.x

Ferreira, J. C., Leite, E. P., Vasconcelos, M. A. R., & Crósta, A. P. (2015). 3-D gravity modeling of impact structures in basaltic formations in brazil: part i – vargeão, santa catarina. Revista Brasileira de Geofísica, 33(2). https://doi.org/10.22564/rbgf.v33i2.723

Finn, C., & Anderson, E. (2015). Second Projet de Renforcement Institutionnel du Secteur Minier de la République Islamique de Mauritanie (PRISM-II) Synthesis of Geophysical Data: Phase V, Deliverable 55 (Open-File Report)

French, B. M. (1999). Traces of Catastrophe: A Handbook of Shock-Metamorphic Effects in Terrestrial Meteorite Impact Structures. Meteoritics and Planetary Science, 34, 486-487. https://doi.org/10.5860/CHOICE.36-5704

French, B. M., & Koeberl, C. (2010). The convincing identification of terrestrial meteorite impact structures: What works, what doesn't, and why. Earth-Science Reviews, 98(1–2), 123–170. https://doi.org/10.1016/j.earscirev.2009.10.009

Ganguli, S. S., & Dimri, V. P. (2013). Interpretation of gravity data using eigenimage with Indian case study: A SVD approach. Journal of Applied Geophysics, 95, 23–35. https://doi.org/10.1016/j.jappgeo.2013.05.004

Glikson, A., & Uysal, I. T. (2013). Geophysical and structural criteria for the identification of buried impact structures, with reference to Australia. Earth-Science Reviews, 125, 114–122. https://doi.org/10.1016/j.earscirev.2013.07.002

Grieve, R. A. F. (2005). Economic natural resource deposits at terrestrial impact structures. Geological Society, London, Special Publications, 248(1), 1–29. https://doi.org/10.1144/GSL.SP.2005.248.01.01

Haldar, S. K. (2018). Exploration Geophysics. In Mineral Exploration (pp. 103–122). Elsevier. https://doi.org/10.1016/B978-0-12-814022-2.00006-X

Hawke, P. J. (2004). The geophysical signatures and exploration potential of Australia's meteorite impact structures (p. 314). Thesis: University of Western Australia.Unpublished

Henkel, H. (1992). Geophysical aspects of meteorite impact craters in eroded shield environment, with special emphasis on electric resistivity. Tectonophysics, 216(1–2), 63–89. https://doi.org/10.1016/0040-1951(92)90156-Z

Henkel, H., Ekneligoda, T. C., & Aaro, S. (2010). The extent of impact induced fracturing from gravity modeling of the Granby and Tvären simple craters. Tectonophysics, 485(1–4), 290–305. https://doi.org/10.1016/j.tecto.2010.01.008

Henkel, H., Reimold, W. U., & Koeberl, C. (2002). Magnetic and gravity model of the Morokweng impact structure. Journal of Applied Geophysics, 49(3), 129–147. https://doi.org/10.1016/S0926-9851(01)00104-5

Ibraheem, I. M., & El-Qady, G. (2017). Hydrogeophysical Investigations at El-Nubariya-Wadi El-Natrun Area, West Nile Delta, Egypt. In A. M. Negm (Ed.), Groundwater in the Nile Delta (73) (235–271). https://doi.org/10.1007/698_2017_154

Ibraheem, I. M., Elawadi, E. A., & El-Qady, G. M. (2018). Structural interpretation of aeromagnetic data for the Wadi El Natrun area, northwestern desert, Egypt. Journal of African Earth Sciences, 139, 14–25. https://doi.org/10.1016/j.jafrearsci.2017.11.036

Ibraheem, I. M., Haggag, M., & Tezkan, B. (2019). Edge Detectors as Structural Imaging Tools Using Aeromagnetic Data: A Case Study of Sohag Area, Egypt. Geosciences, 9(5), 211. https://doi.org/10.3390/geosciences9050211

Ilugbo, S.O., Edunjobi, H., Adewoye, O., Alabi, T., Aladeboyeje, A.I., Olutomilola, O.O., & Owolabi, D.T. (2020). Structural Analysis Using Integrated Aeromagnetic Data and Landsat Imagery in a Basement Complex Terrain, Southwestern Nigeria. Asian Journal of Geological Research, 3(2), 17-33.

Indragiri, N. M. (2019, August). Inversion Modelling 3D Gravity for Hydrocarbon Identification at Sanggau, West Borneo. In IOP Conference Series: Earth and Environmental Science (318) (1) (012025). IOP Publishing. https://doi.org/10.1088/1755-1315/318/1/012025

Jeng, Y., Lee, Y.-L., Chen, C.-Y., & Lin, M.-J. (2003). Integrated signal enhancements in magnetic investigation in archaeology. Journal of Applied Geophysics, 53(1), 31–48. https://doi.org/10.1016/S0926-9851(03)00015-6

Karriqi, A., & Alikaj, P. (2011). Combination of Resistivity “Real Section” with quantitative interpretation of Vertical Electrical Soundings. GeoAlb 2011 “Mineral Resources and their perspective, 466-469.

Kearey, P., Brooks, M., & Hill, I. (2002). An introduction to geophysical exploration (Vol. 4). John Wiley & Sons.

Key, R. M., & Ayres, N. (2000). The 1998 edition of the National Geological Map of Botswana. Journal of African Earth Sciences, 30(3), 427–451. https://doi.org/10.1016/S0899-5362(00)00030-0

Khalil, M. H. (2012). Magnetic, geo-electric, and groundwater and soil quality analysis over a landfill from a lead smelter, Cairo, Egypt. Journal of Applied Geophysics, 86, 146–159. https://doi.org/10.1016/j.jappgeo.2012.08.004

LaFehr, T. R. (1991). Standardization in gravity reduction. GEOPHYSICS, 56(8), 1170–1178. https://doi.org/10.1190/1.1443137

Li, Y., & Oldenburg, D. W. (1998). Separation of regional and residual magnetic field data. SEG Technical Program Expanded Abstracts 1995, 791–794. https://doi.org/10.1190/1.1887567

Li, Y., & Yang, Y. (2011). Gravity data inversion for the lithospheric density structure beneath North China Craton from EGM 2008 model. Physics of the Earth and Planetary Interiors, 189(1–2), 9–26. https://doi.org/10.1016/j.pepi.2011.09.004

Loke, M. H. (2004). Tutorial: 2-D and 3-D electrical imaging surveys. Birmingham, UK. Unpublished

Loke, M. H. (2013). Tutorial: 2-D and 3-D electrical imaging surveys. Geotomo Software Malaysia. Unpublished.

Iugbo, S. O., Edunjobi, H. O., Adewoye, O. E., Alabi, T. O., Aladeboyeje, A. I., Olutomilola, O. O., & Owolabi, D. T. (2020). Structural Analysis Using Integrated Aeromagnetic Data and Landsat Imagery in a Basement Complex Terrain, Southwestern Nigeria. Asian Journal of Geological Research, 3(2), 17-33. https://journalajoger.com/index.php/AJOGER/article/view/30104

Mallick, K., Vasanthi, A., & Sharma, K. K. (2012). Bouguer gravity regional and residual separation: Application to geology and environment. Springer Science & Business Media.

Mankhemthong, N., Morley, C. K., & Srichan, W. (2020). Structure of the Mae On Depression, Chiang Mai province, based on gravity modelling and geological field observation: Implications for tectonic evolution of the Chiang Mai – Chiang Rai Suture Zone, Northern Thailand. Journal of Asian Earth Sciences, 190, 104186. https://doi.org/10.1016/j.jseaes.2019.104186

McCourt, S., Kampunzu, A. B., Bagai, Z., & Armstrong, R. A. (2004). The crustal architecture of Archaean terranes in Northeastern Botswana. South African Journal of Geology, 107(1-2), 147-158. https://doi.org/10.2113/107.1-2.147

McCourt, S., & van Reenen, D. (1992). Structural geology and tectonic setting of the Sutherland Greenstone Belt, Kaapvaal Craton, South Africa. Precambrian Research, 55(1–4), 93–110. https://doi.org/10.1016/0301-9268(92)90017-I

McCourt, S., & Vearncombe, J. R. (1992). Shear zones of the Limpopo Belt and adjacent granitoid-greenstone terranes: Implications for late Archaean collision tectonics in southern Africa. Precambrian Research, 55(1–4), 553–570. https://doi.org/10.1016/0301-9268(92)90045-P

McDonald, A. J. W., Fletchert, C. J. N., Carruthers, R. M., Wilson, D., & Evans, R. B. (1992). Interpretation of the regional gravity and magnetic surveys of Wales, using shaded relief and Euler deconvolution techniques. Geological Magazine, 129(5), 523–531. https://doi.org/10.1017/S0016756800021683

Melosh, H. J. (2011). Planetary Surface Processes. Cambridge University Press. https://doi.org/10.1017/CBO9780511977848

Miller, H. G., & Singh, V. (1994). Potential field tilt—a new concept for location of potential field sources. Journal of Applied Geophysics, 32(2-3), 213-217. https://doi.org/10.1016/0926-9851(94)90022-1

Muchingami, I., Hlatywayo, D. J., Nel, J. M., & Chuma, C. (2012). Electrical resistivity survey for groundwater investigations and shallow subsurface evaluation of the basaltic-greenstone formation of the urban Bulawayo aquifer. Physics and Chemistry of the Earth, Parts A/B/C, 50–52, 44–51. https://doi.org/10.1016/j.pce.2012.08.014

Ndlovu, T., Mashingaitze, R. T., & Mpofu, P. (2015). Analytic Signal and Euler depth interpretation of magnetic anomalies: Applicability to the Beatrice Greenstone Belt. Journal of Geography and Geology, 7(4), 108-112. https://doi.org/10.5539/jgg.v7n4p108

O'Neill, C., & Heine, C. (2005). Reconstructing the Wolfe Creek meteorite impact: Deep structure of the crater and effects on target rock. Australian Journal of Earth Sciences, 52(4–5), 699–709. https://doi.org/10.1080/08120090500170450

Osinowo, O. O., & Taiwo, T. O. (2020). Analysis of high-resolution aeromagnetic (HRAM) data of Lower Benue Trough, Southeastern Nigeria, for hydrocarbon potential evaluation. NRIAG Journal of Astronomy and Geophysics, 9(1), 350–361. https://doi.org/10.1080/20909977.2020.1746890

Osinski, G. R. (2006, May). The geological record of meteorite impacts. In Proc 1st Int Conf Impact Cratering in the Solar System (pp. 8-12).

Osinski, G. R., Grieve, R. A. F., & Tornabene, L. L. (2012). Excavation and Impact Ejecta Emplacement. In G. R. Osinski & E. Pierazzo (Eds.), Impact Cratering (pp. 43–59). John Wiley & Sons, Ltd. https://doi.org/10.1002/9781118447307.ch4

Pati, J. K., & Reimold, W. U. (2007). Impact cratering—Fundamental process in geoscience and planetary science. Journal of Earth System Science, 116(2), 81–98. https://doi.org/10.1007/s12040-007-0009-3

Paya, K., Holmes, H., Brandt, D., Koeberl, C., Dladla, C., & Hancox, P. J. (1999). kgagodi basin, Botswana: origin by meteorite impact confirmed! w. u. reimold1, b. 1.

Pilkington, M., & Grieve, R. A. F. (1992). The geophysical signature of terrestrial impact craters. Reviews of Geophysics, 30(2), 161. https://doi.org/10.1029/92RG00192

Pilkington, M., & Hildebrand, A. R. (2003). Transient and disruption cavity dimensions of complex terrestrial impact structures derived from magnetic data. Geophysical Research Letters, 30(21), 2087. https://doi.org/10.1029/2003GL018294

Pirttijarvi, M. (2008). Gravity interpretation and modeling software based on 3-D block models. User's guide to version, 1.

Pumphrey, H. C. (2014). Gravity surveying: A brief introduction. Edinburgh. Unpublished

Raiskila, S. (2013). Integrated geophysical study of the Keurusselkä impact structure, Central Finland.

Raiskila, S., Plado, J., Ruotsalainen, H., & Pesonen, L. J. (2013). Geophysical Signatures of the Keurusselkä Meteorite Impact Structure-Implications for Crater Dimensions. Geophysical Society of Finland, 49.

Ramotoroko, C., Shemang, E., Lushetile, B., & Sitali, M. (2021). Curie point depth analysis of aeromagnetic data of Kasane region in northwest Botswana and surrounding regions for geothermal investigation of Kasane Hot Spring. Journal of African Earth Sciences, 180, 104214. https://doi.org/10.1016/j.jafrearsci.2021.104214

Ranganai, R. T., Whaler, K. A., & Ebinger, C. J. (2008). Gravity anomaly patterns in the south-central Zimbabwe Archaean craton and their geological interpretation. Journal of African Earth Sciences, 51(5), 257–276. https://doi.org/10.1016/j.jafrearsci.2008.01.011

Rebolledo-Vieyra, M., Urrutia-Fucugauchi, J., & López-Loera, H. (2010). Aeromagnetic anomalies and structural model of the Chicxulub multiring impact crater, Yucatan, Mexico. Revista mexicana de ciencias geológicas, 27(1), 185-195.

Reeves, C. (2005). Aeromagnetic surveys. Principles, Practice and Interpretation. GEOSOFT (Http://Www. Geosoft. Com/Knowledge).

Reid, A. B. (2003). Euler magnetic structural index of a thin-bed fault. GEOPHYSICS, 68(4), 1255–1256. https://doi.org/10.1190/1.1598117

Reid, A. B., Allsop, J. M., Granser, H., Millett, A. J., & Somerton, I. W. (1990). Magnetic interpretation in three dimensions using Euler deconvolution. GEOPHYSICS, 55(1), 80–91. https://doi.org/10.1190/1.1442774

Reimold, W. U., & Koeberl, C. (2014). Impact structures in Africa: A review. Journal of African Earth Sciences, 93, 57–175. https://doi.org/10.1016/j.jafrearsci.2014.01.008

Reimold, W. U., Paya, B. K., Holmes, H., Brandt, D., Koeberl, C., Dladla, C., & Hancox, P. J. (2000). Kgagodi Basin, Botswana: Origin by meteorite impact confirmed! Meteoritics and Planetary Science Supplement, 35, A135.

Reynolds, J. M. (2011). An introduction to applied and environmental geophysics. John Wiley & Sons.

Robbins, S. J., Hynek, B. M., Lillis, R. J., & Bottke, W. F. (2013). Large impact crater histories of Mars: The effect of different model crater age techniques. Icarus, 225(1), 173-184. https://doi.org/10.1016/j.icarus.2013.03.019

Sajeena, S., Kurien, E. K., & Brijesh, V. K. (2015). identification of groundwater potential zones using geophysical technique in Kadalundi river basin, Malappuram, Kerala.

Salem, A., Williams, S., Fairhead, D., Smith, R., & Ravat, D. (2008). Interpretation of magnetic data using tilt-angle derivatives. GEOPHYSICS, 73(1), L1–L10. https://doi.org/10.1190/1.2799992

Selvakumar, T., Mathiazhagan, M., & Madhavi, G. (2015). Geo electrical resistivity survey of the Chennai Sewage Treatment Plants for identifying reclaimed water recharge. Journal of Coastal Sciences, 2(1), 19-23.

Senft, L. E., & Stewart, S. T. (2007). Modeling impact cratering in layered surfaces. Journal of Geophysical Research, 112(E11), E11002. https://doi.org/10.1029/2007JE002894

Stöffler, D., & Grieve, R. (2007). Impactites, Chapter 2.11 in Fettes, D. and Desmons, J. (eds.) Metamorphic Rocks: A Classification and Glossary of Terms, Recommendations of the International Union of Geological Sciences, Cambridge University Press, Cambridge, UK, 82-92, 111-125, and 126-242.

Suleiman, T., Okeke, F. N., & Obiora, N. D. (2020). Interpretation of aeromagnetic data over some parts of Sokoto Basin, Nigeria, using source parameter imaging and 3-D Euler deconvolution methods. International Journal of Physical Sciences, 15(2), 90–98. https://doi.org/10.5897/IJPS2020.4864

Talwani, P., Wildermuth, E., & Parkinson, C. D. (2003). An impact crater in northeast South Carolina inferred from potential field data: impact crater in northeast South Carolina. Geophysical Research Letters, 30(7). https://doi.org/10.1029/2003GL017051

Tarlowski, C., Gunn, P. J., & Mackey, T. (1997). Enhancements of the magnetic map of Australia. AGSO Journal of Australian Geology and Geophysics, 17, 77–82.

Tatchum, C. N., Tabod, T. C., Koumetio, F., & Manguelle-Dicoum, E. (2011). A Gravity Model Study for Differentiating Vertical and Dipping Geological Contacts with Application to a Bouguer Gravity Anomali Over the Foumban Shear Zone, Cameroon. Geophysical, 47(1-2), 43-55.

Tawey, M. D., Alhassan, D. U., Adetona, A. A., Salako, K. A., Rafiu, A. A., & Udensi, E. E. (2020). Application of Aeromagnetic Data to Assess the Structures and Solid Mineral Potentials in Part of North Central Nigeria. 19.

Therriault, A. M., Grieve, R. A. F. and Pilkington, M. (2002): The Recognition of Terrestrial Impact Structures, Bulletin of the Czech Geological Survey, vol. 77, no 4, 253- 263

Titi, Y. L. A., & Minarto, E. (2017, January). The subsurface three-dimensional modeling of volcano arc of Flores island based on gravity data analysis. In AIP Conference Proceedings (Vol. 1788, No. 1, p. 030106). AIP Publishing LLC. https://doi.org/10.1063/1.4968359

Tong, C. H., Lana, C., Marangoni, Y. R., & Elis, V. R. (2010). Geoelectric evidence for centripetal resurge of impact melt and breccias over central uplift of Araguainha impact structure. Geology, 38(1), 91–94. https://doi.org/10.1130/G30459.1

Tsivouraki-Papafotiou, B., Tsokas, G. N., Tsourlos, P. I., & Panas, S. (2003). Regional-residual magnetic field data separation in wavelet domain. Journal of the Balkan Geophysical Society, 6, 209-220.

Vasconcelos, M. A. R., Wünnemann, K., Crósta, A. P., Molina, E. C., Reimold, W. U., & Yokoyama, E. (2012). Insights into the morphology of the Serra da Cangalha impact structure from geophysical modeling. Meteoritics & Planetary Science, 47(10), 1659-1670.https://doi.org/10.1111/maps.12001

Verduzco, B., Fairhead, J. D., Green, C. M., & MacKenzie, C. (2004). New insights into magnetic derivatives for structural mapping. The Leading Edge, 23(2), 116–119. https://doi.org/10.1190/1.1651454

Yeomans, C. M., Head, M., & Lindsay, J. J. (2021). Application of the tilt derivative transform to bathymetric data for structural lineament mapping. Journal of Structural Geology, 146, 104301. https://doi.org/10.1016/j.jsg.2021.104301

Yusoh, R., Saad, R., Saidin, M., Muhammad, S. B., & Anda, S. T. (2018). Integration of Electrical Resistivity and Seismic Refraction using Combine Inversion for Detecting Material Deposits of Impact Crater at Bukit Bunuh, Lenggong, Perak. Journal of Physics: Conference Series, 995, 012099. https://doi.org/10.1088/1742-6596/995/1/012099

Zahra, H. S., & Oweis, H. T. (2016). Application of high-pass filtering techniques on gravity and magnetic data of the eastern Qattara Depression area, Western Desert, Egypt. NRIAG Journal of Astronomy and Geophysics, 5(1), 106–123. https://doi.org/10.1016/j.nrjag.2016.01.005

Zakariah, M. N. A., Roslan, N., Sulaiman, N., Lee, S. C. H., Hamzah, U., Noh, K. A. M., & Lestari, W. (2021). Gravity Analysis for Subsurface Characterization and Depth Estimation of Muda River Basin, Kedah, Peninsular Malaysia. Applied Sciences, 11(14), 6363. https://doi.org/10.3390/app11146363

Zeh, A., Gerdes, A., Klemd, R., & Barton, J. M. (2007). Archaean to Proterozoic Crustal Evolution in the Central Zone of the Limpopo Belt (South Africa-Botswana): Constraints from Combined U-Pb and Lu-Hf Isotope Analyses of Zircon. Journal of Petrology, 48(8), 1605–1639. https://doi.org/10.1093/petrology/egm032

Zhou, T., & Tao, D. (2011, October). Godec: Randomized low-rank & sparse matrix decomposition in noisy case. In Proceedings of the 28th International Conference on Machine Learning, ICML 2011.

Zylberman, William, "Geophysical Study of Complex Meteorite Impact Structures" (2017). Electronic Thesis and Dissertation Repository 5165. https://ir.lib.uwo.ca/etd/5165